MODELING AND CONTROL OF A SYNCHRONOUS GENERATOR WITH ELECTRONIC LOAD

Ivan Jadric

Thesis submitted to the Faculty of

Virginia Polytechnic Institute and State University

in partial fulfillment of the requirements for the degree of

Master of Science

in

Electrical Engineering

Dr. Dušan Borojevic, Chair

Dr. Fred C. Lee

Dr. Douglas K. Lindner

January 5, 1998

Blacksburg, Virginia

Keywords: synchronous generators, diode rectifiers, modeling, stability, control

MODELING AND CONTROL OF A SYNCHRONOUS GENERATOR WITH ELECTRONIC LOAD

Ivan Jadric

(ABSTRACT)

Design and analysis of a system consisting of a variable-speed synchronous generator that supplies an active dc load (inverter) through a three-phase diode rectifier requires adequate modeling in both time and frequency domain. In particular, the system's control-loops, responsible for stability and proper impedance matching between generator and load, are difficult to design without an accurate small-signal model. A particularity of the described system is strong non-ideal operation of the diode rectifier, a consequence of the large value of generator's synchronous impedance. This non-ideal behavior influences both steady state and transient performance. This thesis presents a new, average model of the system. The average model accounts, in a detailed manner, for dynamics of generator and load, and for effects of the non-ideal operation of diode rectifier. The model is non-linear, but time continuous, and can be used for large- and small-signal analysis.

The developed model was verified on a 150 kW generator set with inverter output, whose dc-link voltage control-loop design was successfully carried out based on the average model.

Acknowledgements

This thesis is a result of my two-and-a-half year stay at Virginia Power Electronics Center (VPEC) at Virginia Tech. During that period, many people have contributed to my learning and, at the same time, to having a good time.

Dr. Dusan Borojevic has been as much a friend as an academic advisor. Memories of good company, conversation and food at his home will probably last longer than those of synchronous generator control design.

Classes I took with Dr. Fred C. Lee and Dr. Douglas K. Lindner were sources of valuable knowledge, without which this thesis could not have been completed. I also wish to thank them for their helpful and stimulating comments and suggestions in the final stage of writing of the text.

Luca Amoroso, Paolo Nora, Richard Zhang, V. Himamshu Prasad, Xiukuan Jing, Ivana Milosavljevic, Zhihong Sam Ye, Ray Lee Lin and Nikola Celanovic are only some of my fellow graduate students with whom I despaired over overdue homework and projects, senseless simulation results and non-working hardware. I wish them all plenty of success in the future.

All VPEC faculty and staff members were extremely helpful whenever they were needed. My special thanks go to Teresa Shaw, Linda Fitzgerald, Jeffrey Batson and Jiyuan Lunan.

I gratefully acknowledge the Kohler Company for providing support for the project that this work was part of. A summer internship at this company was a learning opportunity for me and useful out-of-academia experience.

Jeni, of course, is a very special person who has made my life happier for almost a year now by successfully distracting me from work. I hope she continues doing that in the years to come.

Finally, I cannot omit from these acknowledgements an ancient Roman emperor who decided to retire in a very special corner of the world, and thus founded a place to live for people who contributed greatly to what I am today.

Table of Contents

CHAPTER 1. INTRODUCTION **1**

1.1. Motivation for this work and state of the art 1

1.2. Thesis outline 8

CHAPTER 2. SYNCHRONOUS GENERATOR DYNAMIC MODELING **10**

2.1. Synchronous generator model in rotor reference frame 10

2.1.1. Assumptions for model development 11

2.1.2. Development of the model's equations and equivalent circuit 12

2.1.3. Sinusoidal steady state operation 18

2.1.4. Model implementation in a simulation software 21

2.2. Parameter identification 23

2.2.1. Main generator 26

2.2.2. Exciter 26

CHAPTER 3. SWITCHING MODEL **34**

3.1. Introduction 34

3.2. Simulation and experimental results 35

3.3. Analysis of switching model results 40

CHAPTER 4. AVERAGE MODEL **48**

4.1. Concept of the average model 48

4.2. Formulation of average model equations 51

4.2.1. System space-vector diagram 51

4.2.2. Average model equations 52

4.3. Verification of the average model 55

4.4. Validity of the average model 65

4.4.1. Discussion of first harmonic assumption 65

4.4.2. Average model and diode rectifier losses 65

4.4.3. Use of the average model with different loads and sources 69

4.5. Linearized average model 70

4.5.1. Linearization of model equations 70

4.5.2. Linearized state-space representation 73

4.5.2.1. Exciter's equations 74

4.5.2.2. Main generator's equations 78

4.5.2.3. State-space representation of the system 80

4.5.3. Transfer functions 83

CHAPTER 5. DC-LINK CONTROL-LOOP DESIGN **91**

5.1. Introduction 91

5.2. PI compensator 93

5.2.1. Design 93

5.2.2. Operation with resistive dc load 95

5.2.3. Operation with inverter load and instability problem 98

5.3. Multiple-pole, multiple-zero compensators 100

5.3.1. Design 100

5.3.2. Operation with resistive dc load 106

5.3.3. Operation with inverter load 111

CHAPTER 6. CONCLUSIONS 113

List of Figures

Fig. 1.1. Block diagram of the studied system. 1

Fig. 1.2. Ideal three-phase voltage source feeding a dc current source load through a diode rectifier. 3

Fig. 1.3. Ac waveforms of the system shown in Fig. 1.2. 3

Fig. 1.4. Non-ideal voltage source feeding a current source dc load through a diode rectifier. 4

Fig. 1.5. Main generator's line-to-line voltage and phase current with a 100 kW resistive load connected to the dc-link (time scale: 2 ms/div). 5

Fig. 1.6. Block diagram of the studied system in closed loop. 6

Fig. 2.1. Synchronous generator's equivalent circuit in rotor reference frame. 17

Fig. 2.2. Generator's space vector diagram for sinusoidal steady state operation. 20

Fig. 2.3. Implementation of generator's three-phase output. 21

Fig. 2.4. Implementation of generator's field voltage. 23

Fig. 2.5. Circuit for measurement of L_d and L_d'. 27

Fig. 2.6. Circuit for measurement of T_{do}' and T_d'. 29

Fig. 2.7. Circuit for measurement of q axis parameters. 31

Fig. 3.1. Generator/rectifier switching model. 35

Fig. 3.2. Block diagram of the simulated system. 35

Fig. 3.3. Switching model simulation: the main generator's line voltage and phase current (n=2280 rpm, R_l=19 Ω, v_{fd}=16 V). 36

Fig. 3.4. Switching model simulation: the main generator's line voltage and phase current (n=3340 rpm, R_l=6.4 Ω, v_{fd}=33 V). 36

Fig. 3.5. Measurement: the main generator's line voltage and phase current (n=2280 rpm, R_l=19 Ω, v_{fd}=15.2 V). 37

Fig. 3.6. Measurement: the main generator's line voltage and phase current (n=3340 rpm, R_l=6.4 Ω, v_{fd}=31 V). 37

Fig. 3.7. Switching model simulation: the exciter's line-to-line voltage and phase current (n=3340 rpm, R_l=6.4 Ω, v_{fd}=33 V). 38

Fig. 3.8. Switching model simulation: the main generator's field voltage at exciter's field voltage step from 0 V to 47.5 V (n=4000 rpm, R_l=4.27 Ω). 39

Fig. 3.9. Switching model simulation: the main generator's phase voltage and phase current (n=2280 rpm, R_l=19 Ω, v_{fd}=16 V). 41

Fig. 3.10. Switching model simulation: the main generator's phase voltage and phase current (n=3340 rpm, R_l=6.4 Ω, v_{fd}=33 V). 41

Fig. 3.11. Switching model simulation: the exciter's phase voltage and phase current (n=3340 rpm, R_l=6.4 Ω, v_{fd}=33 V). 42

Fig. 3.12. Switching model simulation: the main generator's steady state armature d-axis voltage and current. 43

Fig. 3.13. Generator's space vector diagram for non-sinusoidal steady state. 44

Fig. 3.14. Engine speed as function of the main generator's load, defining operating points (100%=150 kW). 44

Fig. 3.15. Variation of ϕ with the operating point. 45

Fig. 3.16. Variation of k_v with the operating point. 47

Fig. 3.17. Variation of k_i with the operating point. 47

Fig. 4.1. Generator/rectifier space vector diagram. 51

Fig. 4.2. Block diagram of the average model. 53

Fig. 4.3. Switching model simulation: the main generator's field voltage at the exciter's field voltage step from 0 V to 47.5 V (n=4000 rpm, R_l=4.27 Ω). 57

Fig. 4.4. Average model simulation: the main generator's field voltage at the exciter's field voltage step from 0 V to 47.5 V (n=4000 rpm, R_l=4.27 Ω). 57

Fig. 4.5. Measurement: dc-link voltage and the exciter's field current at the exciter's field voltage step from 0 V to 8.5 V (n=3050 rpm, R_l=18.75 Ω). 58

Fig. 4.6. Switching model simulation: dc-link voltage and the exciter's field current at the exciter's field voltage step from 0 V to 7 V (n=3050 rpm, R_l=18.75 Ω). 59

Fig. 4.7. Average model simulation: dc-link voltage and the exciter's field current at the exciter's field voltage step from 0 V to 7 V (n=3050 rpm, R_l=18.75 Ω). 59

Fig. 4.8. Measurement: dc-link voltage and the exciter's field current at the exciter's field current step from 0.34 A to 0 A (n=3050 rpm, R_l=18.75 Ω.). 60

Fig. 4.9. Switching model simulation: dc-link voltage and the exciter's field current at the exciter's field current step from 0.38 A to 0 A (n=3050 rpm, R_l=18.75 Ω). 60

Fig. 4.10. Average model simulation: dc-link voltage and the exciter's field current at the exciter's field current step from 0.38 A to 0 A (n=3050 rpm, R_l=18.75 Ω). 61

Fig. 4.11. Measurement: dc-link voltage and the exciter's field current at resistive load step from 12.5 Ω to 6.25 Ω (n=3100 rpm, v_{fd}=11.6 V). 62

Fig. 4.12. Switching model simulation: dc-link voltage and the exciter's field current at resistive load step from 12.5 Ω to 6.25 Ω (n=3100 rpm, v_{fd}=11.6 V). 62

Fig. 4.13. Average model simulation: dc-link voltage and the exciter's field current at resistive load step from 12.5 Ω to 6.25 Ω (n=3100 rpm, v_{fd}=11.6 V). 63

Fig. 4.14. (a) measurement, (b) average model simulation: dc-link voltage in transient following disconnection of 19 Ω resistive dc load (n=2000 rpm, v_{fd}=3.4 V in (a), v_{fd}=1.85 V in (b)). 63

Fig. 4.15. (a) measurement, (b) average model simulation: dc-link voltage in transient following disconnection of 19 Ω resistive dc load (n=3700 rpm, v_{fd}=2.8 V in (a), v_{fd}=2.03 V in (b)). 64

Fig. 4.16. Diode rectifier's efficiency variation with load. 67

Fig. 4.17. Magnitude of the exciter's field voltage-to-dc-link voltage transfer function with current source load, at two different operating points. 84

Fig. 4.18. Phase of the exciter's field voltage-to-dc-link voltage transfer function with current source load, at two different operating points. 85

Fig. 4.19. Magnitude of the exciter's field voltage-to-dc-link voltage transfer function at 3340 rpm, 105 kW, with different kinds of load. 88

Fig. 4.20. Phase of the exciter's field voltage-to-dc-link voltage transfer function at 3340 rpm, 105 kW, with different kinds of load. 88

Fig. 4.21. The exciter's field voltage-to-exciter's field current transfer function at 3340 rpm, 105 kW current source load. 90

Fig. 4.22. The exciter's field voltage-to-main generator's field current transfer function at 3340 rpm, 105 kW current source load. 90

Fig. 5.1. The exciter's field voltage-to-dc-link voltage transfer function at 3340 rpm and 105 kW current source load. 92

Fig. 5.2. Small-signal block diagram of the closed-loop system. 92

Fig. 5.3. Analog realization of a PI compensator. 94

Fig. 5.4. Loop gain with PI compensator (3340 rpm, 105 kW current source load). 95

Fig. 5.5. Average model simulation: dc-link voltage and the exciter's field current at resistive load step from 8.3 Ω to 12.5 Ω (n=2000 rpm, V_g=25 V). 96

Fig. 5.6. Measurement: dc-link voltage and the exciter's field current at resistive load step from 8.3 Ω to 12.5 Ω (n=2000 rpm, V_g=25 V). 96

Fig. 5.7. Average model simulation: dc-link voltage and the exciter's field current at resistive load step from 8.3 Ω to 12.5 Ω (n=3800 rpm, V_g=15 V). 97

Fig. 5.8. Measurement: dc-link voltage and the exciter's field current at resistive load step from 8.3 Ω to 12.5 Ω (n=3800 rpm, V_g=15 V). 97

Fig. 5.9. Illustration for instability problem. 98

Fig. 5.10. Magnitude of the generator's output impedance (in open and closed loop) and the inverter's input impedance (3340 rpm, 105 kW current source load). 99

Fig. 5.11. Loop gain with four-pole, three-zero compensator (3340 rpm, 105 kW current source load). 101

Fig. 5.12. Generator's closed loop output impedance with four-pole, three zero compensator (3340 rpm, 105 kW current source load). 102

Fig. 5.13. Multiple-pole, multiple-zero compensators' transfer function's magnitudes. 103

Fig. 5.14. Loop gain with five-pole, three-zero compensator (3340 rpm, 105 kW current source load). 104

Fig. 5.15. Generator's closed loop output impedance with five-pole, three zero compensator (3340 rpm, 105 kW current source load). 104

Fig. 5.16. Analog realization of a five-pole, three-zero compensator. 105

Fig. 5.17. Average model simulation: the dc-link voltage and exciter's field current for a resistive load step from 8.3 Ω to 12.5 Ω (n=2000 rpm, V_g=25 V). 107

Fig. 5.18. Measurement: the dc-link voltage and exciter's field current for a resistive load step from 8.3 Ω to 12.5 Ω (n=2000 rpm, V_g=25 V). 107

Fig. 5.19. Average model simulation: the dc-link voltage and exciter's field current for a resistive load step from 8.3 Ω to 12.5 Ω (n=3800 rpm, V_g=15 V). 108

Fig. 5.20. Measurement: the dc-link voltage and exciter's field current for a resistive load step from 8.3 Ω to 12.5 Ω (n=3800 rpm, V_g=15 V). 108

Fig. 5.21. Average model simulation: the dc-link voltage and exciter's field current for a resistive load step from 12.5 Ω to 8.3 Ω (n=2000 rpm, V_g=25 V). 109

Fig. 5.22. Measurement: the dc-link voltage and exciter's field current for a resistive load step from 12.5 Ω to 8.3 Ω (n=2000 rpm, V_g=25 V). 109

Fig. 5.23. Average model simulation: the dc-link voltage and exciter's field current for a resistive load step from 12.5 Ω to 8.3 Ω (n=3800 rpm, V_g=15 V). 110

Fig. 5.24. Measurement: the dc-link voltage and exciter's field current for a resistive load step from 12.5 Ω to 8.3 Ω (n=3800 rpm, V_g=15 V). 110

Fig. 5.25. Measurement: the dc-link voltage and exciter's field current at step in the inverter's resistive three-phase load from 18.8 kW to 12.8 kW (n=3000 rpm, V_g=35 V). 111

Fig. 5.26. Measurement: the dc-link voltage and exciter's field current at step in the inverter's resistive three-phase load from 12.8 kW to 18.8 kW (n=3800 rpm, V_g=35 V). 112

List of Tables

Table 2.1. Measured exciter's parameters. 32

Table 4.1. Values of k_v, k_i and ϕ used for verification of the average model. 56

Table 4.2. Poles and zeros of $\tilde{v}_{adc} / \tilde{v}_{efd}$ transfer function at 3340 rpm, 105 kW current source load. 86

Table 4.3. Poles and zeros of $\tilde{v}_{adc} / \tilde{v}_{efd}$ transfer function at 3340 rpm, 105 kW resistive load. 89

Chapter 1. Introduction

1.1. Motivation for this work and state of the art

This work was motivated by the need to study dynamics and control design of the system whose block diagram is shown in Fig. 1.1. It is a 150 kW generator set with inverter output, in which a natural gas engine drives a synchronous generator (which, throughout this text, will also be referred to as main generator). Field voltage is provided to the main generator by means of a separate, smaller synchronous machine, an exciter. The exciter is constructed with field winding on the stator and armature winding on the rotor; that makes it possible to rectify the exciter's armature ac voltages by a rotating diode bridge, and connect the rectifier's output directly to the field winding of the main generator.

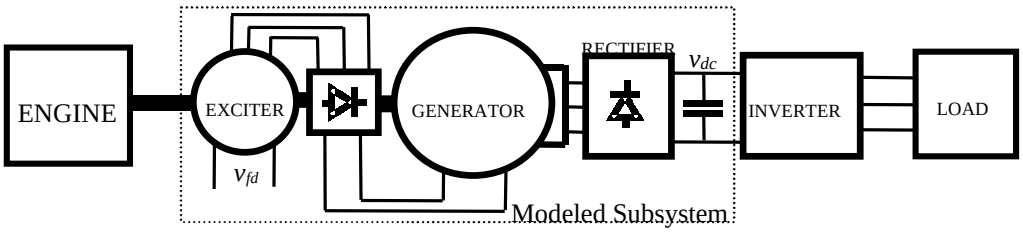

Fig. 1.1. Block diagram of the studied system.

The main generator's output is rectified by another diode bridge, in order to form a dc-link that feeds an inverter. Balanced three-phase voltages are supplied to the load by this inverter. Since the inverter also determines load frequency, it is not necessary to operate the generator at constant speed corresponding to 60 Hz.

In order to make engine operation as efficient as possible, speed is varied from 1800 rpm to 4000 rpm according to a load-versus-speed relationship considered optimal for the engine. Such variable speed operation affects generator design in several ways, of which the most important for our study is the effect it has on the value of main generator's synchronous inductance. With standard generator design, at minimum speed a relatively large main generator's field current would be required in order to achieve the rated generator output voltage. That would result in large exciter's armature currents, and overheating of the exciter. The minimum amount of cooling (due to minimum speed) would make this problem even more serious. In order to avoid this, generator designers increased the number of turns of the main generator's armature windings. That resulted in a smaller field current required to obtain the rated output voltage but, at the same time, it significantly increased main generator's synchronous inductance.

A peculiarity of the system shown in Fig. 1.1 is the fact that both synchronous machines, the exciter and main generator, have electronic load: they feed reactive dc loads through diode rectifiers. If a synchronous machine were an ideal voltage source, Fig. 1.2 would represent its simplified circuit diagram with a diode bridge and a dc current source load. It is a textbook example of how non-linear, switching elements (diodes) cause non-sinusoidal ac waveforms [1]. In Fig. 1.2, v_a, v_b and v_c are sinusoidal voltages with amplitude V_p and a phase shift of 120^o one with respect to another. I_{dc} is a constant dc current representing dc load. Average value of the dc voltage at the rectifier's output can be calculated as

$$\hat{v}_{dc} = \frac{3\sqrt{3}}{\pi} V_p \,. \tag{1.1}$$

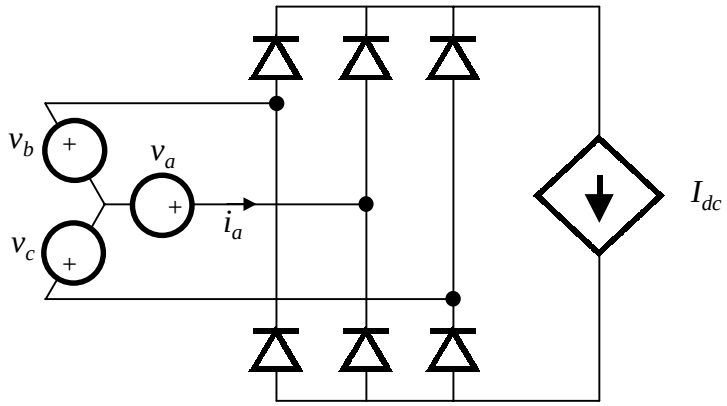

Fig. 1.2. Ideal three-phase voltage source feeding a dc current source load through a diode rectifier.

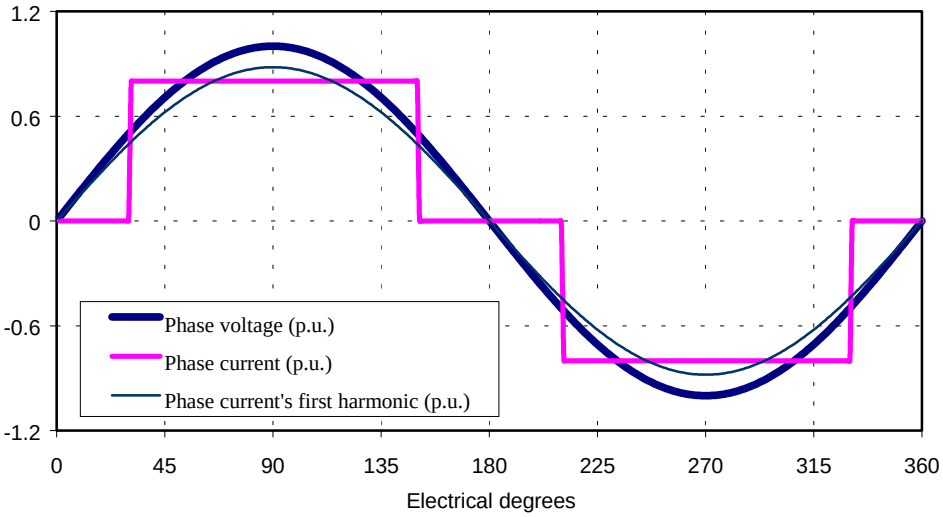

Fig. 1.3. Ac waveforms of the system shown in Fig. 1.2.

Fig. 1.3 shows qualitative waveforms of phase voltage v_a and phase current i_a. It can be seen that, due to diode rectification and current-source dc load, the phase current has a quasi-square waveform. First harmonic of i_a, i_{a1}, is also shown. Its amplitude can be calculated as

$$I_{a1} = \frac{2\sqrt{3}}{\pi} I_{dc} \,. \tag{1.2}$$

It is important to notice in Fig. 1.3 that voltage is in phase with current's first harmonic. Therefore, from the point of view of the ac input's fundamental voltage and

current harmonics, an ideal diode rectifier with a current source dc load behaves like a nonlinear resistor.

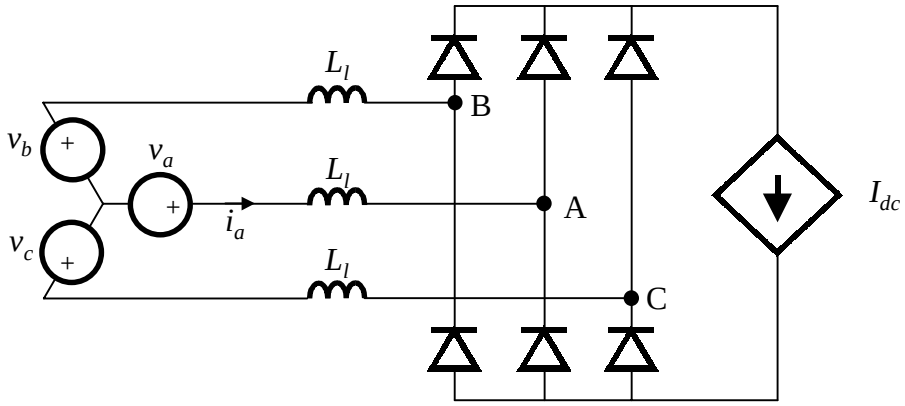

Fig. 1.4. Non-ideal voltage source feeding a current source dc load through a diode rectifier.

The situation is somewhat more complicated if ac side's parasitic inductances L_l are considered [1]. These inductances normally represent transformer or power line leakage inductance, and need to be placed in series with ideal voltage sources v_a, v_b and v_c, as shown in Fig. 1.4. They cause non-ideal operation of the diode bridge, i.e. they cause diode commutations to be non-instantaneous; the time required for commutation is usually expressed in terms of commutation angle u, which is a function of parasitic input inductance L_l, line frequency ω and output current I_{dc} [1]:

$$u = \cos^{-1}\left(1 - \frac{2\omega L_l I_{dc}}{\sqrt{3}V_p}\right). \tag{1.3}$$

Non-instantaneous diode commutations cause distortion in diode bridge input voltage waveforms, v_{AB}, v_{BC} and v_{CA}, while edges of the current waveform have some finite slope. Also, the average value of the output dc voltage is somewhat reduced compared to the ideal case, and it can be expressed as [1]:

$$\widehat{v}_{dc} = \frac{3\sqrt{3}}{\pi}V_p\left(1 - \frac{\omega L_l I_{dc}}{\sqrt{3}V_p}\right). \tag{1.4}$$

Expression (1.4) is valid only if $u < \frac{\pi}{3}$; for cases in which $u \geq \frac{\pi}{3}$, expressions similar to (1.4) can be found [1].

It needs to be understood that (1.1) and (1.2) describe an ideal operation of the diode rectifier in an average sense: they express average dc output voltage by means of input ac peak voltage, and fundamental harmonic of input ac current by means of the output dc current. These expressions do not contain any information about the voltage ripple at the dc side and the current's higher harmonics at the ac side.

A synchronous generator is never an ideal voltage source, and it is even less so if it is characterized by a large value of synchronous inductance. If it is connected to a diode rectifier, inductance L_l from Fig. 1.4 is of the order of magnitude of the generator's synchronous inductance. Therefore, it can be expected that the exciter's and the main generator's ac terminal voltage and current waveforms will be heavily distorted [2]-[7]. Fig. 1.5 shows measured waveforms of the system from Fig. 1.1 and can serve as an example of such distortion. It can be seen that the main generator's line-to-line voltage is a quasi-square wave, and the current is also far from being sinusoidal.

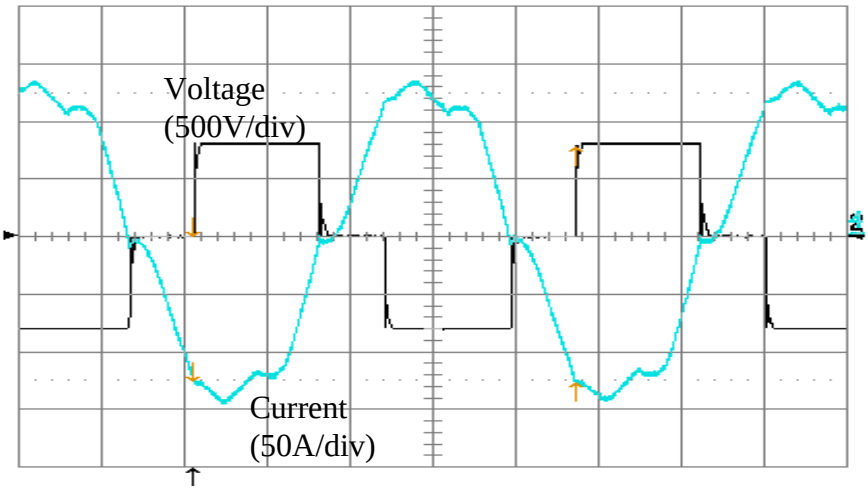

Fig. 1.5. Main generator's line-to-line voltage and phase current with a 100 kW resistive load connected to the dc-link (time scale: 2 ms/div).

Similarly, a dc load is never an ideal dc current source. For a heavily inductive dc load, like the main generator's field winding that loads the exciter in Fig. 1.1, the current

source approximation is very close to the actual situation. For the main generator, which has a large dc-link capacitor and an inverter as a load, that is not the case.

For the above reasons, operation of the system shown in Fig. 1.1 cannot be described with analytical expressions such as (1.1) (or (1.3)) and (1.2). Moreover, even though it is not obvious from Fig. 1.5, there is a phase-shift between the first harmonics of the phase voltage and the phase current. Therefore, as a result of the non-ideal operation of the diode-bridge, the generator will behave as if some reactive load were connected to its terminals.

Some design aspects relative to the system shown in Fig. 1.1 (e.g., design of protection measures at the dc-link) require large-signal, time-domain simulation results. Simulation of the system's switching model can provide these results, but is extremely time- and memory consuming (time-constants of the system are of the order of magnitude of hundreds of milliseconds, and the maximum simulation time-step needs to be kept well below the switching ripple period, i.e. on the order of millisecond). Therefore, from the point of view of large signal analysis, the need for an 'average' model of the system can be anticipated. Such a model would describe dynamic behavior of the system without including any switching elements.

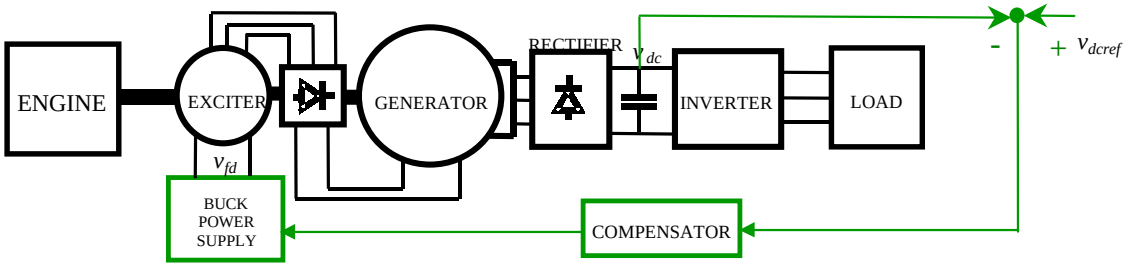

Fig. 1.6. Block diagram of the studied system in closed loop.

The system shown in Fig. 1.1 cannot work in open loop: dc-link voltage, v_{dc}, needs to be regulated at a constant value (800 V) for the inverter to operate properly. Since diode rectification provides no means of regulation, constant dc-link voltage can be achieved only by adjusting the exciter's field voltage v_{fd}. That can be done by closing the dc-link voltage feedback control-loop, as shown in Fig. 1.6. This control-loop provides

regulation of the inverter's input voltage, but also plays an important role in impedance matching between the generator and inverter, thus assuring system stability.

In order to design the compensator in Fig. 1.6, it is necessary to have a good small-signal model representing the system's dynamic behavior. A three-phase, salient pole, wound field synchronous generator is characterized by relatively complex dynamics. In order to describe properly its electrical behavior, it is necessary to deal with at least a third order system, which becomes fifth (or higher) order if there are damper windings present in the machine [8], [9]. These high-order models contain complete information about the generator's dynamics, but are often quite demanding to use, both from parameters identification and computational burden point of view. In particular, for the generator's control-loop design, it is a common practice to model a generator as a first-order system [11], [12]. For that simplification to be legitimate, two assumptions need to be true. First, the generator has to behave as a good voltage source; i.e. its synchronous impedance needs to be small. Second, the generator must operate at constant speed. Both assumptions are normally true for large generators used in power generation plants. However, the system shown in Fig. 1.1 is characterized by variable speed and the large main generator's synchronous impedance. Also, if the exciter's field voltage is considered input, and the dc-link voltage output variable, the overall order of the system is eight. Therefore, it can be suspected that the above-mentioned, single-pole generator model would hardly be appropriate. The presence of diode rectifiers makes modeling of the system even more difficult. The diode's switching behavior causes the system to be time-discontinuous, and therefore impossible to linearize. Moreover, it is not clear how to model the effect of the distorted generator's ac waveforms.

The above–mentioned, design–related requirements for transient and small–signal representation of the system's behavior define the goal of this work. It consists of developing a model of the system with the following properties:

- Accurate dynamic representation of the generator, load and effects of non-ideal operation of diode rectifier;

- Suitability for time domain simulations, with emphasis on efficient use of CPU time and computer memory; and
- Suitability for small-signal analysis and application to control design.

The following section is a short overview of the topics covered in the body of the text.

1.2. Thesis outline

Chapter 2, Synchronous Generator Dynamic Modeling, starts with a summary of synchronous machine's dynamic model development. This model has been known for more than half a century, and that is why its development is not carried out in a detailed manner; only the main assumptions and results are presented. During the work that resulted in this thesis, a considerable amount of time and effort was spent on the parameter identification problem, particularly for the exciter. That is why this chapter also contains a brief description of the parameter identification process. Following that is a section dedicated to the review of the generator's steady state operation, and a short section on how the generator's model can be implemented in a simulation software like PSpice.

In Chapter 3, results obtained by simulating the "modeled subsystem" from Fig. 1.1 are presented and compared to the measurement results. This is referred to as the "switching model" of the system, since it includes switching elements (diodes), and therefore describes the system as it actually operates. Results obtained with the switching model simulations are discussed, and the basis is set for the development of the average model.

Chapter 4, Average Model, is the most innovative part of this work. Based on conclusions regarding the switching model of the system, this chapter shows how a system, consisting of a synchronous generator, a diode bridge rectifier and some reactive

dc load, can be modeled in a simplified way. This is referred to as the “average model” of the system. The average model preserves all of the system’s relevant dynamic information, but it does not include any switching elements. That makes it particularly useful for linearization and control-loop design. Assumptions for the development of the average model are presented, and derivation of the model’s equations is carried out. The average model is then verified through comparison with the switching model and measurement results. Since the average model equations are non-linear, it is shown how they can be linearized and how the corresponding state-space representation of the system can be found. Finally, a discussion on model’s validity is included.

Chapter 5 contains dc-link voltage control-loop design procedure. It is based on the exciter’s field voltage-to-dc-link voltage transfer function obtained with the average model developed in Chapter 4. A design procedure for a PI compensator is given, and transient simulation and measurement results with resistive load at the dc-link are shown. Unstable operation of this compensator with an inverter load due to poor impedance matching between different parts of the system is discussed, and the need for a higher-order dynamic compensator is justified. A five-pole, three-zero compensator is found to be satisfactory, and its design process is carried out. Validity of this compensator is confirmed through simulation and measurement results of transient operation with resistive and inverter load at the dc-link.

Chapter 6 concludes the thesis by summarizing its most important results.

Chapter 2. Synchronous Generator Dynamic Modeling

2.1. Synchronous generator model in rotor reference frame

It was explained in the introductory chapter why a first-order synchronous machine model would not be appropriate for the application that motivated the work presented in this thesis. The purpose of this section is to introduce a detailed synchronous generator model, which takes into account all relevant dynamic phenomena occurring in the machine. Since this model has been widely known since 1930s, only the main assumptions and results will be presented.

2.1.1. Assumptions for model development

A three-phase, wound-field synchronous generator has three identical armature windings symmetrically distributed around the air-gap, and one field winding. One or more damper windings can also be present and, for our convenience in this section, we will assume that one damper winding is present in each machine's axis. Normally, armature windings are placed on the stator, and field and damper windings on the rotor. However, there are cases, such as the exciter in Fig. 1.1, when armature windings are placed on the rotor and field winding on the stator (the exciter has no damper windings). This does not affect the machine modeling approach at all, since only relative motion between the stator and rotor windings is important. Therefore, throughout this text, when we refer to 'rotor windings', we will always imply the field (and damper, if existent) winding placed at the opposite side of the air gap with respect to the three-phase armature windings.

Several assumptions are needed in order to simplify the actual synchronous machine and make the model development less tedious [9]:

1. It is assumed that every winding present in the machine produces a sinusoidal MMF along the air gap, which, for phase *a*, can be expressed as $\theta_a = \Theta_a \sin\left(\frac{P}{2}\gamma_s\right)$, where P represents the machine's number of poles, and γ_s stands for the stator's angular coordinate;
2. Iron permeability in the machine is assumed to be infinite. This is equivalent to neglecting all effects due to magnetic saturation, and flux fringing;
3. Rotor construction is assumed to be the only factor contributing to magnetic asymmetry in the machine. Effects of the stator or rotor slots can be taken into account by Carter's factor. This assumption results in approximating the magnetic conductivity function as $\lambda = \lambda_0 - \lambda_2 \cos(P\gamma_s)$, where λ_0 and λ_2 depend on the geometry of the air gap; and

4. Local value of magnetic flux density B is obtained by multiplying local values of MMF and magnetic conductivity. The third harmonic of the magnetic flux density resulting from this multiplication is neglected, in accordance with assumption 1.

Errors introduced by these assumptions are normally small enough to be negligible, particularly from the point of view of the machine's dynamic performance.

2.1.2. Development of the model's equations and equivalent circuit

A synchronous machine can be described by a system of $n+1$ equations, n of which are electrical and one of which is mechanical. The number n of electrical equations is equal to the number of independent electrical variables necessary to describe the machine. These variables can be either currents or flux linkages. Currents are chosen to be the independent variables in this thesis.

Electrical equations are obtained by writing Kirchoff's voltage law for every winding, i.e. by equating the voltage at the winding's terminal to the sum of resistive and inductive voltage drops across the winding [8], [9]. Note that damper windings, if present, are always short circuited. Therefore, their terminal voltage is equal to zero.

In order to correctly calculate the inductive voltage drop across a winding, total magnetic flux linked with the winding needs to be evaluated. That is achieved by means of an inductance matrix, which relates all windings' flux linkages to all windings' currents. When that is done for a salient-pole synchronous machine, an inductance matrix dependent on the rotor position is obtained. This dependence is due to the magnetic asymmetry of the rotor: because of the way the rotor of a salient pole machine is shaped, there exists a preferable magnetic direction. This direction coincides with the direction of the flux produced by the field winding, and is defined as machine's d axis. The machine's q axis is placed at 90 electrical degrees (in a counterclockwise direction) with respect to

the machine's *d* axis. Then, the rotor position can be expressed by means of an angle, named θ, between the magnetic axis of the armature's phase *a* and the rotor's *q* axis.

Dependence of the inductance matrix on the rotor position represents the main difficulty in modeling the synchronous machine. A solution to this problem is to change the reference system, or frame, in which the machine's electrical and magnetic variables are expressed. So far, the reference frame intuitively used was the so-called stationary, or stator, or *abc* reference frame. In it, variables are expressed as they can actually be measured in the machine, but the machine parameters are time variant (since θ is a function of time). It can be shown that the only reference frame that provides constant machine parameters is the rotor, or *dq*, reference frame. In it, all variables are expressed in a form in which a hypothetical observer placed on the rotor would measure them. Transformation from the *abc* to the *dq* reference frame is given by the following transformation matrix:

$$\mathbf{T} = \sqrt{\frac{2}{3}}\begin{bmatrix} \sin\theta & \sin\left(\theta - \frac{2\pi}{3}\right) & \sin\left(\theta + \frac{2\pi}{3}\right) \\ \cos\theta & \cos\left(\theta - \frac{2\pi}{3}\right) & \cos\left(\theta + \frac{2\pi}{3}\right) \end{bmatrix}. \tag{2.1}$$

Inverse transformation (from the *dq* to the *abc* reference frame) is then given by

$$\mathbf{T}_{inv} = \sqrt{\frac{2}{3}}\begin{bmatrix} \sin\theta & \cos\theta \\ \sin\left(\theta - \frac{2\pi}{3}\right) & \cos\left(\theta - \frac{2\pi}{3}\right) \\ \sin\left(\theta + \frac{2\pi}{3}\right) & \cos\left(\theta + \frac{2\pi}{3}\right) \end{bmatrix}. \tag{2.2}$$

In (2.1) and (2.2), θ is calculated as

$$\theta(t) = \int_0^t \omega(\xi)d\xi + \theta_0\,, \tag{2.3}$$

where ω represents the rotor's (electrical) speed.

Therefore, any set of three-phase variables f_a, f_b and f_c expressed in the *abc* reference frame can be transformed in *dq* reference frame variables f_d and f_q by multiplying them by **T**:

$$\begin{bmatrix} f_d \\ f_q \end{bmatrix} = \mathbf{T} \begin{bmatrix} f_a \\ f_b \\ f_c \end{bmatrix}. \tag{2.4}$$

Vice versa:

$$\begin{bmatrix} f_a \\ f_b \\ f_c \end{bmatrix} = \mathbf{T}_{inv} \begin{bmatrix} f_d \\ f_q \end{bmatrix}. \tag{2.5}$$

Note that transformation of the variables, as defined by (2.1) and (2.2), preserves total system power: in every time instant, power in the *abc* reference frame is equal to the power in the *dq* reference frame.

Another comment needs to be made regarding zero variables, which generally must be taken into account when variables are transformed into the rotor reference frame. In our case, with a Y-connected generator without neutral connection, zero variables are always equal to zero, and are therefore excluded from representation.

When the machine's electrical equations are transformed from the *abc* to the *dq* reference frame, they assume the following form:

- Armature equations

$$v_d = -\mathrm{R_s} i_d - \omega\lambda_q - (\mathrm{L_{ls}} + \mathrm{L_{md}})\frac{di_d}{dt} + \mathrm{L_{md}}\frac{di_{fd}}{dt} + \mathrm{L_{md}}\frac{di_{kd}}{dt}, \tag{2.6}$$

$$v_q = -\mathrm{R_s} i_q + \omega\lambda_d - (\mathrm{L_{ls}} + \mathrm{L_{mq}})\frac{di_q}{dt} + \mathrm{L_{mq}}\frac{di_{kq}}{dt}, \tag{2.7}$$

where

$$\lambda_d = -(\mathrm{L_{ls}} + \mathrm{L_{md}})i_d + \mathrm{L_{md}}(i_{fd} + i_{kd}),$$

(2.8)

$$\lambda_q = -(\mathrm{L_{ls}} + \mathrm{L_{mq}})i_q + \mathrm{L_{mq}} i_{kq};$$

(2.9)

- Field equation

$$v_{fd} = \mathrm{R_{fd}} i_{fd} - \mathrm{L_{md}} \frac{di_d}{dt} + (\mathrm{L_{lfd}} + \mathrm{L_{md}}) \frac{di_{fd}}{dt} + \mathrm{L_{md}} \frac{di_{kd}}{dt};$$

(2.10)

- Damper winding equations

$$0 = \mathrm{R_{kd}} i_{kd} - \mathrm{L_{md}} \frac{di_d}{dt} + \mathrm{L_{md}} \frac{di_{fd}}{dt} + (\mathrm{L_{lkd}} + \mathrm{L_{md}}) \frac{di_{kd}}{dt},$$

(2.11)

$$0 = \mathrm{R_{kq}} i_{kq} - \mathrm{L_{mq}} \frac{di_q}{dt} + (\mathrm{L_{lkq}} + \mathrm{L_{mq}}) \frac{di_{kq}}{dt}.$$

(2.12)

Parameters and variables in the above equations have the following meanings:

- ω: rotor speed;
- v_d: armature *d* axis terminal voltage;
- v_q: armature *q* axis terminal voltage;
- i_d: armature *d* axis terminal current;
- i_q: armature *q* axis terminal current;
- v_{fd}: field winding terminal voltage (reflected to the stator);
- i_{fd}: field winding terminal current (reflected to the stator);
- i_{kd}: *d* axis damper winding current (reflected to the stator);
- i_{kq}: *q* axis damper winding current (reflected to the stator);

- λ_d: total armature flux in *d* axis;
- λ_q: total armature flux in *q* axis;
- R_s: armature phase resistance;
- L_{ls}: armature phase leakage inductance;
- L_{md}: *d* axis coupling inductance;
- R_{fd}: field winding resistance (reflected to the stator);
- L_{lfd}: field winding leakage inductance (reflected to the stator);
- R_{kd}: *d* axis damper wining resistance (reflected to the stator);
- L_{lkd}: *d* axis damper winding leakage inductance (reflected to the stator);
- L_{mq}: *q* axis coupling inductance;
- R_{kq}: *q* axis damper winding resistance (reflected to the stator);
- L_{lkq}: *q* axis damper winding leakage inductance (reflected to the stator).

Equations (2.6)-(2.12) describe the synchronous generator's equivalent circuit in the rotor reference frame shown in Fig. 2.1.

Several comments can be made regarding this equivalent circuit:

- *D* and *q* axis equivalent circuits are similar to a transformer equivalent circuit: in each of them, several windings, each characterized by some resistance and leakage inductance, are coupled through a mutual coupling inductance. The difference, compared to the transformer case, is that, while a transformer equivalent circuit is an ac circuit, here, when the generator is operating in sinusoidal steady state, all voltages, currents and flux linkages are dc.
- Even though armature windings are now represented in the rotor reference frame, and there are no time-variant inductances, the fact that armature windings are magnetically coupled is taken into account by presence of cross-coupling terms in the *d* and *q* axis's equivalent circuit's armature branch. For each axis, that term is

equal to the product of rotor speed and total flux linked with armature winding of the other axis.

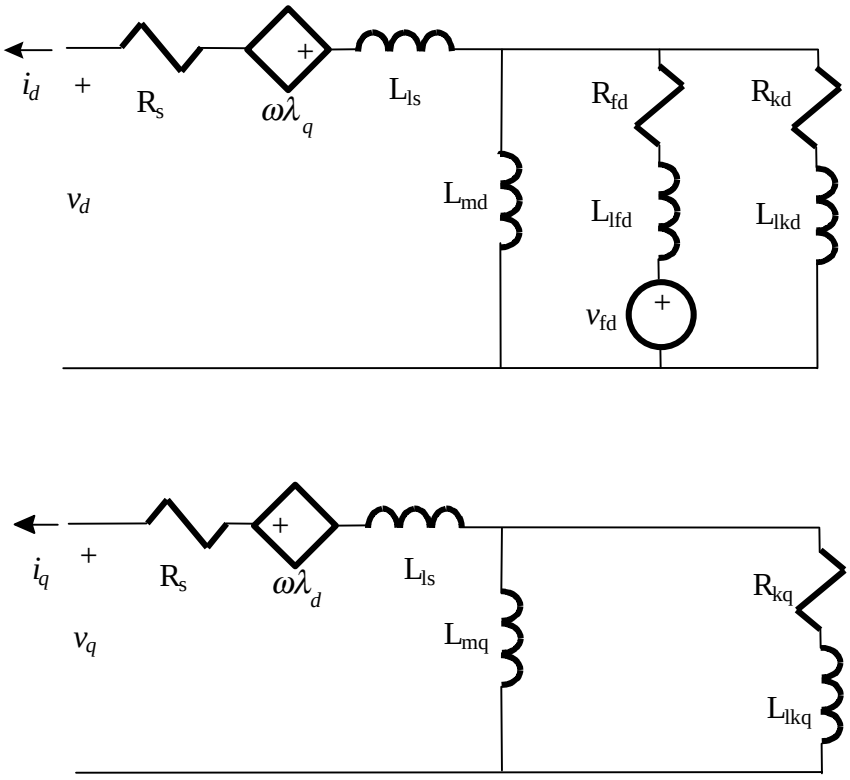

Fig. 2.1. Synchronous generator's equivalent circuit in rotor reference frame.

- If a machine (such as the exciter) has no damper windings, the equivalent circuit can be easily adapted by removing from it the branches representing damper windings. The rest of the circuit remains unchanged.
- All rotor parameters are reflected to armature. Therefore, when this circuit is used for simulation, and actual values of rotor variables are of interest, the turns ratio between the rotor and armature needs to be taken into account.

This equivalent circuit describes a synchronous generator electrically. The mechanical variable is represented by rotor speed ω, and the mechanical equation of the system is needed in order to complete the model. This equation relates the external torque applied to the generator's shaft to the electromagnetic torque that the machine develops internally. However, for the purpose of this thesis, the mechanical equation of the system is not considered, i.e. rotor speed is assumed to be known. The reason for that is the fact

that our interest consists primarily in describing electrical behavior of the generator loaded with a diode rectifier and a dc reactive load. To do that, it is legitimate to assume constant speed, since electrical transients in the machine can be considered much faster than mechanical transients (which involve the engine's dynamics and inertia and the generator's inertia). However, the main results of this work (the average model described in Chapter 4) will be verified at different values of rotor speed, in order to assure their validity.

With the above considerations, rotor speed ω is not a variable, but a parameter of the system. That causes (2.6)-(2.12) to be a set of linear differential equations.

2.1.3. Sinusoidal steady state operation

If a generator operates in sinusoidal steady state, phase voltages can be written in the *abc* reference frame as

$$v_a = V_p \cos\theta_v \,, \tag{2.13}$$

$$v_b = V_p \cos\left(\theta_v - \frac{2\pi}{3}\right), \tag{2.14}$$

$$v_c = V_p \cos\left(\theta_v + \frac{2\pi}{3}\right), \tag{2.15}$$

where

$$\theta_v = \omega_v t + \theta_{v0} \,. \tag{2.16}$$

In steady state, obviously, $\omega_v = \omega$. However, in order to reach a steady state, the generator must go through a transient during which the rotor electrical speed can be

different from the terminal voltage's angular frequency. That is the transient which allows the machine to reach the steady state value of rotor angle δ, defined as the displacement of the rotor referenced to the maximum positive value of the fundamental component of the terminal voltage of phase *a*. It can be expressed, in radians, as

$$\delta = \theta - \theta_v = \int_0^t (\omega(\xi) - \omega_v(\xi))d\xi + \theta(0) - \theta_v(0) . \tag{2.17}$$

Then, after applying (2.1) to (2.13)-(2.15), in the *dq* reference frame we have

$$v_d = \sqrt{\frac{3}{2}} V_p \sin(\theta - \theta_v) = \sqrt{\frac{3}{2}} V_p \sin\delta , \tag{2.18}$$

$$v_q = \sqrt{\frac{3}{2}} V_p \cos(\theta - \theta_v) = \sqrt{\frac{3}{2}} V_p \cos\delta . \tag{2.19}$$

Expressions (2.18) and (2.19) suggest that, in order to be able to represent *dq* reference frame variables and ac space vectors in the same diagram, a complex (Gaussian) plane be associated with the machine's 'physical' *dq* plane. The Gaussian plane's real axis is aligned with the machine's *q* axis, and the Gaussian plane's imaginary axis is aligned with machine's *d* axis. It can then be written

$$\overline{V} = \frac{1}{\sqrt{3}} (v_q + \bar{j} v_d) . \tag{2.20}$$

In (2.20), $\overline{V}$ represents the space vector associated to voltages v_a, v_b and v_c defined by (2.13)-(2.15), and $\bar{j}$ represents the unity vector in the direction of imaginary axis. Remember that the length of a space vector is assumed to be equal to the variable's rms value. Fig. 2.2 shows the position of the *dq* reference frame and space vector $\sqrt{3}\overline{V}$ at time *t=0*. Space vector $\sqrt{3}\overline{V}$ and *dq* reference frame rotate at constant speed ω in a

counterclockwise direction, and the instantaneous values of v_a, v_b and v_c are obtained as projections of $\sqrt{2}\bar{V}$ onto axes *a*, *b* and *c*, which are still.

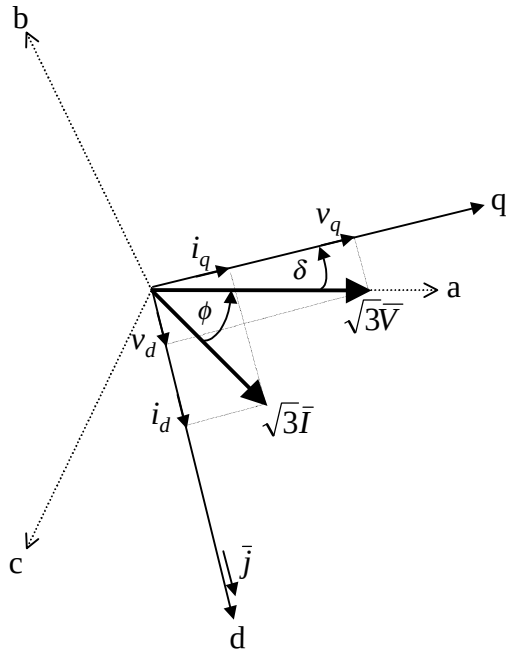

Fig. 2.2. Generator's space vector diagram for sinusoidal steady state operation.

Space vector $\sqrt{3}\bar{I}$, representing phase currents, is shifted by load angle ϕ with respect to $\bar{V}$. The instantaneous values of phase currents in the *abc* reference frame are obtained as projections of $\sqrt{2}\bar{I}$ onto axes *a*, *b* and *c*, and (constant) values of phase currents in the rotor reference frame are obtained as projections of the current space vector onto the *d* and *q* axis, which yields

$$i_d = \sqrt{\frac{3}{2}} I_p \sin(\delta + \phi), \tag{2.21}$$

$$i_q = \sqrt{\frac{3}{2}} I_p \cos(\delta + \phi), \tag{2.22}$$

where I_p stands for peak phase current.

2.1.4. Model implementation in a simulation software

Synchronous generator equivalent circuit in the rotor reference frame, shown in Fig. 2.1, is very convenient to simulate with any software that allows schematic descriptions of electric circuits, since only resistors, inductors and current dependent voltage sources need to be implemented. PSpice [10] was used for all simulation results in this thesis. Implementation of the circuit is straightforward, and only a few details will be given some attention in this section

Cross-coupling terms in armature branches contain total armature flux in *d* and *q* axis, given by (2.8) and (2.9). It is evident that these terms can be implemented using current-dependent voltage sources.

The generator model is implemented in the *dq* reference frame, but it is usually of practical interest to a have three-phase generator's output terminals available in a simulation process. That can be done by implementing the generator's output with three current-dependent current sources (Fig. 2.3), which generate currents in the *abc* reference frame by calculating them from armature currents in the *dq* reference frame as

$$\begin{bmatrix} i_a \\ i_b \\ i_c \end{bmatrix} = \mathbf{T}_{inv} \begin{bmatrix} i_d \\ i_q \end{bmatrix}. \tag{2.23}$$

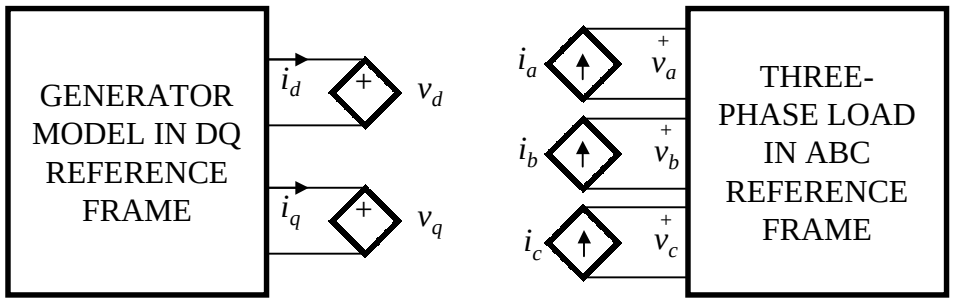

Fig. 2.3. Implementation of generator's three-phase output.

From the principle of duality, the generator model in the rotor reference frame is loaded with two voltage-dependent voltage sources (Fig. 2.3), representing the

generator's armature voltages in *dq* reference frame, and calculated from the generator's armature voltages in the *abc* reference frame as

$$\begin{bmatrix} v_d \\ v_q \end{bmatrix} = \mathbf{T} \begin{bmatrix} v_a \\ v_b \\ v_c \end{bmatrix}. \tag{2.24}$$

In order to be able to implement (2.23) and (2.24), rotor angle θ needs to be known. It can be calculated from (2.3), with the rotor speed represented by a current source charging a 1 F capacitor. Voltage across this capacitor is numerically equal to the rotor angle θ. The initial angle θ_0, if needed, can be implemented by an ideal dc voltage source in series with the capacitor.

One last comment regarding the generator's field voltage value. All rotor parameters and variables in model equations are referred to armature. However, for purposes of easy comparison of simulation with measurement results, it is convenient to implement the field voltage source in the simulation process as it actually exists in a real machine. To be able to do that, field-to-armature equivalent turns ratio *t* needs to be known. The following relationships exist between the actual field winding variables and field winding variables referred to armature (index 'act' denotes an actual field winding variable, i.e. the variable as it can be measured at field winding terminals):

$$v_{fd} = t v_{fdact}, \tag{2.25}$$

$$i_{fdact} = t i_{fd}. \tag{2.26}$$

These relationships can be implemented as shown in Fig. 2.4.

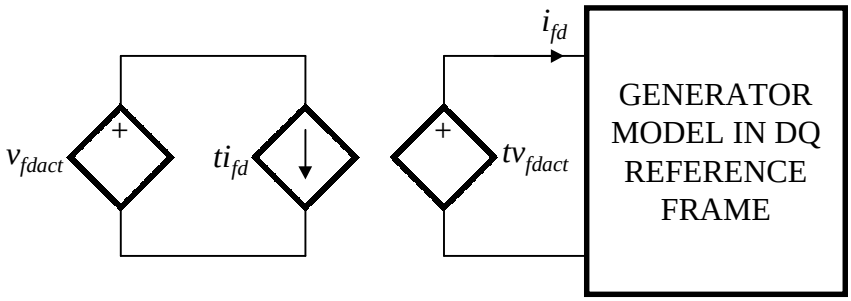

Fig. 2.4. Implementation of generator's field voltage.

2.2. Parameter identification

The synchronous generator equivalent circuit from Fig. 2.1 requires a large number of machine's parameters to be known. These parameters can be obtained from either the generator's design data or through measurements.

The two most common ways to measure a synchronous machine's parameters are short-circuit characteristics and standstill frequency response characteristics [8], [9], [13]-[19]. Both of these methods are based on determining the machine's parameters from the following standard inductances and time-constants:

- *D* axis synchronous inductance L_d

$$L_d = L_{ls} + L_{md};$$

(2.27)

- *D* axis transient inductance L_d'

$$L_d' = L_{ls} + \frac{L_{md} L_{lfd}}{L_{md} + L_{lfd}};$$

(2.28)

- *D* axis subtransient inductance L_d''

$$L_d'' = L_{ls} + \frac{L_{md}L_{lfd}L_{lkd}}{L_{md}L_{lfd} + L_{md}L_{lkd} + L_{lfd}L_{lkd}};$$

(2.29)

- *Q* axis synchronous inductance L_q

$$L_q = L_{ls} + L_{mq};$$

(2.30)

- *Q* axis subtransient inductance L_q''

$$L_q'' = L_{ls} + \frac{L_{mq}L_{lkq}}{L_{mq} + L_{lkq}};$$

(2.31)

- *D* axis open circuit transient time constant T'_{do}

$$T'_{do} = \frac{L_{lfd} + L_{md}}{R_{fd}};$$

(2.32)

- *D* axis short circuit transient time constant T'_d

$$T'_d = \frac{L_{lfd} + \frac{L_{md}L_{ls}}{L_{md} + L_{ls}}}{R_{fd}};$$

(2.33)

- *D* axis open circuit subtransient time constant T''_{do}

$$T''_{do} = \frac{L_{lkd} + \frac{L_{md}L_{lfd}}{L_{md} + L_{lfd}}}{R_{kd}};$$

(2.34)

- *D* axis short circuit subtransient time constant T''_d

$$T''_d = \frac{L_{lkd} + \frac{L_{md}L_{lfd}L_{ls}}{L_{md}L_{lfd} + L_{md}L_{ls} + L_{lfd}L_{ls}}}{R_{kd}};$$

(2.35)

- *Q* axis open circuit subtransient time constant T''_{qo}

$$T''_{qo} = \frac{L_{lkq} + L_{mq}}{R_{kq}};$$

(2.36)

- *Q* axis short circuit subtransient time constant T''_{q}

$$T''_{q} = \frac{L_{lkq} + \dfrac{L_{mq} L_{ls}}{L_{mq} + L_{ls}}}{R_{kq}}.$$

(2.37)

Measurement of short-circuit characteristics requires measurement of the waveform of the armature current immediately after a three-phase short circuit is performed at the armature terminals. During the transient, the machine is rotating at a constant speed, and field voltage is kept constant. From the measured armature current waveform, it is possible to extract the values of L_d, L_d'', T_d' and T_d'', and from them to calculate the *d* axis parameters. This method does not allow calculation of the parameters of the *q* axis.

Measurement of frequency response characteristics requires blocking the rotor in a position in which its *d* (or *q*) axis is aligned with the flux produced by the armature windings. With field winding shorted, frequency response is measured from the armature terminals. The obtained Bode plots allow to determine L_d, L_d'', L_q, L_q'', T_d', T_{do}', T_d'', T_{do}'', T_q'', T_{qo}'' and, from them, all parameters of the *d* and *q* axes.

In a system like the one shown in Fig. 1.1, it is difficult to perform any of these measurements. The reason for thist is that the exciter's armature terminals and main generator's field terminals are not accessible (they rotate with the shaft). Since detailed design data sheets were available for the main generator, all the main generator's parameters were extracted from these data sheets. In the exciter's case, no reliable design data sheets were available. Therefore, an exciter's stator and rotor (without a shaft) were obtained from the manufacturer, and some measurements, conceptually similar to standstill frequency response measurements, were done.

2.2.1. Main generator

Design data sheets resulted in the following values of the main generator's parameters at 145^{o}C:

- P= 4 poles;
- R_s=0.137 Ω;
- L_{ls}=0.897 mH;
- L_{md}=43.2 mH;
- R_{fd}=0.0266 Ω;
- L_{lfd}=3.37 mH;
- R_{kd}=0.120 Ω;
- L_{lkd}=0.164 mH;
- L_{mq}=20.8 mH;
- R_{kq}=0.120 Ω;
- L_{lkq}=0.347 mH;
- *t*=0.098.

2.2.2. Exciter

The exciter is a machine without damper windings, and that makes measurements of its parameters relatively easy. The parameters to be determined are R_s, L_{ls}, L_{md}, L_{mq}, R_{fd}, L_{lfd} and *t*. While R_s and R_{fdact} can be measured directly at the winding's terminals, L_{ls}, L_{md}, L_{mq}, L_{lfd} and R_{fd} can be calculated using (2.27)-(2.33), once L_d, $L_d^{'}$, $T^{'}_{do}$, $T^{'}_{d}$ and L_q are measured.

Measurement of L_d and L_d'

Consider the exciter with the rotor blocked and windings positioned as schematically shown in Fig. 2.5. With $\theta=0^o$, $\omega=0$ rad/s, the transformation matrix is

$$\mathbf{T}=\begin{bmatrix} 0 & -\frac{1}{\sqrt{2}} & \frac{1}{\sqrt{2}} \\ \sqrt{\frac{2}{3}} & -\frac{1}{\sqrt{6}} & -\frac{1}{\sqrt{6}} \end{bmatrix}, \tag{2.38}$$

while the inverse transformation matrix is

$$\mathbf{T}_{inv}=\begin{bmatrix} 0 & \sqrt{\frac{2}{3}} \\ -\frac{1}{\sqrt{2}} & -\frac{1}{\sqrt{6}} \\ \frac{1}{\sqrt{2}} & -\frac{1}{\sqrt{6}} \end{bmatrix}. \tag{2.39}$$

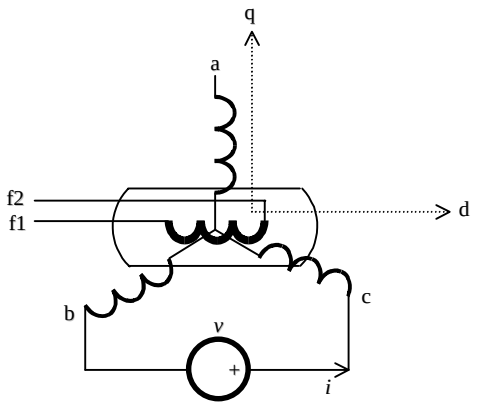

Fig. 2.5. Circuit for measurement of L_d and L_d'.

From Fig. 2.5, armature currents in the *abc* reference frame can be expressed as $i_a=0$, $i_b=i$, $i_c=-i$. Armature currents in the *dq* reference frame are easily calculated by applying (2.4), which yields $i_d=-\sqrt{2}i$, $i_q=0$. Then, if field winding terminals *f1* and *f2* are left open ($i_{fd}=0$), equations (2.6)-(2.12) are reduced to

$$v_d = -\mathrm{R}_s i_d - (\mathrm{L}_{\mathrm{ls}} + \mathrm{L}_{\mathrm{md}}) \frac{di_d}{dt} = \sqrt{2}\left[\mathrm{R}_s i + (\mathrm{L}_{\mathrm{ls}} + \mathrm{L}_{\mathrm{md}}) \frac{di}{dt} \right], \tag{2.40}$$

$$v_q = 0, \tag{2.41}$$

$$v_{fd} = -\mathrm{L}_{\mathrm{md}} \frac{di_d}{dt}. \tag{2.42}$$

Once v_d and v_q are known, v_a, v_b and v_c can be found from (2.5), yielding

$$v_a = 0, \tag{2.43}$$

$$v_b = -v_c = -\mathrm{R}_s i - (\mathrm{L}_{\mathrm{ls}} + \mathrm{L}_{\mathrm{md}}) \frac{di}{dt}. \tag{2.44}$$

Finally, supply voltage v can be expressed from v_b and v_c:

$$v = v_c - v_b = 2\left(\mathrm{R}_s i + (\mathrm{L}_{\mathrm{ls}} + \mathrm{L}_{\mathrm{md}}) \frac{di}{dt} \right). \tag{2.45}$$

If v is a sinusoidal voltage source of frequency ω_s, (2.45) can be rewritten in terms of phasors as

$$\frac{\overline{V}}{\bar{I}} = 2\left[\mathrm{R}_{\mathrm{s}} + j\omega_s(\mathrm{L}_{\mathrm{ls}} + \mathrm{L}_{\mathrm{md}})\right] = 2\left[\mathrm{R}_{\mathrm{s}} + j\omega_s \mathrm{L}_{\mathrm{d}}\right], \tag{2.46}$$

where L_{d} stands for the exciter's *d* axis synchronous inductance. It is clear now that, by measuring $\overline{V}$, $\bar{I}$ and R_{s}, it is possible to determine the value of L_{d}.

It can be shown that, in the same conditions as above, except for field winding terminals *f1* and *f2* being shorted instead of open (v_{fd}=0), the following is valid if $\mathrm{R}_{\mathrm{fd}} << \omega_s \mathrm{L}_{\mathrm{lfd}}$:

$$\frac{\overline{V}}{\overline{I}} \approx 2\left[R_s + j\omega_s (L_{ls} + \frac{L_{md} L_{lfd}}{L_{md} + L_{lfd}}) \right] = 2\left[R_s + j\omega_s L_d^{'} \right].$$

(2.47)

In this way, *d* axis transient inductance $L_d^{'}$ can be found.

Measurement of $T_{do}^{'}$ and $T_d^{'}$

D axis time constants $T_{do}^{'}$ and $T_d^{'}$ can be found from measurements performed at the field winding terminals. The configuration shown in Fig. 2.6 is used. Remember that time constants do not depend on whether they are referred to the rotor or to the armature. Therefore, it is allowable to draw conclusions from the machine's equations referred to the armature, but to perform measurements at the actual field winding terminals.

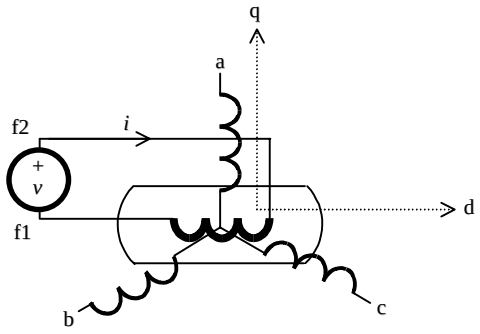

Fig. 2.6. Circuit for measurement of $T_{do}^{'}$ and $T_d^{'}$.

If the armature windings are left open, (2.10) immediately yields

$$v = R_{fd} i + (L_{lfd} + L_{md}) \frac{di}{dt},$$

(2.48)

or, written with phasors,

$$\frac{\overline{V}}{\overline{I}} = R_{fd} + j\omega_s (L_{lfd} + L_{md}) = \overline{Z}_{fdo}.$$

(2.49)

Then, as (2.32) suggests, the *d*-axis open-circuit transient time constant can be found from the resistive and inductive part of $\overline{Z}_{fdo}$.

If the armature terminals are shorted, the assumption that $R_s << \omega_s L_{ls}$ needs to be made in order to measure $T_d^{'}$. With $v_a=v_b=v_c=v_d=v_q=0$, and stator resistance R_s neglected, (2.6)-(2.10) yield

$$i_d = \frac{L_{md}}{L_{ls}+L_{md}} i_{fd} ,$$

(2.50)

$$i_q = 0 ,$$

(2.51)

$$v_{fd} = R_{fd} i_{fd} + \left(L_{lfd} + \frac{L_{md} L_{ls}}{L_{md}+L_{ls}} \right) \frac{di_{fd}}{dt} .$$

(2.52)

When (2.52) is written in terms of phasors, we obtain

$$\frac{\overline{V}}{\overline{I}} = R_{fd} + j\omega_s \left(L_{lfd} + \frac{L_{md} L_{ls}}{L_{md}+L_{ls}} \right) = \overline{Z}_{fd} .$$

(2.53)

Then, as (2.33) suggests, *d* axis short-circuit transient time constant can be found from the resistive and inductive part of $\overline{Z}_{fd}$.

Measurement of L_q

For measurement of the *q* axis parameters, the windings can still be positioned as in Fig. 2.5, but the armature terminals need to be connected as shown in Fig. 2.7. It has no importance, in this case, whether the field winding is left open or shorted, since no flux produced by the armature links the field winding.

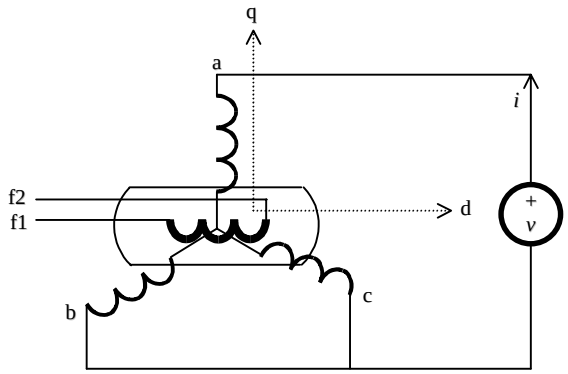

Fig. 2.7. Circuit for measurement of q axis parameters.

With the connection as in Fig. 2.7, *abc* reference frame armature currents are $i_a = -i$, $i_b = \frac{1}{2}i$, $i_c = \frac{1}{2}i$, which, by virtue of (2.4), yields i_d=0, $i_q = -\sqrt{\frac{3}{2}}i$. Then, from (2.6) and (2.7), armature voltages in rotor reference frame can be found as

$$v_d = 0\,,$$

(2.54)

$$v_q = -\mathrm{R_s} i_q - (\mathrm{L_{ls}} + \mathrm{L_{mq}})\frac{di_q}{dt} = \sqrt{\frac{3}{2}}\left[\mathrm{R_s} i + (\mathrm{L_{ls}} + \mathrm{L_{mq}})\frac{di}{dt}\right].$$

(2.55)

From (2.54) and (2.55), by using (2.5), the armature voltages in the *abc* reference frame are

$$v_a = \mathrm{R_s} i + (\mathrm{L_{ls}} + \mathrm{L_{mq}})\frac{di}{dt}\,,$$

(2.56)

$$v_b = v_c = -\frac{1}{2}\left[\mathrm{R_s} i + (\mathrm{L_{ls}} + \mathrm{L_{mq}})\frac{di}{dt}\right].$$

(2.57)

Since $v=v_a-v_b$, it can be written (in phasor terms)

$$\frac{\bar{V}}{\bar{I}} = \frac{3}{2}\left[\mathrm{R_s} + j\omega_s(\mathrm{L_{ls}} + \mathrm{L_{mq}})\right] = \frac{3}{2}(\mathrm{R_s} + j\omega_s \mathrm{L_q})\,,$$

(2.58)

which makes it clear that L_q can be found after $\bar{V}$, $\bar{I}$ and R_s are measured.

Note that where a factor of two was present in (2.46), expression (2.58) has a factor of 3/2. That can be intuitively explained by the way the armature phases are connected in Fig. 2.5 and Fig. 2.7.

The above-described measurements were performed at the available exciter's stator and rotor. Since there were no shaft and bearings, uniformity of the air gap was assured by inserting transformer paper between stator and rotor. Resistances were measured at dc and 25ºC, and ac measurements were performed at three different frequencies, in order to check for the effects of iron eddy currents. Since there is no standard way of dividing L_d into its two components, L_{ls} and L_{md}, it is assumed that L_{ls} represents 5% of the value of L_d. Table 2.1 summarizes the measurement results. It was found that eddy currents had no influence, since the measurements at all three frequencies gave very similar values.

Table 2.1. Measured exciter's parameters.

Parameter measured	Measured at dc	Measured at 60 Hz	Measured at 200 Hz	Measured at 400 Hz
R_s (Ω)	0.218			
R_{fdact} (Ω)	30.6			
L_d (mH)		2.43	2.43	2.42
L_d' (mH)		0.677	0.672	0.669
T_{do}' (s)		0.026	0.026	0.026
T_d' (s)		0.0086	0.0077	0.0076
L_q (mH)		2.38	2.37	2.37

The following parameter values (at 145ºC) were used when exciter operation was simulated:

- P= 8 poles;
- R_s=0.218 Ω;
- L_{ls}=0.122 mH;
- L_{md}=2.31 mH;
- R_{fd}=0.123 Ω;
- L_{lfd}=0.845 mH;
- L_{mq}=2.25 mH;
- *t*=0.063.

Chapter 3. Switching Model

3.1. Introduction

The switching model of a diode bridge-loaded synchronous generator (which will also be referred to as a generator/rectifier switching model) is obtained when a three-phase diode bridge is connected to the generator's three-phase output implemented in a simulation software, as shown in Fig. 3.1. The main purpose of time-domain simulations of the switching model is to see how an electronic (diode-rectifier) load affects the generator's ac waveforms; the model's switching nature makes it unsuitable for linearization and control-purpose applications. Also, because of the need to keep the maximum simulation time-step well below the switching period, these simulations are time- and memory consuming.

Fig. 3.2 shows the block diagram of the system whose switching model was simulated. It differs from the one shown in Fig. 1.1 in the fact that the engine is excluded from the model, the generator speed is set as a model parameter, and the main generator's dc load is represented by a resistor (instead of an inverter). Since our primary interest is to show the exciter's and main generator's ac waveforms, these simplifications are legitimate.

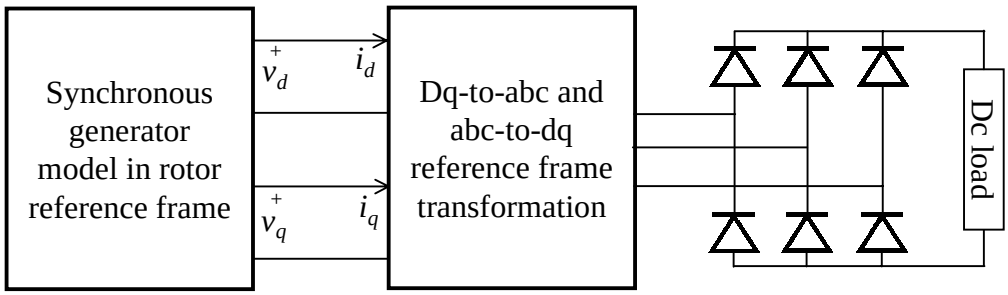

Fig. 3.1. Generator/rectifier switching model.

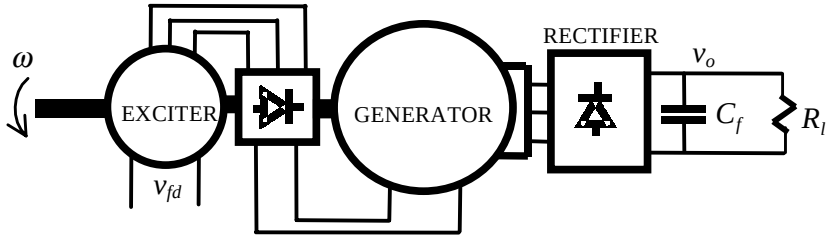

Fig. 3.2. Block diagram of the simulated system.

3.2. Simulation and experimental results

It is convenient to simulate the system shown in Fig. 3.2 under different operating conditions (values of speed ω and load R_l) in order to see how the main generator's ac waveforms are affected by diode-rectifier load. Two cases are shown in Fig. 3.3 and Fig. 3.4. They represent the main generator's line-to-line voltage and phase current at two different speeds (2280 rpm and 3340 rpm) and different resistive dc loads (34 kW and 100 kW). In both cases, the exciter's field voltage was set to an appropriate value in order to obtain 800 V at the dc-link.

The simulation results shown in Fig. 3.3 and Fig. 3.4 are to be compared with the measurement results, shown in Fig. 3.5 and Fig. 3.6, respectively. It can be seen that the measured waveforms closely match the simulation results.

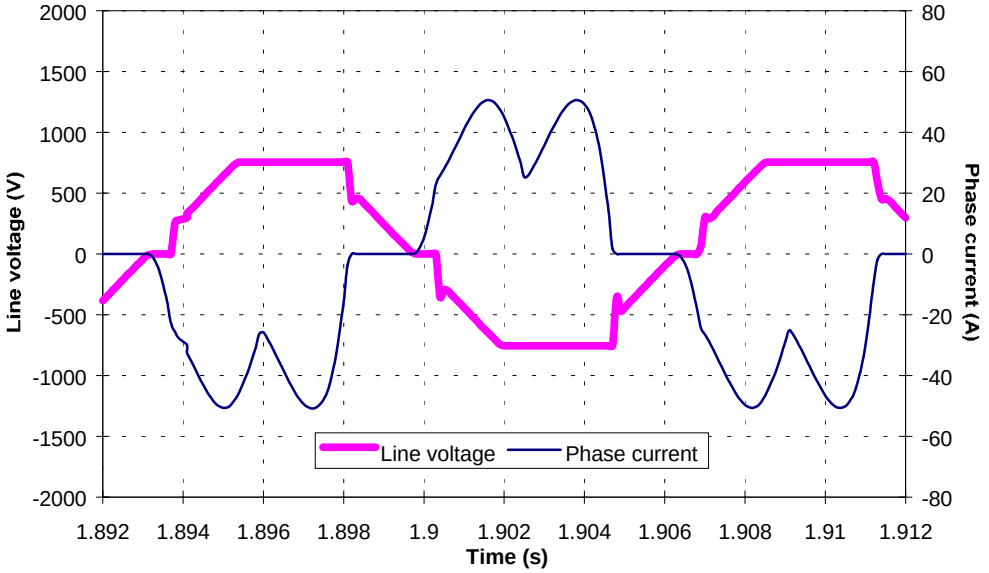

Fig. 3.3. Switching model simulation: the main generator's line voltage and phase current (n=2280 rpm, R_l=19 Ω, v_{fd}=16 V).

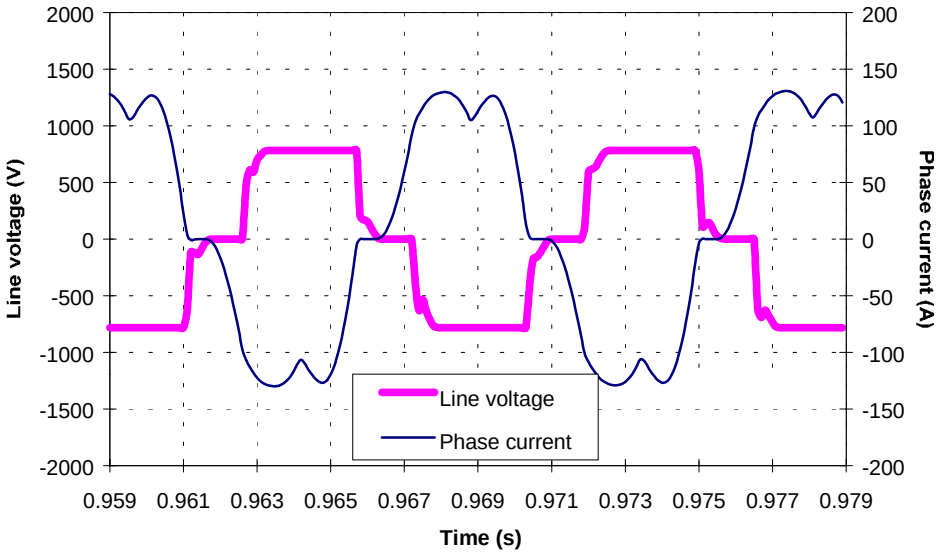

Fig. 3.4. Switching model simulation: the main generator's line voltage and phase current (n=3340 rpm, R_l=6.4 Ω, v_{fd}=33 V).

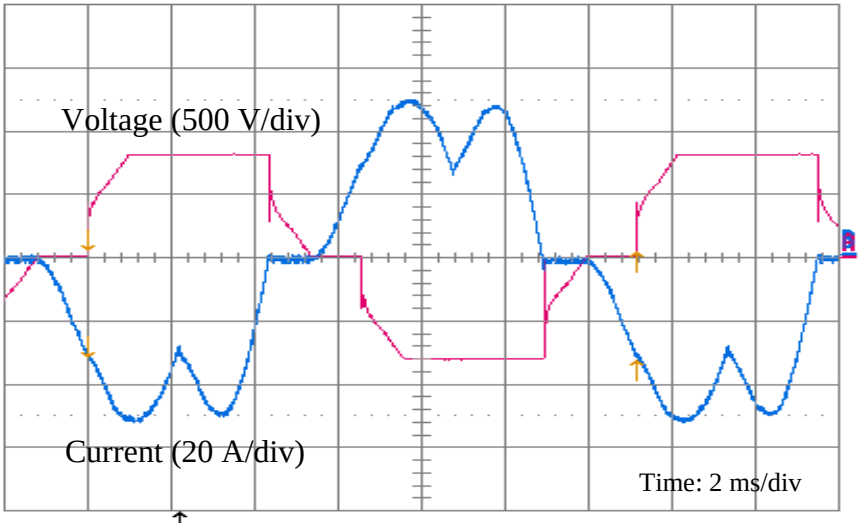

Fig. 3.5. Measurement: the main generator's line voltage and phase current (n=2280 rpm, R_l=19 Ω, v_{fd}=15.2 V).

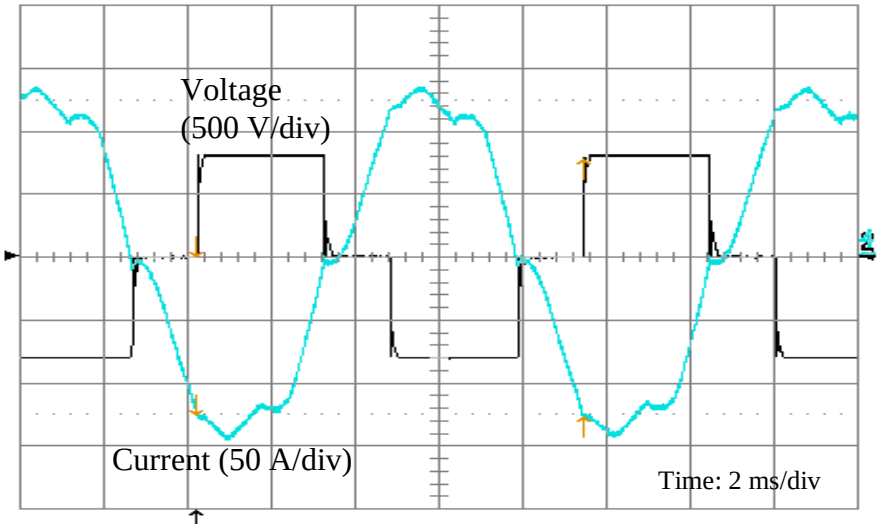

Fig. 3.6. Measurement: the main generator's line voltage and phase current (n=3340 rpm, R_l=6.4 Ω, v_{fd}=31 V).

Several remarks can be made regarding the waveforms shown in Fig. 3.3, Fig. 3.4, Fig. 3.5 and Fig. 3.6. Line-to-line voltage waveforms in these pictures have a 'flat' top, due to the simultaneous conduction of three diodes, and the presence of a large capacitor connected across the dc-link. The generator's inductance causes diode commutation to last for a considerable portion of the ac period. During commutation, three diodes are conducting in the diode bridge, which means that one of the generator's line-to-line voltages is equal to zero; the other two are equal to v_{dc} and $-v_{dc}$, where v_{dc} is the voltage

across the dc-link capacitor. That voltage does not practically change over an ac period, which results in the line-to-line voltage waveform's flat top. Therefore, the main generator's line voltages are shaped by its dc load, dominated by a large capacitor. Note that as generator speed increases (ac period decreases) and dc load current increases, the duration of commutation becomes relatively longer with respect to the ac period. That continues until diode commutation requires 60 electrical degrees, and line-to-line voltage shows no more sinusoidal portions, but is a quasi-square waveform (Fig. 3.4 and Fig. 3.6). If the ac period were further reduced, and/or the load current were further increased, it could be expected that the commutation angle would exceed 60°. However, no such conditions were experienced with the studied system. The phase current waveform shown in Fig. 3.3, Fig. 3.4, Fig. 3.5 and Fig. 3.6 is a consequence of applied voltage conditions, and no immediate intuitive explanation can be associated with it.

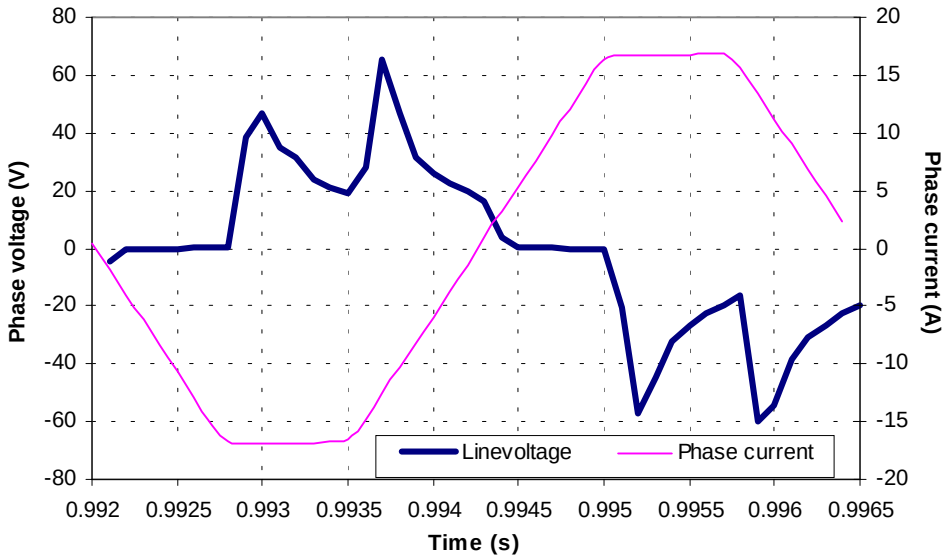

Fig. 3.7. Switching model simulation: the exciter's line-to-line voltage and phase current (n=3340 rpm, R_l=6.4 Ω, v_{fd}=33 V).

The exciter's voltage and the current waveforms obtained with the switching model simulation are shown in Fig. 3.7. It was not possible to measure the exciter's armature voltage and current waveforms because of the inaccessibility of the exciter's armature windings. In Fig. 3.7, the exciter's diode bridge already operates with the 60° commutation angle, but the waveforms are very different from the ones relative to the

main generator, due to the nature of the exciter's dc load. It is a heavily inductive load (the main generator's field winding), which causes the output dc current to be practically constant over one exciter's ac period. Because of that, and because of the 60° diode commutation angle, the exciter's phase currents have a trapezoidal form as shown in Fig. 3.7. The line-to-line voltage waveform is a consequence of such currents, and it is not subject to an intuitive explanation. Dually to main generator's case, the exciter's phase currents are shaped by its primarily inductive dc load.

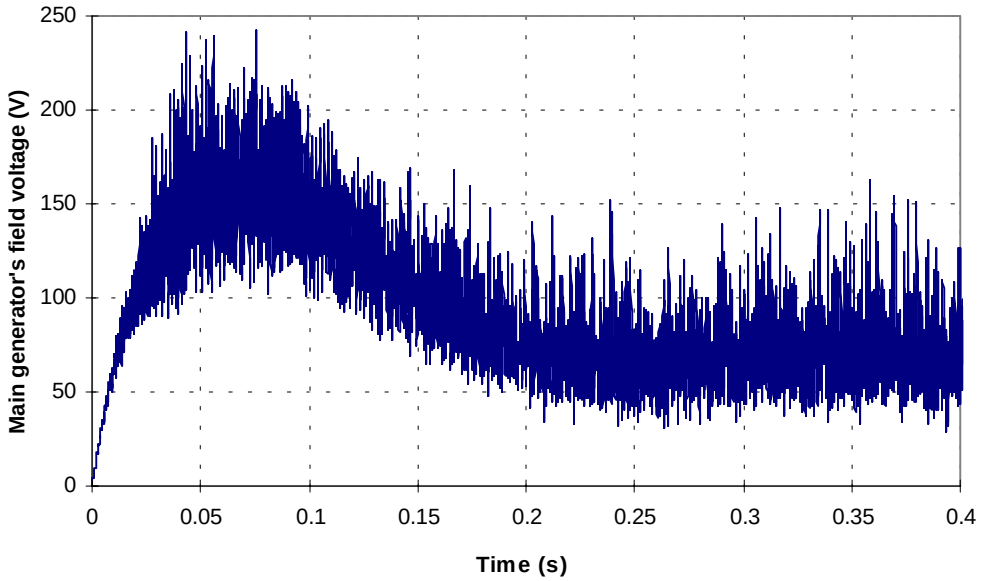

Fig. 3.8. Switching model simulation: the main generator's field voltage at exciter's field voltage step from 0 V to 47.5 V (n=4000 rpm, R_l=4.27 Ω).

All figures in this section show the machine's ac variables in steady state. In order to reach a steady state of interest, a long initial transient needs to be simulated. It is illustrative to consider one of the system's dc variables during such a transient. Fig. 3.8 shows the main generator's field voltage (output voltage of exciter's diode bridge) during transient caused by a step in exciter's field voltage. Note that the waveform consists of an average component on which is superimposed a large amount of the switching ripple. It will be argued in the following section that only the average component of such a waveform has importance regarding power transfer and the system's dynamic behavior; the ripple is a consequence of the exchange of reactive power between various parts of the system. Therefore, a representation of a system that accounts for the average component of a dc waveform, but excludes the ripple, would be valid and meaningful for

the system's analysis. It would also save simulation time, and offer some possibilities (linearization) that are not inherent to the switching model. Such 'ripple-free' representation will be made possible by the average model presented in the following chapter. It is necessary, however, for the average model to take into account the effects of non-ideal operation of the system. In order to identify and correctly quantify these effects, an analysis of the switching model simulation results need to be conducted.

3.3. Analysis of switching model results

It was mentioned in the introductory chapter that, with a generator operating in conditions such as those shown in Fig. 3.5 and Fig. 3.6, a phase-shift exists between the fundamental harmonic of the generator's phase voltage and phase current. In the system studied, it was not possible to measure the generator's phase voltage waveform because of the absence of a neutral connection. In such a case, switching model simulation offers a precise means of obtaining phase voltage waveforms, shown (together with phase current) in Fig. 3.9 and Fig. 3.10 for the main generator and in Fig. 3.11 for the exciter. It is evident from these figures that there is a considerable phase shift between the fundamental harmonic of the two waveforms; however it is also evident that, due to the complexity of the waveforms, it is practically impossible to evaluate the phase shift analytically. Numerical evaluation is made possible by using the results of the switching model simulations and the generator's space vector diagram. Prior to explaining how this numerical evaluation can be carried out, it is useful to discuss the role of the current's and voltage's higher harmonics (harmonics other than fundamental) in the power transfer occurring from the generator to the dc output of the diode rectifier.

On the ac side of the rectifier, higher current harmonics are caused by diode non-linearity. Higher voltage harmonics are due to the voltage drop, caused by the higher harmonics of the current, across generator's impedance. Since this impedance is primarily inductive, for each harmonic other than the fundamental, the voltage will be

shifted by practically 90° with respect to the current. Therefore, active power associated with higher harmonics at the rectifier's ac side can be considered negligible.

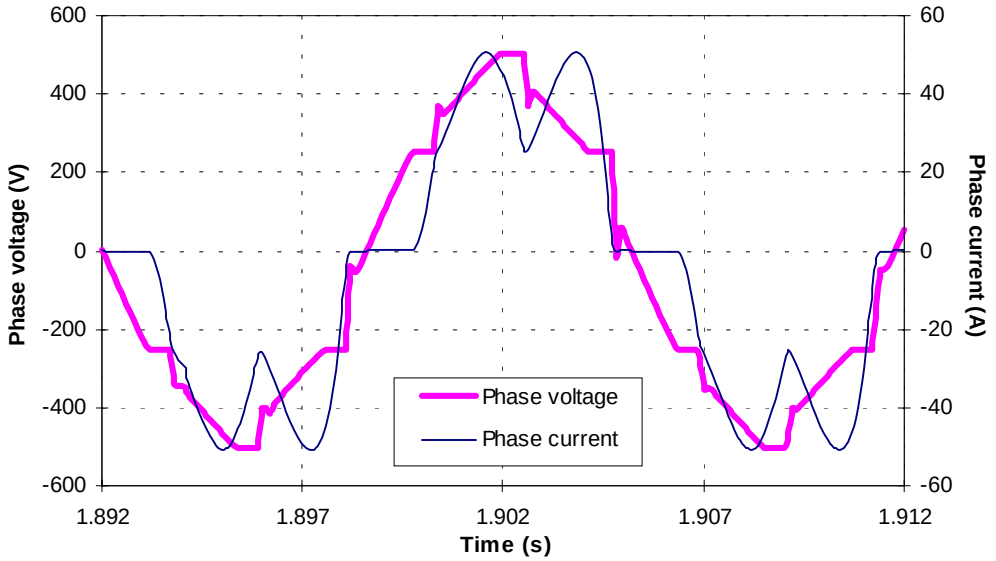

Fig. 3.9. Switching model simulation: the main generator's phase voltage and phase current (n=2280 rpm, R_l=19 Ω, v_{fd}=16 V).

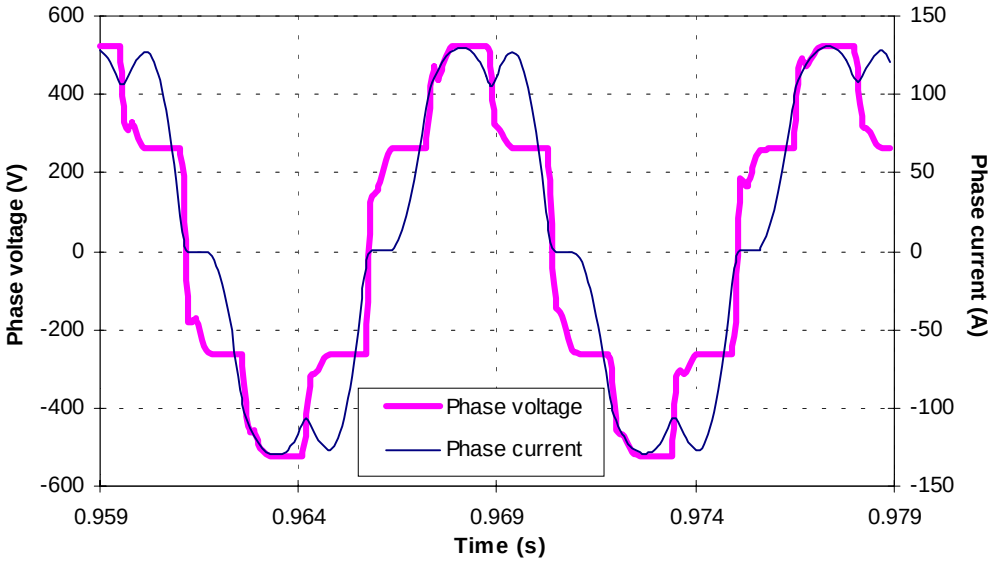

Fig. 3.10. Switching model simulation: the main generator's phase voltage and phase current (n=3340 rpm, R_l=6.4 Ω, v_{fd}=33 V).

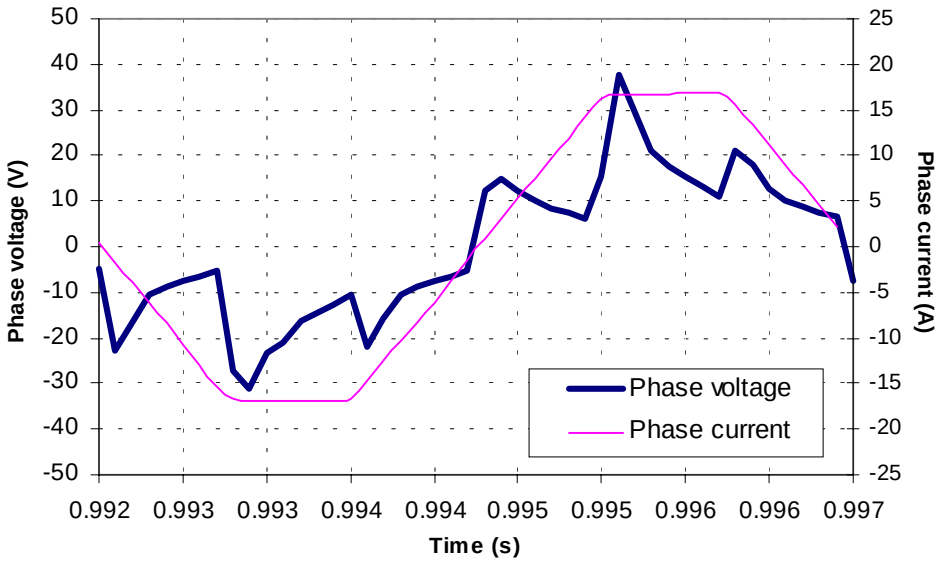

Fig. 3.11. Switching model simulation: the exciter's phase voltage and phase current (n=3340 rpm, R_l=6.4 Ω, v_{fd}=33 V).

At the dc side of diode rectifier, the dc voltage and current consist of an average value and a certain ripple superimposed on it. One of two dc variables, however, is almost ripple-free: it is the dc current in the exciter's case, due to the heavily inductive main generator's field winding; it is dc voltage in the case of the main generator, due to a large dc-link capacitor. Therefore, power associated with ripple voltage and current at the dc side of the rectifier can be neglected, compared to the power associated with the output variables' average values.

It is possible now to proceed with an explanation of how the generator's space vector diagram can be drawn when steady state ac waveforms consist of a fundamental and higher harmonics. Because of higher harmonics present in ac waveforms, steady state currents and voltages in the *dq* reference frame are not constants, but dc variables consisting of an average value to which a ripple (at a frequency equal to six times the generator terminal frequency) is added. For example, the main generator's *d* axis armature voltage and current are shown in Fig. 3.12. In these conditions, and according to the above discussion regarding the importance of higher harmonics for power transfer, the generator's space vector diagram can still be drawn, but *d* and *q* axis armature variables are represented by their average values, i.e. ac variables are represented by their

fundamental harmonics. That is shown in Fig. 3.13, where $\hat{x}$ denotes the steady state average value of variable x, and index '1' refers to the fundamental harmonic of an ac variable. From Fig. 3.13, phase shift ϕ between the fundamental harmonics of generator's voltage and current can be evaluated as

$$\phi = \arctan\frac{\hat{i}_d}{\hat{i}_q} - \arctan\frac{\hat{v}_d}{\hat{v}_q}. \tag{3.1}$$

The operating point of the system is defined by the main generator's load and engine speed. These two, however, are related through a linear dependence as shown in Fig. 3.14. That kind of relationship is considered optimal for the engine, and will be used in this section whenever the dependence of a certain parameter on the operating point is investigated.

Fig. 3.15 shows how ϕ varies with system's operating point. In order to obtain these results, the switching model was simulated and the steady state average values of i_d, i_q, v_d and v_q were found, after which ϕ was computed from (3.1). The dependence of ϕ on the operating point will be important for the development of the generator/rectifier average model, carried out in the following chapter.

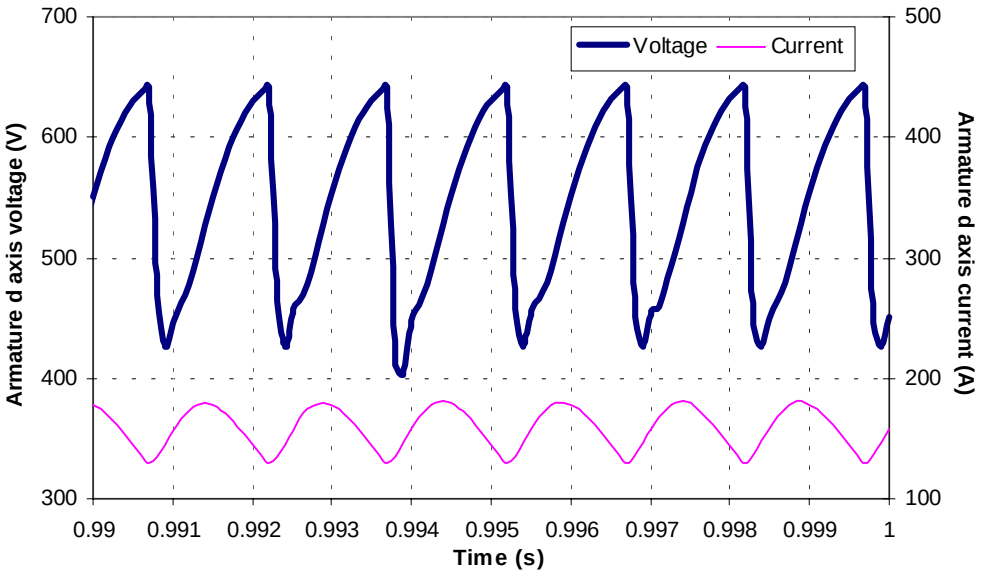

Fig. 3.12. Switching model simulation: the main generator's steady state armature d-axis voltage and current.

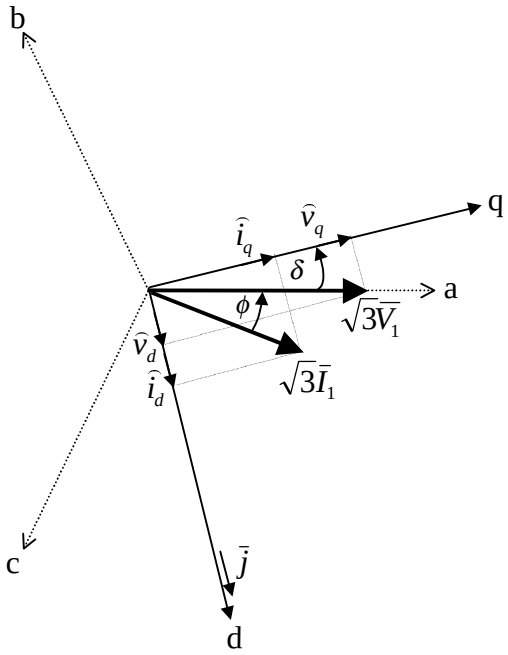

Fig. 3.13. Generator's space vector diagram for non-sinusoidal steady state.

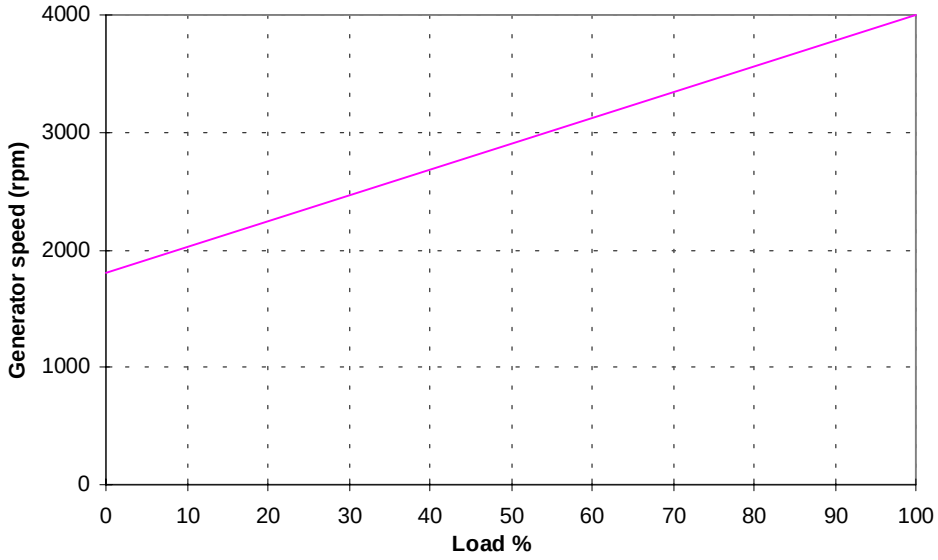

Fig. 3.14. Engine speed as function of the main generator's load, defining operating points (100%=150 kW).

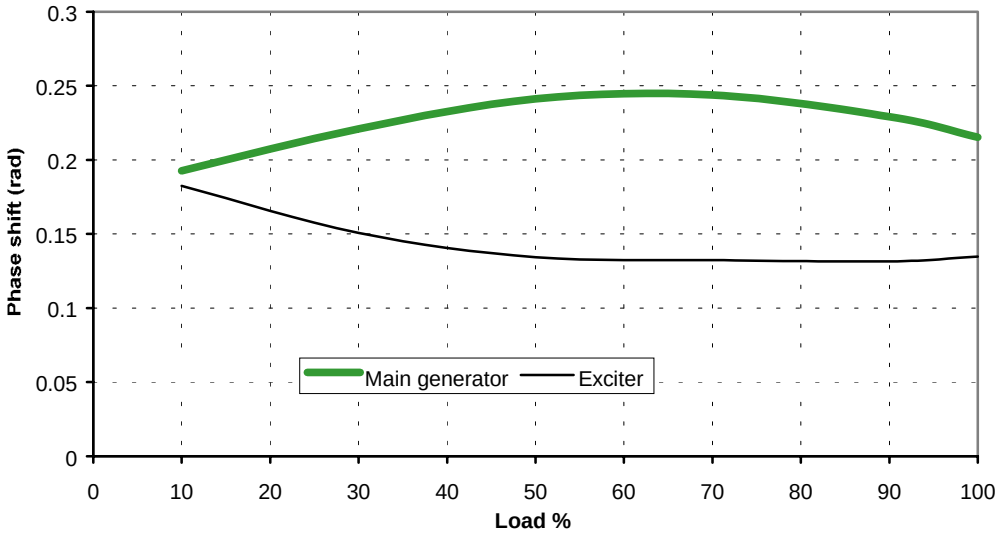

Fig. 3.15. Variation of ϕ with the operating point.

For the development of the generator/rectifier average model, it is also interesting to study how the average value of the rectifier's output dc voltage and current can be related to the average values of the armature voltages and currents in the *dq* reference frame. If the generator were an ideal voltage source, by combining (1.1) with (2.18) and (2.19), the following expression can be found:

$$\widehat{v}_{dc} = \frac{3\sqrt{2}}{\pi}\sqrt{v_d^2 + v_q^2} = \frac{3\sqrt{2}}{\pi}\sqrt{\widehat{v}_d^2 + \widehat{v}_q^2} \approx 1.35\sqrt{\widehat{v}_d^2 + \widehat{v}_q^2}\ . \tag{3.2}$$

Similarly, with an ideal voltage source generator and a dc current source load, from (1.2) and the space vector diagram in Fig. 3.13, a relationship for currents can be obtained:

$$I_{dc} = \frac{\pi}{3\sqrt{2}}\sqrt{\widehat{i}_d^{\,2} + \widehat{i}_q^{\,2}} \approx 0.74\sqrt{\widehat{i}_d^{\,2} + \widehat{i}_q^{\,2}}\ . \tag{3.3}$$

In the actual case, when the generator is not ideal and the dc load is not a constant current source, it can be assumed that these relationships preserve the same form; however, the value of the constants that relate the rectifier's output variables to the generator's average *dq* variables will have to be changed. The switching model

simulation can be used in order to evaluate numerically these constants (named k_v for voltages and k_i for currents) according to the following expressions:

$$k_v = \frac{\hat{v}_{dc}}{\sqrt{\hat{v}_d^2 + \hat{v}_q^2}}, \tag{3.4}$$

$$k_i = \frac{\hat{i}_{dc}}{\sqrt{\hat{i}_d^2 + \hat{i}_q^2}}. \tag{3.5}$$

Fig. 3.16 and Fig. 3.17 show the variation of k_v and k_i, respectively, with the operating point, for the main generator and the exciter. It is interesting to note that, for the main generator at light load, constant k_v is practically equal to 1.35, which is its ideal value. That is due to the fact that, at light load and low generator speed, distortion in the main generator's terminal voltage is minimal. The exciter's k_v, however, does not show the same behavior at light load. That can be attributed to the forward voltage drop across the diodes in the exciter's rectifier bridge. At light load, the exciter needs to provide only several volts of the main generator's field voltage. In these conditions, the forward voltage drop across two diodes (which are in serial connection with the exciter's armature windings) is a significant portion of the exciter's phase voltage. Therefore, in order to provide the needed main generator's field voltage, the exciter's phase voltages need to be somewhat larger compared to the ideal case characterized by the zero diode forward voltage drop. Consequently, when the exciter's k_v at low load is calculated from (3.4), the resulting value is significantly smaller than in the ideal case. The difference between the ideal and non-ideal value of k_v gets relatively smaller as the load increases, because the exciter's phase voltage becomes much larger than the diode forward voltage drop. That is also why the effect of the diode forward voltage drop is practically negligible in main generator's case.

Calculation of k_i is not directly affected by diode non-ideality, and both the exciter's and main generator's k_i show the same type of load dependence. Their discrepancy from the ideal value (equal to 0.74) can only be attributed to phase current waveforms being different from the one shown in Fig. 1.3.

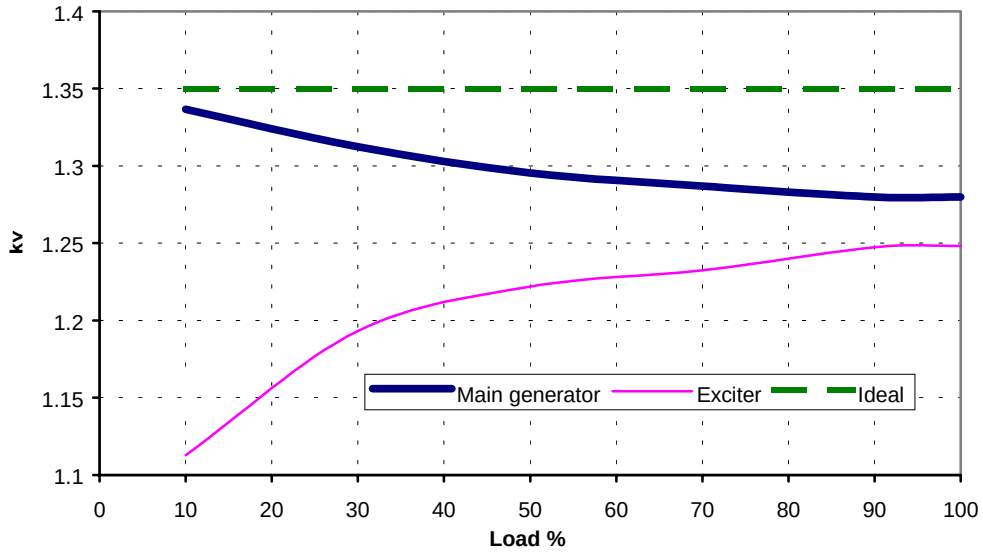

Fig. 3.16. Variation of k_v with the operating point.

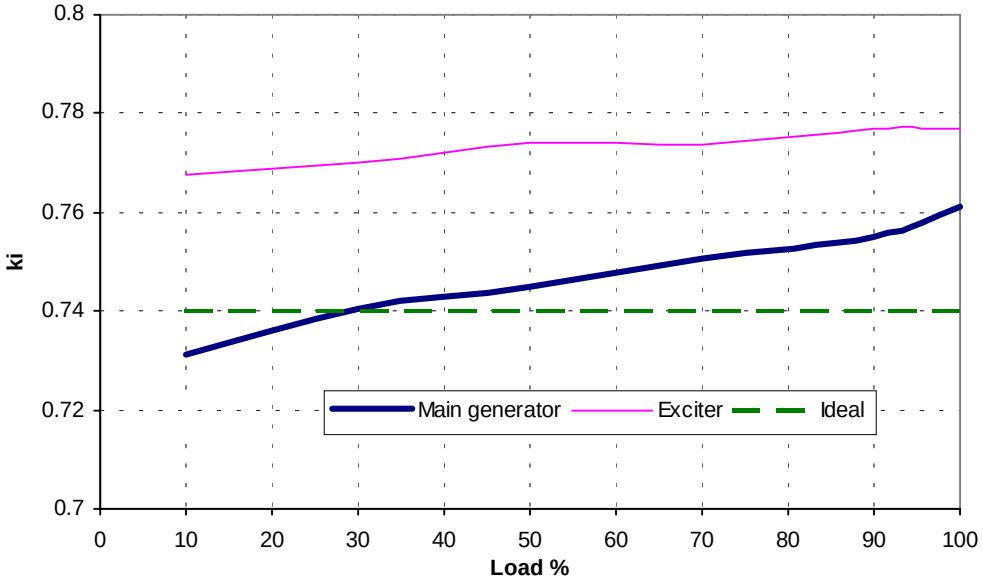

Fig. 3.17. Variation of k_i with the operating point.

The influence of the diode forward voltage drop will be addressed again in Section 4.4.2, when the validity of generator/rectifier average model will be discussed.

The above discussion on the meaning and load-dependence of ϕ, k_v and k_i represents the basis for the development of the average model of a diode bridge-loaded synchronous generator (also referred to as the generator/rectifier average model), contained in Chapter 4.

Chapter 4. Average Model

4.1. Concept of the average model

The higher harmonics present in the generator's ac variables need to be taken into account and studied in detail for certain purposes, such as, for example, evaluation of additional generator losses caused by them. However, as was already mentioned in section 3.3, they can be ignored from the point of view of the main power transfer from the generator to the dc-link. The same statement can be made regarding their importance for the generator's dynamic performance, which is determined primarily by the fundamental harmonic of ac voltage and current. For example, when the dc-link control-loop of the system in Fig. 1.6 needs to be designed, the objective is to control the average value of the dc-link voltage, i.e. the fundamental harmonic of the generator's ac voltage. The ripple present in dc (or *dq* reference frame) variables, and harmonics other than fundamental in ac variables, are characterized by frequencies too high to affect the machine's dynamic behavior and to be dealt with by the field control-loop.

For the above reasons, it would be useful to have an 'average' model of a diode bridge-loaded synchronous generator, i.e. a model that would take into account only fundamental harmonic of the ac variables, and the average value of dc (or rotor reference

frame) variables [20], [21]. The model should also take into account the effects that the non-ideal operation of the diode bridge has on fundamental harmonic and average values.

Before proceeding, a clarification regarding the meaning of the term ‘average’ in this text is necessary. A more appropriate term to describe what is intended here would be ‘moving average’ [1] which, for a generic periodic variable x of period T, can be defined as

$$\hat{x}(t) = \frac{1}{T}\int_{t-T}^{t} x(\xi)d\xi \,. \tag{4.1}$$

Applied to the case dealt with in this text, (4.1) means that the process of averaging removes the ripple from all dc or rotor reference frame variables. What remains is a ‘smooth’ variable that assumes the role of instantaneous value of the actual variable, and can be affected by any transient characterized by frequencies smaller than $1/(2T)$, where $T=1/(6f)$, f being the generator’s ac frequency. Transients occurring at frequencies larger than $1/(2T)$ are lost in the process of averaging. However, the synchronous generator’s dominant characteristic frequencies are, as a rule, well below $3f$. Therefore, it can be expected that all important dynamic characteristics of the synchronous generator will be preserved in the averaging process.

It can be noticed that the symbol used in (4.1) for moving average is the same one used in (3.1)-(3.5) for steady state average. It was chosen because the steady state average can be considered only a special case of the more generic moving average.

It is possible now to proceed with presenting the approach that is going to be used to develop the generator/rectifier average model. In [21], an average model of a system consisting of a three-phase voltage source, rectifier, inverter and synchronous motor is presented. It involves describing the rectifier and inverter in a reference frame rotating synchronously with source voltages, while the synchronous motor is desribed in a reference frame rotating synchronously with its rotor. Transformation from one to another reference frame is then established by means of rotor angle δ.

A similar method will be applied here in order to develop an average model of a diode-bridge loaded synchronous generator: the rectifier's dc output will be expressed in a reference frame rotating synchronously with the generator's terminal voltages. Rotor displacement angle δ will then be used to relate it to the generator's variables in rotor reference frame.

In development of the average model, switching model simulation results from Section 3.3 are used. The main conclusions from this section, indispensable for development of the average model, are repeated here for convenience:

- Power transfer and the system's dynamic behavior are determined primarily by the fundamental harmonic of ac variables and the average component of dc variables.
- Due to the reactive nature of the generator's impedance and dc load, there exists a phase shift ϕ between the fundamental harmonics of the generator's phase voltage and phase current. The amount of phase shift can be determined from the switching model simulation results.
- In spite of non-ideal operation of the rectifier, it can be assumed that average values of rectifier's output voltage and current are proportional to the fundamental harmonic of the generator's phase voltage and current through constants k_v and k_i, respectively. Values of these constants need to be determined numerically from switching model simulation results.

Based on the above conclusions, development of the average model is carried out in two steps, which are discussed in the following section:

- The generator's armature variables in rotor reference frame and the rectifier's output variables are represented together in the system's space vector's diagram by means of k_v, k_i and ϕ.
- Appropriate equations (following from the geometry of the system's space-vector diagram) are selected as the average model's equations.

4.2. Formulation of average model equations

4.2.1. System space-vector diagram

It was shown in Fig. 3.13 how the generator's space vector diagram can be drawn by taking into account the average values of variables in the rotor reference frame, and the fundamental harmonic of ac variables. It is possible now to move one step further, and to include vectors representing the average values of the diode bridge's output variables in the same diagram. According to (3.4) and (3.5), that is possible by simply replacing space vectors $\sqrt{3}\overline{V}_1$ and $\sqrt{3}\overline{I}_1$ in Fig. 3.13 with vectors whose lengths are $\hat{v}_{dc}/k_v$ and $\hat{i}_{dc}/k_i$, respectively. The resulting generator/rectifier space vector diagram is shown in Fig. 4.1. Axes *a*, *b* and *c* were omitted from representation in Fig. 4.1, since no three-phase variables are shown.

The following expressions can be obtained from Fig. 4.1:

$$\hat{v}_{dc} = k_v(\hat{v}_d \sin\delta + \hat{v}_q \cos\delta), \tag{4.2}$$

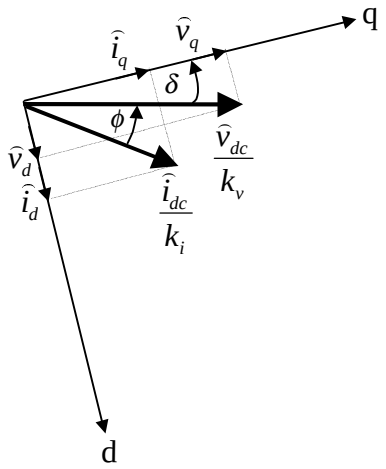

Fig. 4.1. Generator/rectifier space vector diagram.

$$\hat{i}_{dc} = k_i\left[\hat{i}_d \sin(\delta+\phi) + \hat{i}_q \cos(\delta+\phi)\right], \tag{4.3}$$

$$\hat{v}_d = \frac{\hat{v}_{dc}}{k_v}\sin\delta\,, \tag{4.4}$$

$$\hat{v}_q = \frac{\hat{v}_{dc}}{k_v}\cos\delta\,, \tag{4.5}$$

$$\hat{i}_d = \frac{\hat{i}_{dc}}{k_v}\sin(\delta+\phi)\,, \tag{4.6}$$

$$\hat{i}_q = \frac{\hat{i}_{dc}}{k_v}\cos(\delta+\phi)\,. \tag{4.7}$$

Strictly speaking, Fig. 4.1 and (4.2)-(4.7) describe, in an average sense, a certain steady state operating point, because the values of ϕ, k_v and k_i change as the operating point changes. However, from Fig. 3.15, Fig. 3.16 and Fig. 3.17, it can be seen that their variation with the operating point is not significant. It can, therefore, be assumed that (4.2)-(4.7) will be valid during transients, too, as long as values of ϕ, k_v and k_i corresponding to a 'medium' operating point (for example, 50% of rated load) are selected. If it is known in advance that transient will occur in the proximity of a particular operating point, it is possible to select more appropriate values of ϕ, k_v and k_i relative to it, thus making (4.2)-(4.7) a more accurate representation of the system.

4.2.2. Average model equations

It is possible now to select appropriate expressions among (4.2)-(4.7) in order to implement the average generator/rectifier model, whose block diagram is shown in Fig.

4.2. The dc source can be either a voltage or a current source, and its expression is obtained from (4.2) or (4.3), respectively. The *d* and *q* axis load can be given by either current or voltage sources, and their expressions are calculated from (4.6)-(4.7), or (4.4)-(4.5), respectively. This results in two dual sets of average model equations:

- Set 1

$$\hat{v}_{dc} = k_v(\hat{v}_d \sin\delta + \hat{v}_q \cos\delta), \tag{4.8}$$

$$\hat{i}_d = \frac{\hat{i}_{dc}}{k_i}\sin(\delta+\phi), \tag{4.9}$$

$$\hat{i}_q = \frac{\hat{i}_{dc}}{k_i}\cos(\delta+\phi), \tag{4.10}$$

$$\delta = \arctan\frac{\hat{v}_d}{\hat{v}_q}. \tag{4.11}$$

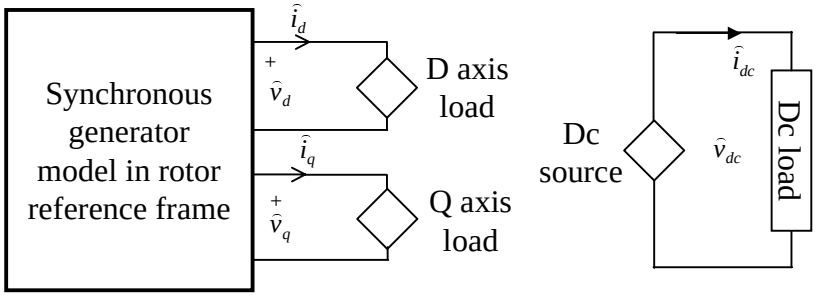

Fig. 4.2. Block diagram of the average model.

- Set 2

$$\hat{i}_{dc} = k_i\left[\hat{i}_d \sin(\delta+\phi) + \hat{i}_q \cos(\delta+\phi)\right], \tag{4.12}$$

$$\hat{v}_d = \frac{\hat{v}_{dc}}{k_v}\sin\delta, \tag{4.13}$$

$$\hat{v}_q = \frac{\hat{v}_{dc}}{k_v}\cos\delta \,, \tag{4.14}$$

$$\delta = \arctan\frac{\hat{v}_d}{\hat{v}_q} \,. \tag{4.15}$$

It can be seen that, both in Set 1 and Set 2, an equation for calculation of rotor angle δ was included among the average model's equations. More generally, if the generator's mechanical transients were modeled, angle δ should be calculated according to (2.17). In our case, rotor speed is set as a model parameter, and δ can change only due to electrical transients; therefore, it can be calculated directly from the armature voltages in the *dq* reference frame.

It can be seen that the average model's equations establish a 'transformer-like' relationship between the generator's output in the *dq* reference frame, and the rectifier's dc output. For example, if Set 1 is considered, dc output voltage is calculated from armature *d* and *q* axis voltages, and the generator's armature currents in the *dq* reference frame are calculated from the dc output current. However, the presence of angle δ in (4.9) and (4.10) causes the armature currents in the *dq* reference frame to be dependent also on the armature voltages in the *dq* reference frame. That is a consequence of the fact that the generator is not an ideal voltage source.

An analogous conclusion can be reached if Set 2 of the average model equations is considered.

Set 1 of the average model equations can be written in a somewhat different form if the equation for calculation of angle δ is incorporated into other equations. That can be done by expanding $\sin(\delta+\phi)$ and $\cos(\delta+\phi)$, and replacing $\sin\delta$ with $k_v\hat{v}_d / \hat{v}_{dc}$, and $\cos\delta$ with $k_v\hat{v}_q / \hat{v}_{dc}$. That results in:

- Set 1a

$$\hat{v}_{dc} = k_v \sqrt{\hat{v}_d^2 + \hat{v}_q^2}\,, \tag{4.16}$$

$$\hat{i}_d = (k_{\cos}\hat{v}_d + k_{\sin}\hat{v}_q)\frac{\hat{i}_{dc}}{\hat{v}_{dc}}\,, \tag{4.17}$$

$$\hat{i}_q = (k_{\cos}\hat{v}_q - k_{\sin}\hat{v}_d)\frac{\hat{i}_{dc}}{\hat{v}_{dc}}\,, \tag{4.18}$$

where

$$k_{\cos} = \frac{k_v \cos\phi}{k_i}\,, \tag{4.19}$$

$$k_{\sin} = \frac{k_v \sin\phi}{k_i}\,. \tag{4.20}$$

Mathematically, Set 1, Set 2 and Set 1a are completely equivalent to each other. However, when simulation of the average model is performed, sometimes one set of equations is more convenient than another, as far as the calculation of the steady state operating point and convergence problems are regarded. It is useful, therefore, to use them interchangeably in order to obtain the best simulation results.

4.3. Verification of the average model

In order to verify the average model, the simulation results obtained with it can be compared to the simulation results obtained with the switching model, and to measurement results. Between these two choices, comparison with the switching model results are more meaningful for verification of the average model, because they are not

influenced by possible errors in machine parameter values, which can cause discrepancies between simulation and measurement. However, as this section will show, good matching of the results was obtained in both cases.

Two types of transients were simulated and measured: the step in the exciter's field voltage and the step in the main generator's resistive dc load. The measured variables included the exciter's field current and the main generator's dc-link voltage. Measurements were performed at various generator speeds, and at reduced voltage and power levels (compared to the system's rated power), because of the limitations of measuring instruments. All average model simulations were done with values of ϕ, k_v and k_i corresponding to 50% load on Fig. 3.15, Fig. 3.16 and Fig. 3.17, that are summarized in Table 4.1.

Table 4.1. Values of k_v, k_i and ϕ used for verification of the average model.

	ϕ (rad/s)	k_v	k_i
Main generator	0.24	1.29	0.75
Exciter	0.13	1.22	0.78

Fig. 4.3 shows the main generator's field voltage (i.e. the output voltage of the exciter's diode bridge) during transient caused by stepping the exciter's field voltage from 0 to 47.5 V. The generator is rotating at maximum speed (4000 rpm), and the steady state operating point, reached after the transient is finished, corresponds to the maximum (150 kW) power output of the system. Fig. 4.4 shows the same waveform, but is obtained with the average model. It can be seen that it resembles very closely the waveform obtained with the switching model, except for the ripple. It is interesting to point out that the simulation whose results are shown in Fig. 4.3 required 207 s to be completed, while the one showed in Fig. 4.4 required 2.55 s. That makes it easy to understand how much simulation time the average model can save.

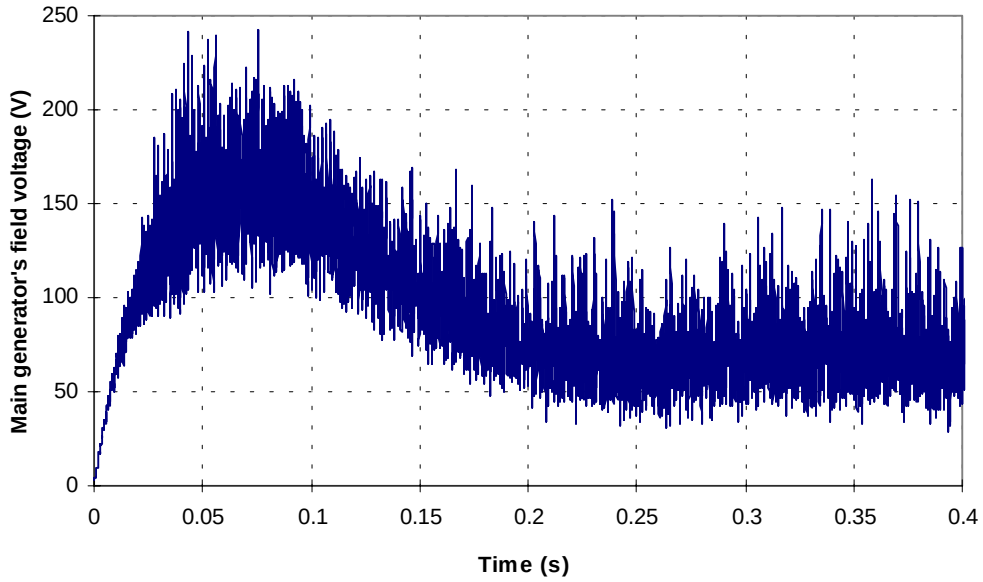

Fig. 4.3. Switching model simulation: the main generator's field voltage at the exciter's field voltage step from 0 V to 47.5 V (n=4000 rpm, R_l=4.27 Ω).

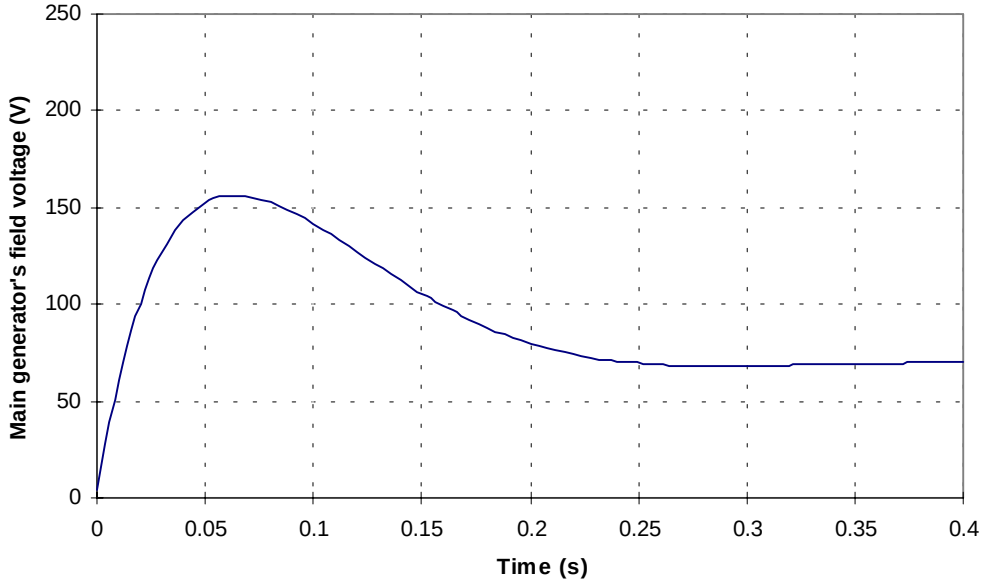

Fig. 4.4. Average model simulation: the main generator's field voltage at the exciter's field voltage step from 0 V to 47.5 V (n=4000 rpm, R_l=4.27 Ω).

Fig. 4.5 shows the measured waveforms of the exciter's field current and main dc-link voltage during transient caused by a 0 to 8.5 V step in the exciter's field voltage. The generator is rotating at 3050 rpm, and the load resistance is 18.75 Ω, which corresponds to a steady state power output of approximately 12 kW. Fig. 4.6 shows the same

waveforms obtained with the switching model simulation, and Fig. 4.7 shows average model simulation results. Even though the waveforms in Fig. 4.5, Fig. 4.6 and Fig. 4.7 are very similar, there are some differences among them that require a comment. First, the measurement shows some dc-link voltage even at zero exciter's field voltage. That is due to remnant magnetism in the real machine, which is not taken into account by the generator model. Second, when the switching model simulation was done, the exciter's field voltage needed to be lower (7 V), compared to the measured case (8.5 V), in order to achieve the same steady state dc-link voltage. That can be attributed to errors in the exciter's and main generator's parameters. Third, the value of steady state dc-link voltage obtained with the average model is slightly lower than the value obtained with the switching model. That can be attributed to the fact that, when the average model simulation was done, values of ϕ, k_v and k_i corresponding to 50% load in Fig. 3.15, Fig. 3.16 and Fig. 3.17 were chosen, even though actual output power was less than 10% of rated power. The speed, also, was not such that it would correspond to the power according to Fig. 3.14.

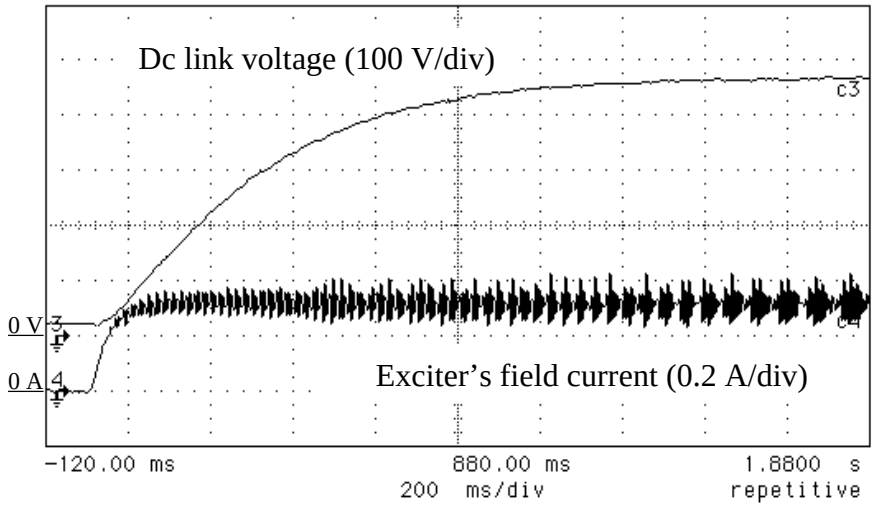

Fig. 4.5. Measurement: dc-link voltage and the exciter's field current at the exciter's field voltage step from 0 V to 8.5 V (n=3050 rpm, R_l=18.75 Ω).

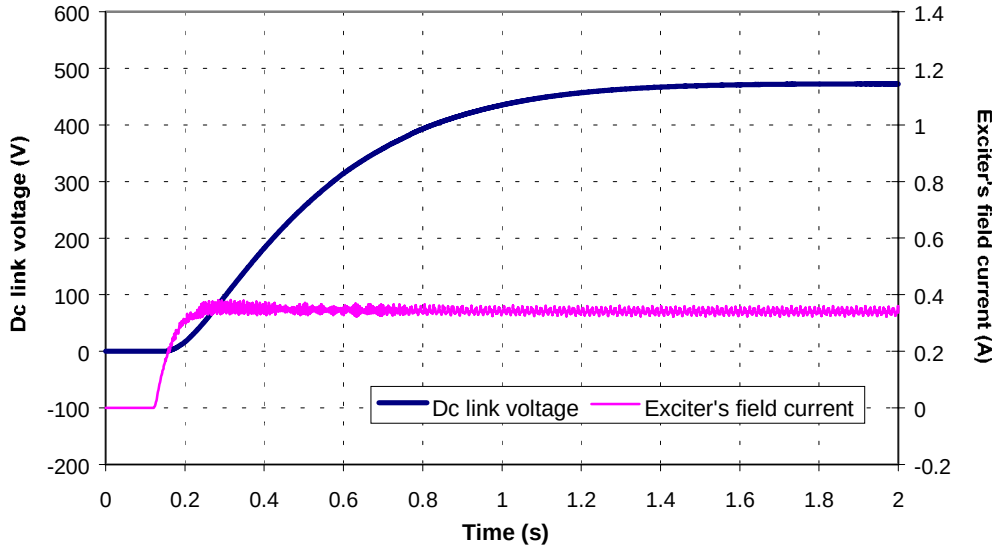

Fig. 4.6. Switching model simulation: dc-link voltage and the exciter's field current at the exciter's field voltage step from 0 V to 7 V (n=3050 rpm, R_l=18.75 Ω).

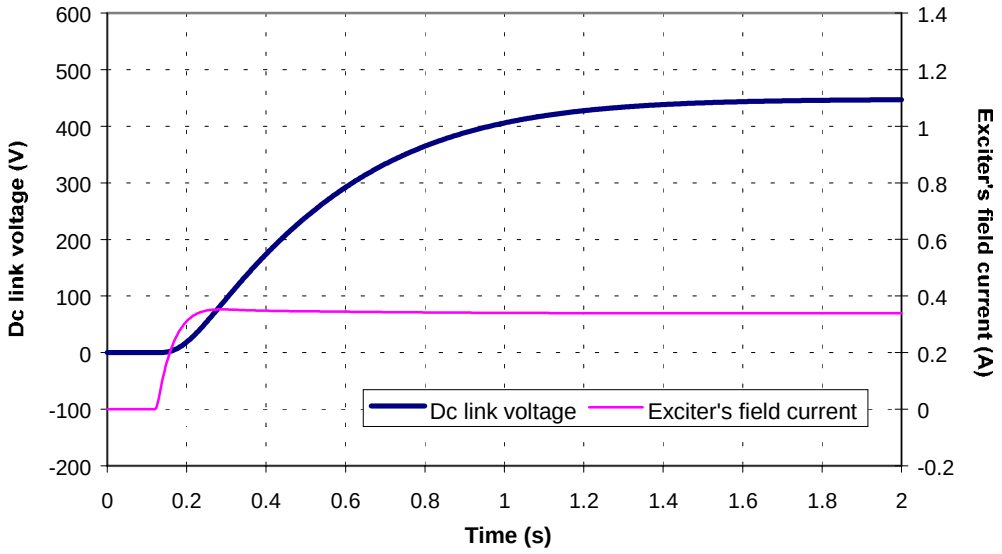

Fig. 4.7. Average model simulation: dc-link voltage and the exciter's field current at the exciter's field voltage step from 0 V to 7 V (n=3050 rpm, R_l=18.75 Ω).

Measured and simulated waveforms during transient caused by interruption of the exciter field current are shown in Fig. 4.8, Fig. 4.9 and Fig. 4.10. Regarding the small differences in waveforms, the same comments can be applied as in the previous case.

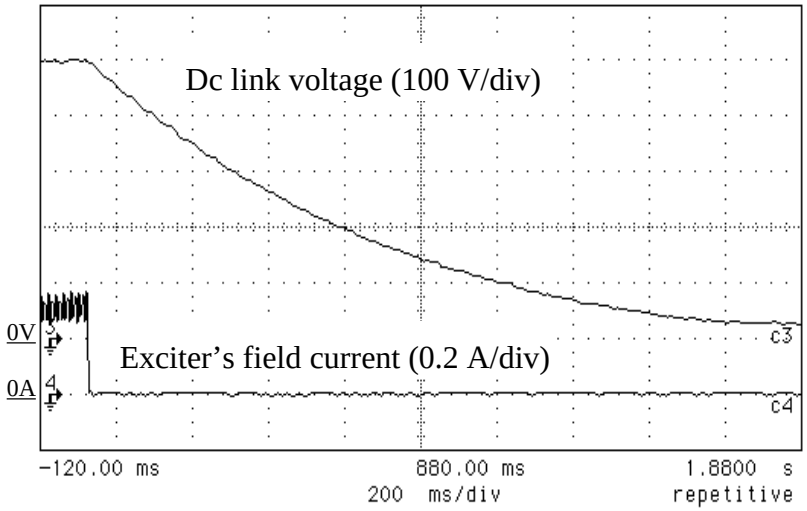

Fig. 4.8. Measurement: dc-link voltage and the exciter's field current at the exciter's field current step from 0.34 A to 0 A (n=3050 rpm, R_l=18.75 Ω.).

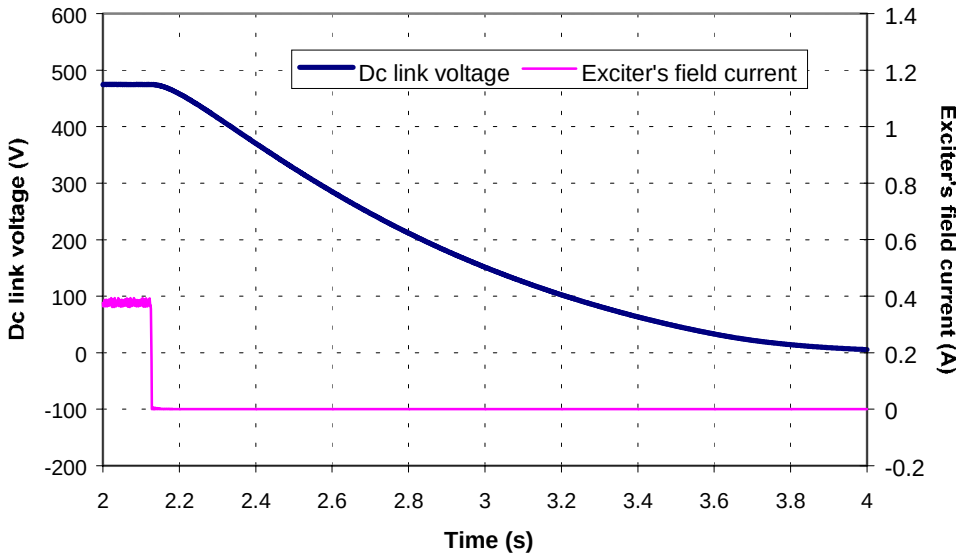

Fig. 4.9. Switching model simulation: dc-link voltage and the exciter's field current at the exciter's field current step from 0.38 A to 0 A (n=3050 rpm, R_l=18.75 Ω).

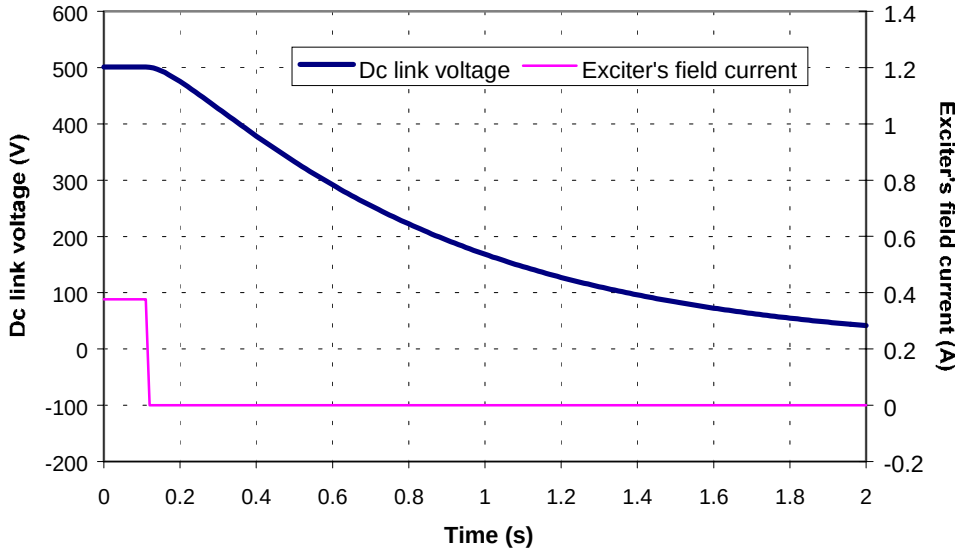

Fig. 4.10. Average model simulation: dc-link voltage and the exciter's field current at the exciter's field current step from 0.38 A to 0 A (n=3050 rpm, R_l=18.75 Ω).

The transient caused by stepping the main generator's resistive dc load is shown in Fig. 4.11, Fig. 4.12 and Fig. 4.13 (measurement, switching model simulation and average model simulation, respectively). A slight undershoot, not registered during the measurement, can be noticed in the simulated waveform of the dc-link voltage; it can be attributed to errors in machine parameters. Also, for the same reason as before, the steady state dc-link voltage is somewhat larger when obtained with the average model than with the switching model.

It is also interesting to notice the effect of the large generator's synchronous reactance on Fig. 4.11: when load resistance drops by a factor of two, the output voltage drops by a large amount (approximately a factor of two in this case). The same effect can be observed in Fig. 4.14 and Fig. 4.15, which show dc-link voltage during the transient due to the disconnection of 19 Ω (2 kW) resistive dc load, at two different speeds (2000 rpm and 3700 rpm). It can be seen how the difference in dc-link voltage before and after the transient depends on generator speed (i.e. the generator's synchronous reactance).

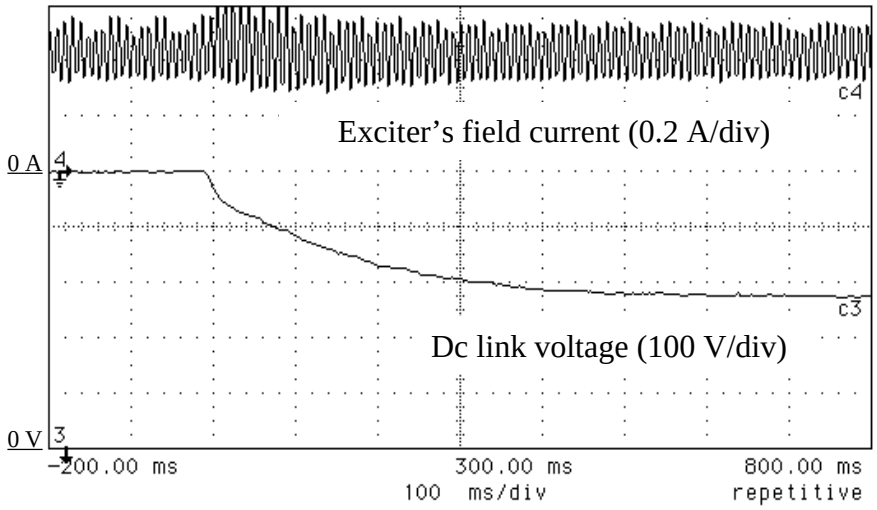

Fig. 4.11. Measurement: dc-link voltage and the exciter's field current at resistive load step from 12.5 Ω to 6.25 Ω (n=3100 rpm, v_{fd}=11.6 V).

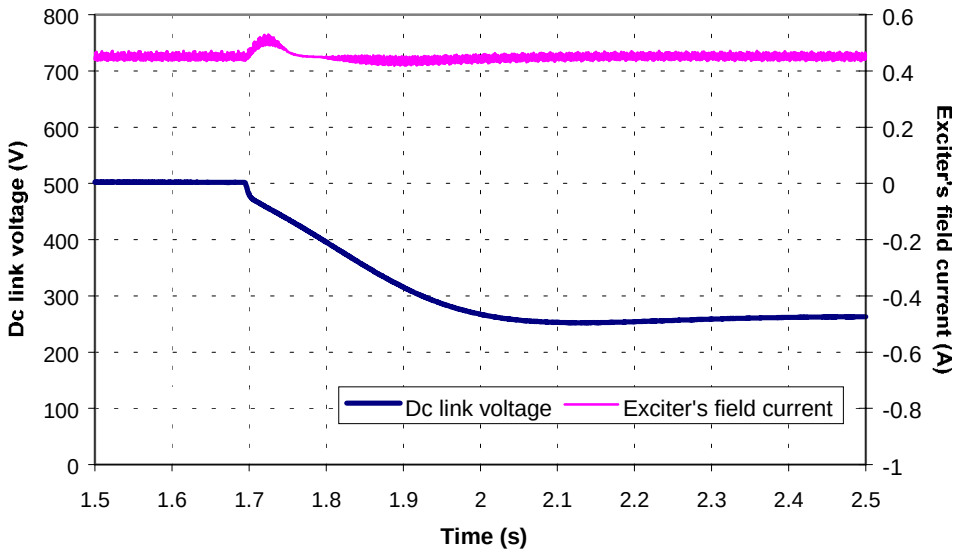

Fig. 4.12. Switching model simulation: dc-link voltage and the exciter's field current at resistive load step from 12.5 Ω to 6.25 Ω (n=3100 rpm, v_{fd}=11.6 V).

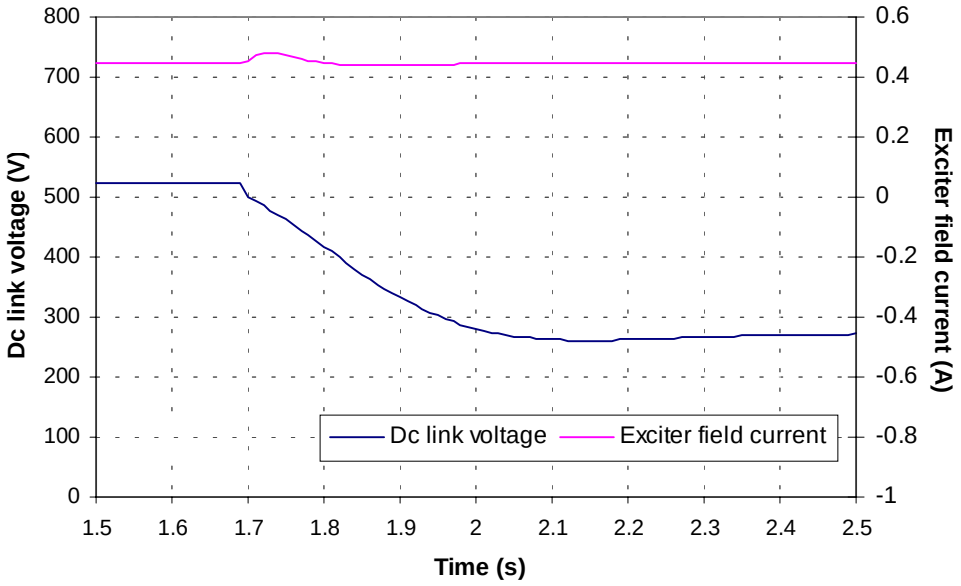

Fig. 4.13. Average model simulation: dc-link voltage and the exciter's field current at resistive load step from 12.5 Ω to 6.25 Ω (n=3100 rpm, v_{fd}=11.6 V).

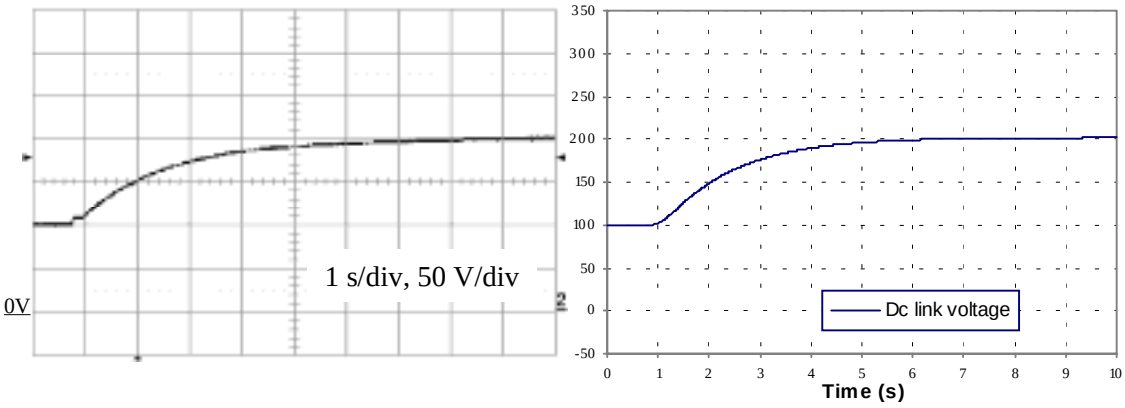

(a) (b)

Fig. 4.14. (a) measurement, (b) average model simulation: dc-link voltage in transient following disconnection of 19 Ω resistive dc load (n=2000 rpm, v_{fd}=3.4 V in (a), v_{fd}=1.85 V in (b)).

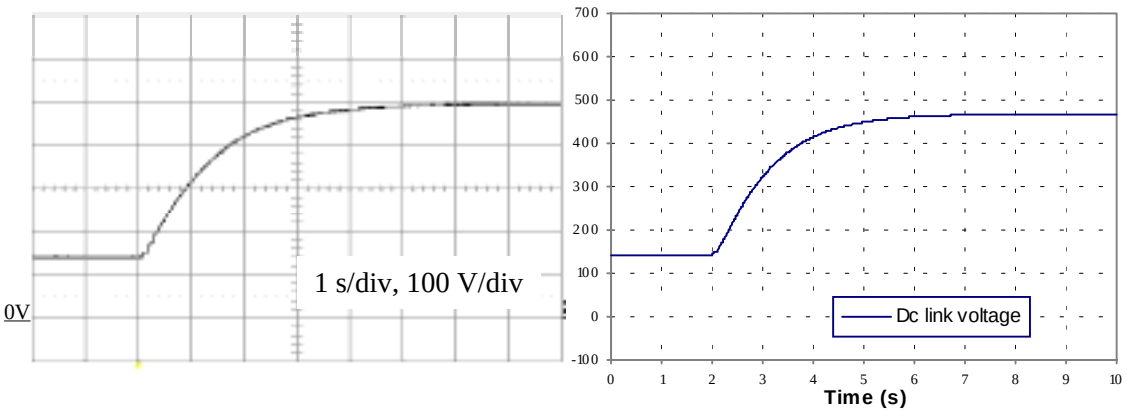

(a) (b)

Fig. 4.15. (a) measurement, (b) average model simulation: dc-link voltage in transient following disconnection of 19 Ω resistive dc load (n=3700 rpm, v_{fd}=2.8 V in (a), v_{fd}=2.03 V in (b)).

The results presented in this section lead to the following conclusions:

1. Transient waveforms obtained with average model match extremely well, in the moving average sense, transient waveforms obtained with the switching model. Slight discrepancies (about 5%) in steady state values can be attributed to the fact that the same values of ϕ, k_v and k_I, relative to 50% load in Fig. 3.15, Fig. 3.16 and Fig. 3.17, were used for all average model simulation, regardless of the operating point. Differences in dynamic waveforms characteristics (overshoot, undershoot, settling time) are practically invisible between the switching and average model results.

2. All simulation results (switching and average model) match reasonably well with measurement results. The differences can be explained by either the generator model's inherent drawbacks (absence of modeling of magnetic saturation and remnant magnetism), or by errors in the main generator's and exciter's parameters.

3. Based on the above conclusions, the average model presented in Section 4.2.2 can be used in order to predict dynamic behavior of the system shown in Fig. 3.2. Validity of the model will be discussed more generally in the following section.

4.4. Validity of the average model

4.4.1. Discussion of first harmonic assumption

Based on the discussion regarding the importance of higher harmonics for operation of a diode bridge loaded synchronous generator (Section 3.3), the following conditions must be satisfied so that the average model represents the actual system's behavior with sufficient accuracy:

1. The generator's harmonics other than fundamental deliver negligible active power;
2. The diode rectifier output is well filtered (large L, or C, or both).

In most practical applications, both of these conditions will be true. Almost any synchronous machine (or, more generally, any non-ideal electrical source) will have the reactive part of its internal impedance dominant when compared to the resistive part. That will cause the active power associated with higher harmonics at the rectifier's input to be negligible. Similarly, there is always some kind of filter at the output of the diode bridge. Because of that, either dc voltage or dc current at the rectifier's output will have a negligible ripple.

Therefore, it can be expected that the above requirements will not limit the possibility of practical applications of the developed average model.

4.4.2. Average model and diode rectifier losses

It was explained in Section 3.3 how the diode's forward voltage drop influences calculation of the exciter's k_v at light load. It is the purpose of this section to discuss, in a

somewhat more detailed manner, how diode rectifier losses can be related to parameters of the average model.

It needs to be made clear, at the very beginning of this discussion, that all switching model simulation results presented in previous sections of this work were obtained with the default diode model available in PSpice. That model accounts for forward voltage drop, i.e. diodes used in switching model simulations were characterized by a forward voltage drop larger than zero. However, no attempts were made to accurately model real diodes used in the actual generator set that is the object of this study. Therefore, all results regarding relationships between diode losses and average model parameters need to be interpreted from only the conceptual point of view, without attributing to them any practical meaning relative to the actual studied system.

The average model's parameters (ϕ, k_v and k_i) were obtained based on switching model simulations. Therefore, the average model contains information about diode forward voltage drop and losses. That can be quantified if the diode rectifier input power is expressed as

$$\hat{p}_{in} = \hat{v}_d \hat{i}_d + \hat{v}_q \hat{i}_q \,. \tag{4.21}$$

When d and q axis voltages are substituted according to (4.13) and (4.14), and currents according to (4.9) and (4.10), input power can be written as

$$\hat{p}_{in} = \frac{\cos\phi}{k_v k_i} \hat{v}_{dc} \hat{i}_{dc} \,. \tag{4.22}$$

The product of dc voltage and current in (4.22) can be recognized as output power of the diode rectifier

$$\hat{p}_{out} = \hat{v}_{dc} \hat{i}_{dc} \,. \tag{4.23}$$

Therefore, efficiency of the diode rectifier can be expressed as

$$\eta = \frac{\hat{p}_{out}}{\hat{p}_{in}} = \frac{k_v k_i}{\cos\phi}\,. \tag{4.24}$$

This last expression relates efficiency of the diode rectifier directly to the parameters of the generator/rectifier average model. Fig. 4.16 shows variation of the exciter's and the main generator's rectifier efficiency with load, when speed versus load relationship is the one shown in Fig. 3.14. The main generator's rectified output dc voltage is kept at 800 V at any operating point, which makes the main generator's diode rectifier's output power proportional to the output current. At the same time, diode losses are approximately proportional to the diode current. Consequently, the main generator's rectifier efficiency does not change with load variations.

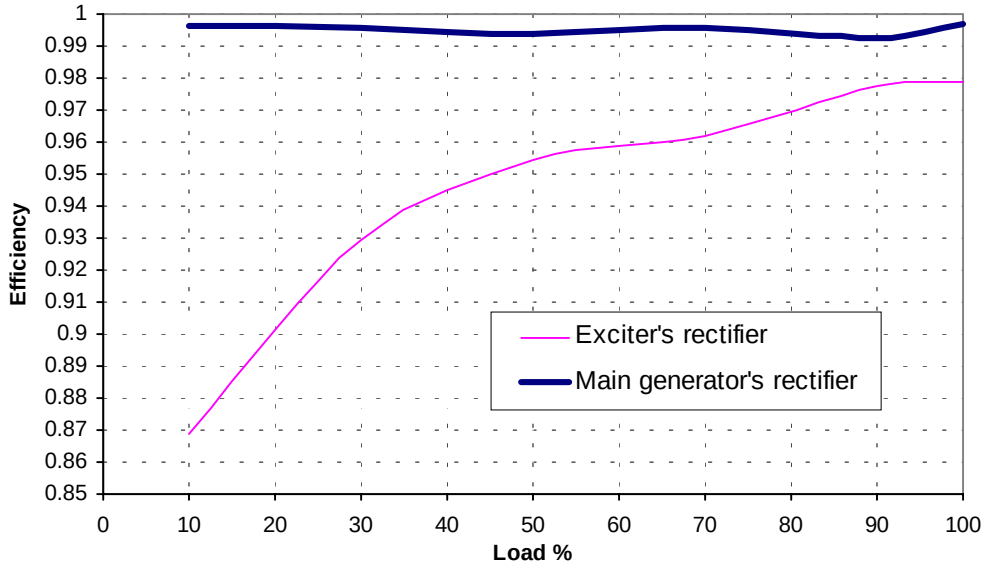

Fig. 4.16. Diode rectifier's efficiency variation with load.

The exciter's case is different. The exciter's rectifier needs to provide variable dc voltage for the main generator's field winding. At low output power, this voltage is low enough to decrease significantly the exciter's diode rectifier's efficiency.

Fig. 4.16 also allows for discussion, from a power balance point of view, the legitimacy of the use of ϕ, k_v and k_i values relative to 50% load for any operating point. (They were used in Section 4.3, when the average model was verified through comparison with switching model simulation and measurements.) It can be seen that, for

the main generator, rectifier efficiency at 50% load is practically equal to efficiency at any other load; therefore, use of ϕ, k_v and k_i relative to 50% load does not introduce any error, as far as power balance is concerned. For the exciter, however, efficiency at 50% load is considerably different from efficiency at a lower or higher load. However, power processed by the exciter is very small compared to the power processed by the main generator. Consequently, it can be said that error introduced by the use of 'wrong' values of exciter's ϕ, k_v and k_i does not affect significantly the power balance of the whole system.

The ideal case, (lossless diodes and no reactive components on either side of diode rectifier) is characterized by η=1, ϕ=0, $k_v = 3\sqrt{2}/\pi$, $k_i = \pi/(3\sqrt{2})$, i.e.

$$k_i = \frac{1}{k_v},$$

(4.25)

which recalls the relationship characterizing an ideal transformer.

If the diode rectifier is lossless (η=1), but reactive components are present at both sides of diode rectifier (ϕ>0), (4.24) yields

$$k_v k_i = \cos\phi .$$

(4.26)

In this case, product $k_v k_i$ can be interpreted as describing the reactive nature of source and load impedances. When losses in the diode rectifier are negligible ($\eta \approx 1$), such as in the main generator's case, expression (4.26) can be considered alternative to (3.1) for calculation of ϕ, once k_v and k_i are calculated.

The real case (η<1, ϕ>0) is described by

$$k_v k_i = \frac{\cos\phi}{\eta},$$

(4.27)

which means that product $k_v k_i$ reflects both the reactive nature of source and load impedances, and losses in the system.

4.4.3. Use of the average model with different loads and sources

The average model's equations were developed based on the switching model results obtained with resistive load at the main generator's dc-link. Consequently, the validity of the average model can be questioned if a different dc load (e.g., an inverter) is applied, as in the practical system shown in Fig. 1.1. In order to justify the use of the average model with such a dc load, it needs to be remembered that the average model's parameters (ϕ, k_v and k_i) were obtained from the switching model steady state waveforms. If the dc-link capacitor is large enough to provide the high-frequency current component required by the inverter, there is no reason why the generator's voltage and current steady state waveforms should be different with the inverter dc load, as opposed to the resistive dc load. Essentially, the main generator still has a dc voltage source connected to its rectifier's output, and the average model can still be considered valid.

The above justification of the use of the average model does not mean, however, that the actual inverter can be approximated by a resistor. An inverter operating in closed loop is a constant power load in the sense that, if the dc-link voltage rises for any reason, the closed loop inverter will decrease its duty cycle, which will result in smaller current being drawn from the dc-link. That, small-signal-wise, can be represented by a negative resistor [22] or, less accurately but easier to apply to control design, a current source. A dc current source connected to the dc-link provides the desired steady state operating point, but does not introduce any damping at the output (damping does not exist with the actual closed-loop inverter, but it would be introduced if the inverter were represented by a resistor). Therefore, it can be expected that it will be more difficult to stabilize the closed loop system with current source load than with resistive load.

The average model was developed for the case in which an independent synchronous generator feeds a diode rectifier. However, it can be generalized to any case in which a diode rectifier is fed by a three-phase voltage source with complex source impedance; it suffices to write equations of the particular voltage source of interest, and transform them to the *dq* reference frame. The average model is then directly applicable.

The model's strength, however, consists in taking into account the effects of the non-ideal operation of the diode rectifier. Therefore, the use of the model is meaningful primarily in cases in which the source's impedance causes the rectifier's strongly non-ideal operation.

4.5. Linearized average model

4.5.1. Linearization of model equations

The average model's equations, presented in Section 4.2.2, are non-linear because they contain products of variables, as well as trigonometric functions. For some purposes, such as control-loop design, it is necessary to study the linearized system. In many cases, software used for simulation of the average model is capable of linearizing system equations, after it determines the steady-state operating point. However, it is useful to find analytically the linearized version of average model equations. That makes it possible to easily simulate cases that would cause numerical problems in determining the steady state operating point, as well as to find the linearized state space representation of the system.

In this section, linearized versions of (4.8)-(4.11) (Set 1) and (4.16)-(4.18) (Set 1a) of average model equations will be presented. Linearizing an equation around a certain steady state operating point is equivalent to finding Taylor's expansion of the function represented by that equation, and neglecting all terms other than the constant and the linear term. The obtained linear expression is valid only for small perturbations around the selected operating point.

In this and the following sections, the steady state value of an average variable $\hat{x}$ will be denoted as X, while $\tilde{x}$ will stand for small perturbation of the same variable. With these conventions, the following linearized version of (4.8)-(4.11) can be obtained:

$$\tilde{v}_{dc} = k_1\tilde{v}_d + k_2\tilde{v}_q + k_3\tilde{\delta}\ , \tag{4.28}$$

$$\tilde{i}_d = k_4\tilde{i}_{dc} + k_5\tilde{\delta}\ , \tag{4.29}$$

$$\tilde{i}_q = k_6\tilde{i}_{dc} + k_7\tilde{\delta}\ , \tag{4.30}$$

$$\tilde{\delta} = k_8\tilde{v}_d + k_9\tilde{v}_q\ , \tag{4.31}$$

where

$$k_1 = k_v\, sin\Delta\ , \tag{4.32}$$

$$k_2 = k_v\, cos\Delta\ , \tag{4.33}$$

$$k_3 = k_v(V_d\cos\Delta - V_q\sin\Delta)\ , \tag{4.34}$$

$$k_4 = \frac{sin(\Delta+\varphi)}{k_i}\ , \tag{4.35}$$

$$k_5 = \frac{I_{dc}\, cos(\Delta+\varphi)}{k_i}\ , \tag{4.36}$$

$$k_6 = \frac{cos(\Delta+\varphi)}{k_i}\ , \tag{4.37}$$

$$k_7 = -\frac{I_{dc}\, sin(\Delta+\varphi)}{k_i}\ , \tag{4.38}$$

$$k_8 = \frac{\cos\Delta}{V_q \cos\Delta + V_d \sin\Delta},$$

(4.39)

$$k_9 = -\frac{\sin\Delta}{V_q \cos\Delta + V_d \sin\Delta}.$$

(4.40)

Linearization of (4.16)-(4.18) yields

$$\tilde{v}_{dc} = c_1\tilde{v}_d + c_2\tilde{v}_q,$$

(4.41)

$$\tilde{i}_d = c_3\tilde{i}_{dc} + c_4\tilde{v}_{dc} + c_5\tilde{v}_d + c_6\tilde{v}_q,$$

(4.42)

$$\tilde{i}_q = c_7\tilde{i}_{dc} + c_8\tilde{v}_{dc} + c_9\tilde{v}_d + c_{10}\tilde{v}_q,$$

(4.43)

where

$$c_1 = \frac{k_v V_d}{\sqrt{V_d^2 + V_q^2}},$$

(4.44)

$$c_2 = \frac{k_v V_q}{\sqrt{V_d^2 + V_q^2}},$$

(4.45)

$$c_3 = \frac{k_{\cos} V_d + k_{\sin} V_q}{V_{dc}},$$

(4.46)

$$c_4 = -\frac{I_d}{V_{dc}},$$

(4.47)

$$c_5 = \frac{k_{\cos} I_{dc}}{V_{dc}},$$

(4.48)

$$c_6 = \frac{k_{\sin} I_{dc}}{V_{dc}},$$

(4.49)

$$c_7 = \frac{k_{\cos} V_q - k_{\sin} V_d}{V_{dc}},$$

(4.50)

$$c_8 = -\frac{I_q}{V_{dc}},$$

(4.51)

$$c_9 = -\frac{k_{\sin} I_{dc}}{V_{dc}},$$

(4.52)

$$c_{10} = \frac{k_{\cos} I_{dc}}{V_{dc}},$$

(4.53)

4.5.2. Linearized state-space representation

The purpose of this section is to find a linear state space representation of the system consisting of the exciter, main generator and a dc load. This is obtained by combining the machine's equations (2.6)-(2.12) with the linearized generator/rectifier average model's equations, and an equation describing the dc load. This is an algebraically tedious process that does not introduce any new concepts. Some readers, therefore, may wish not to pay particular attention to sections 4.5.2.1 and 4.5.2.2, in which algebraic manipulations are carried out, but to use results given in section 4.5.2.3.

If the generator's speed is constant and treated as a parameter of the system, (2.6)-(2.12) are linear differential equations, and they can be rewritten for small perturbations by simply adding a tilde to all currents and voltages. Since both the exciter's and the main generator's equations will be treated in this section, index 'e' will be added to all parameters and variables relative to the exciter, and index 'a' to all those relative to the main generator, in order to be able to distinguish between them. For example, R_{as} will stand for the armature resistance of the main generator, i_{ed} will stand for exciter's *d* axis armature current, and so on.

4.5.2.1. Exciter's equations

With the above conventions, the exciter's equations can be written as

$$\tilde{v}_{ed} = -R_{es}\tilde{i}_{ed} + \omega_e(L_{els} + L_{emq})\tilde{i}_{eq} - (L_{els} + L_{emd})\frac{d\tilde{i}_{ed}}{dt} + L_{emd}\frac{d\tilde{i}_{efd}}{dt}, \tag{4.54}$$

$$\tilde{v}_{eq} = -R_{es}\tilde{i}_{eq} - \omega_e(L_{els} + L_{emd})\tilde{i}_{ed} + \omega_e L_{emd}\tilde{i}_{efd} - (L_{els} + L_{emq})\frac{d\tilde{i}_{eq}}{dt}, \tag{4.55}$$

$$\tilde{v}_{efd} = R_{efd}\tilde{i}_{efd} - L_{emd}\frac{d\tilde{i}_{ed}}{dt} + (L_{elfd} + L_{emd})\frac{d\tilde{i}_{efd}}{dt}. \tag{4.56}$$

These equations obviously suggest use of the exciter's currents for state variables. In equation (4.56), $\tilde{v}_{efd}$ is considered to be the input to the system, which means that (4.56) is already in a form suitable for obtaining linear state space representation. What remains to be done is to express $\tilde{v}_{ed}$ and $\tilde{v}_{eq}$ as linear functions of currents and their derivatives, and to substitute the found expressions in (4.54) and (4.55). That can be achieved by combining linearized equations of the generator/rectifier average model

(4.28)-(4.31) with the exciter's dc load equation. By substituting (4.31) into (4.28), (4.29) and (4.30), we get

$$\tilde{v}_{edc} = k_{138}\tilde{v}_{ed} + k_{239}\tilde{v}_{eq}\,, \tag{4.57}$$

$$\tilde{i}_{ed} = k_4\tilde{i}_{edc} + k_5k_8\tilde{v}_{ed} + k_5k_9\tilde{v}_{eq}\,, \tag{4.58}$$

$$\tilde{i}_{eq} = k_6\tilde{i}_{edc} + k_7k_8\tilde{v}_{ed} + k_7k_9\tilde{v}_{eq}\,, \tag{4.59}$$

where

$$k_{138} = k_1 + k_3k_8\,, \tag{4.60}$$

$$k_{239} = k_2 + k_3k_9\,. \tag{4.61}$$

The exciter's dc load is represented by the main generator's field winding, whose equation is

$$\tilde{v}_{afd} = R_{afd}\tilde{i}_{afd} - L_{amd}\frac{d\tilde{i}_{ad}}{dt} + (L_{alfd} + L_{amd})\frac{d\tilde{i}_{afd}}{dt} + L_{amd}\frac{d\tilde{i}_{akd}}{dt}\,. \tag{4.62}$$

The main generator's field voltage in (4.62) is referred to the armature, but it is related to the exciter's rectified output voltage by means of the main generator's field-to-armature turns ratio t_a as

$$\tilde{v}_{afd} = t_a\tilde{v}_{edc}\,. \tag{4.63}$$

Similarly, for currents

$$\tilde{i}_{afd} = \frac{1}{t_a}\tilde{i}_{edc}\,. \tag{4.64}$$

When (4.62), (4.63) and (4.64) are combined, the following exciter's load equation is obtained:

$$\tilde{v}_{edc} = \frac{R_{afd}}{t_a^{\,2}}\tilde{i}_{edc} - \frac{L_{amd}}{t_a}\frac{d\tilde{i}_{ad}}{dt} + \frac{L_{alfd}+L_{amd}}{t_a^{\,2}}\frac{d\tilde{i}_{edc}}{dt} + \frac{L_{amd}}{t_a}\frac{d\tilde{i}_{akd}}{dt}. \tag{4.65}$$

It can be seen that (4.65) contains main generator's *d* axis currents; that accounts for dynamic coupling between the exciter and the main generator.

Now it is possible to find expressions for $\tilde{v}_{ed}$ and $\tilde{v}_{eq}$ by eliminating $\tilde{v}_{edc}$ and $\tilde{i}_{edc}$ from the system of equations consisting of (4.57)-(4.59) and (4.65). That yields

$$\tilde{v}_{ed} = r_{edd}\tilde{i}_{ed} + l_{edd}\frac{d\tilde{i}_{ed}}{dt} + r_{edq}\tilde{i}_{eq} + l_{edq}\frac{d\tilde{i}_{eq}}{dt} - k_9 l_{ae}\frac{d\tilde{i}_{ad}}{dt} + k_9 l_{ae}\frac{d\tilde{i}_{akd}}{dt}, \tag{4.66}$$

$$\tilde{v}_{eq} = r_{eqd}\tilde{i}_{ed} + l_{eqd}\frac{d\tilde{i}_{ed}}{dt} + r_{eqq}\tilde{i}_{eq} + l_{eqq}\frac{d\tilde{i}_{eq}}{dt} + k_8 l_{ae}\frac{d\tilde{i}_{ad}}{dt} - k_8 l_{ae}\frac{d\tilde{i}_{akd}}{dt}, \tag{4.67}$$

where

$$k_{\det} = k_4 k_7 (k_9 k_{138} - k_8 k_{239}) + k_5 k_6 (k_8 k_{239} - k_9 k_{138}) \tag{4.68}$$

$$r_{edd} = \frac{k_6 k_{239} + k_7 k_9 \dfrac{R_{afd}}{t_a^{\,2}}}{k_{\det}}, \tag{4.69}$$

$$r_{edq} = -\frac{k_4 k_{239} + k_5 k_9 \dfrac{R_{afd}}{t_a^{\,2}}}{k_{\det}}, \tag{4.70}$$

$$l_{edd} = \frac{k_7 k_9 (L_{alfd} + L_{amd})}{t_a^{\,2} k_{\det}}, \tag{4.71}$$

$$l_{edq} = -\frac{k_5 k_9 (L_{alfd} + L_{amd})}{t_a{}^2 k_{\det}},$$

(4.72)

$$r_{eqd} = -\frac{k_6 k_{138} + k_7 k_8 \frac{R_{afd}}{t_a{}^2}}{k_{\det}},$$

(4.73)

$$r_{eqq} = -\frac{k_4 k_{138} + k_5 k_8 \frac{R_{afd}}{t_a{}^2}}{k_{\det}},$$

(4.74)

$$l_{eqd} = -\frac{k_7 k_8 (L_{alfd} + L_{amd})}{t_a{}^2 k_{\det}},$$

(4.75)

$$l_{eqq} = \frac{k_5 k_8 (L_{alfd} + L_{amd})}{t_a{}^2 k_{\det}},$$

(4.76)

$$l_{ae} = \frac{k_4 k_7 - k_5 k_6}{t_a k_{\det}} L_{amd},$$

(4.77)

The same process allows us to find the following expression for the main generator's field current:

$$\tilde{i}_{afd} = h_{aed} \tilde{i}_{ed} + h_{aeq} \tilde{i}_{eq},$$

(4.78)

where

$$h_{aed} = \frac{k_{138} k_7 k_9 - k_{239} k_7 k_8}{t_a k_{\det}},$$

(4.79)

$$h_{aeq} = \frac{k_{239}k_5k_8 - k_{138}k_5k_9}{t_a k_{\det}}.$$

(4.80)

Expressions (4.66) and (4.67) will be substituted into (4.54) and (4.55), respectively, in order to obtain linear state space representation. Expression (4.78) allows us to replace the main generator's field current by a linear combination of the exciter's armature currents; that eliminates the main generator's field current as a state variable, and reduces the order of the system by one.

4.5.2.2. Main generator's equations

It is possible to proceed now with rewriting the main generator's equations for small perturbations. In doing so, the field winding equation is omitted, since it has already been used as the exciter's load equation, and the main generator's field current is substituted according to (4.78). That yields

$$v_{ad} = -R_{as}i_{ad} + \omega_a(L_{als} + L_{amq})i_{aq} - \omega_a L_{amq}i_{akq} - (L_{als} + L_{amd})\frac{di_{ad}}{dt} + \\ + L_{amd}\frac{d(h_{aed}i_{ed} + h_{aeq}i_{eq})}{dt} + L_{amd}\frac{di_{akd}}{dt},$$

(4.81)

$$v_{aq} = -R_{as}i_{aq} - \omega_a(L_{als} + L_{amd})i_{ad} + \omega_a L_{amd}(h_{aed}i_{ed} + h_{aeq}i_{eq}) + \\ + \omega_a L_{amd}i_{akd} - (L_{als} + L_{amq})\frac{di_{aq}}{dt} + L_{amq}\frac{di_{akq}}{dt},$$

(4.82)

$$0 = R_{akd}i_{akd} - L_{amd}\frac{di_{ad}}{dt} + L_{amd}\frac{d(h_{aed}i_{ed} + h_{aeq}i_{eq})}{dt} + (L_{alkd} + L_{amd})\frac{di_{akd}}{dt},$$

(4.83)

$$0 = R_{akq} i_{akq} - L_{amq} \frac{di_{aq}}{dt} + (L_{alkq} + L_{amq}) \frac{di_{akq}}{dt}.$$

(4.84)

It can be seen that (4.83) and (4.84) are already in a convenient form for state space representation. As in the exciter's case, it is necessary to find expressions which will linearly relate $\tilde{v}_{ad}$ and $\tilde{v}_{aq}$ to state variables and their derivatives. Again, that can be done by combining linearized equations of generator/rectifier average model (this time, (4.41)-(4.43) will be used) with the main generator's load equation.

It can be assumed at this point, and in accordance with the discussion in Section 4.4.3, that the main generator's load is represented by a current source $\tilde{i}_{load}$. In that case, the main generator's load equation is given by

$$\tilde{i}_{adc} = C \frac{d\tilde{v}_{adc}}{dt} + \tilde{i}_{load}.$$

(4.85)

If the above expression is used to eliminate $\tilde{i}_{adc}$ from (4.42) and (4.43), the following expressions are obtained for $\tilde{v}_{ad}$ and $\tilde{v}_{aq}$:

$$\tilde{v}_{ad} = r_{add} \tilde{i}_{ad} + r_{adq} \tilde{i}_{aq} + h_{addc} \tilde{v}_{adc} + c_{addc} \frac{d\tilde{v}_{adc}}{dt} + r_{adl} \tilde{i}_{load},$$

(4.86)

$$\tilde{v}_{aq} = r_{aqd} \tilde{i}_{ad} + r_{aqq} \tilde{i}_{aq} + h_{aqdc} \tilde{v}_{adc} + c_{aqdc} \frac{d\tilde{v}_{adc}}{dt} + r_{aql} \tilde{i}_{load},$$

(4.87)

where

$$c_{\det} = \frac{1}{c_5 c_{10} - c_6 c_9},$$

(4.88)

$$r_{add} = c_{\det} c_{10},$$

(4.89)

$$r_{adq} = -c_{\det} c_6 \,, \tag{4.90}$$

$$h_{addc} = c_{\det}(c_6 c_8 - c_4 c_{10}) \,, \tag{4.91}$$

$$c_{addc} = c_{\det}(c_6 c_7 - c_3 c_{10})C \,, \tag{4.92}$$

$$r_{adl} = c_{\det}(c_6 c_7 - c_3 c_{10}) \,, \tag{4.93}$$

$$r_{aqd} = -c_{\det} c_9 \,, \tag{4.94}$$

$$r_{aqq} = c_{\det} c_5 \,, \tag{4.95}$$

$$h_{aqdc} = c_{\det}(c_4 c_9 - c_5 c_8) \,, \tag{4.96}$$

$$c_{aqdc} = c_{\det}(c_3 c_9 - c_5 c_7)C \,, \tag{4.97}$$

$$r_{aql} = c_{\det}(c_3 c_9 - c_5 c_7) \,. \tag{4.98}$$

In (4.86) and (4.87), $\tilde{i}_{load}$ needs to be treated as input to the system. These expressions will be used to substitute for armature voltages in (4.81) and (4.82), respectively.

4.5.2.3. State-space representation of the system

State-space representation of the system needs to have the following form:

$$\dot{\mathbf{x}} = \mathbf{A}\mathbf{x} + \mathbf{B}\mathbf{u}\,, \tag{4.99}$$

where

$$\mathbf{x} = \begin{bmatrix} \tilde{i}_{ed} \\ \tilde{i}_{eq} \\ \tilde{i}_{efd} \\ \tilde{i}_{ad} \\ \tilde{i}_{aq} \\ \tilde{i}_{akd} \\ \tilde{i}_{akq} \\ \tilde{v}_{adc} \end{bmatrix} \tag{4.100}$$

is the vector of state variables, and

$$\mathbf{u} = \begin{bmatrix} \tilde{v}_{efd} \\ \tilde{i}_{load} \end{bmatrix} \tag{4.101}$$

is the vector of system's inputs.

In order to find matrices **A** and **B** from (4.99), the system's equations will be written in the form

$$\mathbf{E}\dot{\mathbf{x}} = \mathbf{F}\mathbf{x} + \mathbf{G}\mathbf{u}\,. \tag{4.102}$$

After that, matrices **A** and **B** can be calculated as

$$\mathbf{A} = \mathbf{E}^{-1}\mathbf{F}\,, \tag{4.103}$$

$$\mathbf{B} = \mathbf{E}^{-1}\mathbf{G}\,. \tag{4.104}$$

In order to obtain the form given by (4.102), for each state variable, an equation is written in the following way:

- For the exciter's armature *d* axis current, by combining (4.54) and (4.66);
- For the exciter's armature *q* axis current, by combining (4.55) and (4.67);
- For the exciter's field current, by using (4.56);
- For the main generator's armature *d* axis current, by combining (4.81) and (4.86);
- For the main generator's armature *q* axis current, by combining (4.82) and (4.87);
- For the main generator's *d* axis damper winding current, by using (4.83);
- For the main generator's *q* axis damper winding current, by using (4.84);
- For dc-link voltage, by combining (4.41) with (4.86) and (4.87).

When these eight equations are written in matrix form, the following matrices **E, F** and **G** are gotten:

$$\mathbf{E}=\begin{bmatrix} -(L_{els}+L_{emd}+l_{edd}) & -l_{edq} & L_{emd} & k_9 l_{ae} & 0 & -k_9 l_{ae} & 0 & 0 \\ -l_{eqd} & -(L_{els}+L_{emq}+l_{eqq}) & 0 & -k_8 l_{ae} & 0 & k_8 l_{ae} & 0 & 0 \\ -L_{emd} & 0 & L_{elfd}+L_{emd} & 0 & 0 & 0 & 0 & 0 \\ L_{amd}h_{aed} & L_{amd}h_{aeq} & 0 & -(L_{als}+L_{amd}) & 0 & L_{amd} & 0 & -c_{addc} \\ 0 & 0 & 0 & 0 & -(L_{als}+L_{amq}) & 0 & L_{amq} & -c_{aqdc} \\ L_{amd}h_{aed} & L_{amd}h_{aeq} & 0 & -L_{amd} & 0 & L_{alkd}+L_{amd} & 0 & 0 \\ 0 & 0 & 0 & 0 & -L_{amq} & 0 & L_{alkq}+L_{amq} & 0 \\ 0 & 0 & 0 & 0 & 0 & 0 & 0 & e_{88} \end{bmatrix}$$

$$e_{88}=-(c_1 c_{addc}+c_2 c_{aqdc})$$

(4.105)

$$\mathbf{F}=\begin{bmatrix} R_{es}+r_{edd} & r_{edq}-\omega_e(L_{els}+L_{emq}) & 0 & 0 & 0 & 0 & 0 & 0 \\ r_{eqd}+\omega_e(L_{els}+L_{emd}) & R_{es}+r_{eqq} & -\omega_e L_{emd} & 0 & 0 & 0 & 0 & 0 \\ 0 & 0 & -R_{efd} & 0 & 0 & 0 & 0 & 0 \\ 0 & 0 & 0 & R_{as}+r_{add} & r_{adq}-\omega_a(L_{als}+L_{amq}) & 0 & \omega_a L_{amq} & h_{addc} \\ -\omega_a L_{amd}h_{aed} & -\omega_a L_{amd}h_{aeq} & 0 & r_{aqd}+\omega_a(L_{als}+L_{amd}) & R_{as}+r_{aqq} & -\omega_a L_{amd} & 0 & h_{aqdc} \\ 0 & 0 & 0 & 0 & 0 & -R_{akd} & 0 & 0 \\ 0 & 0 & 0 & 0 & 0 & 0 & -R_{akq} & 0 \\ 0 & 0 & 0 & f_{84} & f_{85} & 0 & 0 & f_{88} \end{bmatrix}$$

$$f_{84}=c_1 r_{add}+c_2 r_{aqd}$$
$$f_{85}=c_1 r_{adq}+c_2 r_{aqq}$$
$$f_{88}=c_1 h_{addc}+c_2 h_{aqdc}-1$$

(4.106)

$$\mathbf{G} = \begin{bmatrix} 0 & 0 \\ 0 & 0 \\ 1 & 0 \\ 0 & r_{adl} \\ 0 & r_{aql} \\ 0 & 0 \\ 0 & 0 \\ 0 & c_1 r_{adl} + c_2 r_{aql} \end{bmatrix}. \tag{4.107}$$

If a resistive load were connected to the dc-link, equations which allow us to determine matrices **E**, **F** and **G** can easily be modified by substituting

$$\tilde{i}_{load} = \frac{\tilde{v}_{dc}}{R_l} \tag{4.108}$$

where R_l is the load resistance. In that case, the only input to the system is represented by exciter's field voltage.

If dc-link voltage is considered to be system's output, the output equation can be written in the form

$$\tilde{v}_{adc} = \mathbf{C}\mathbf{x} + \mathbf{D}\mathbf{u}, \tag{4.109}$$

where

$$\mathbf{C} = \begin{bmatrix} 0 & 0 & 0 & 0 & 0 & 0 & 0 & 1 \end{bmatrix}, \tag{4.110}$$

$$D = \begin{bmatrix} 0 \end{bmatrix}. \tag{4.111}$$

4.5.3. Transfer functions

A linearized representation of the system allows to find system's transfer functions. For dc-link voltage controller design, it is necessary to have Bode plots of $\tilde{v}_{adc} / \tilde{v}_{efd}$ (also

referred to as control-to-output) transfer function. This transfer function can be found from linearized state space representation as

$$\frac{\tilde{v}_{adc}}{\tilde{v}_{efd}} = \mathbf{C}(s\mathbf{I} - \mathbf{A})^{-1}\mathbf{B} + \mathbf{D}\,. \tag{4.112}$$

However, it is almost always faster to plot this transfer function by directly performing frequency-domain simulation of the system's average model. Fig. 4.17 and Fig. 4.18 show thus obtained Bode plots of magnitude and phase of $\tilde{v}_{adc}/\tilde{v}_{efd}$ at two different operating points. In both cases, dc load is represented by a current source.

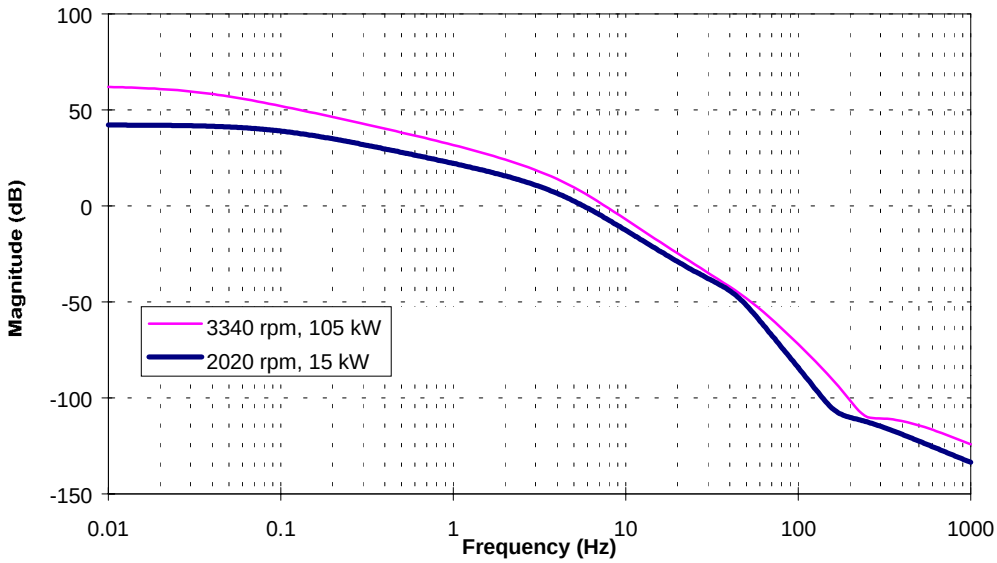

Fig. 4.17. Magnitude of the exciter's field voltage-to-dc-link voltage transfer function with current source load, at two different operating points.

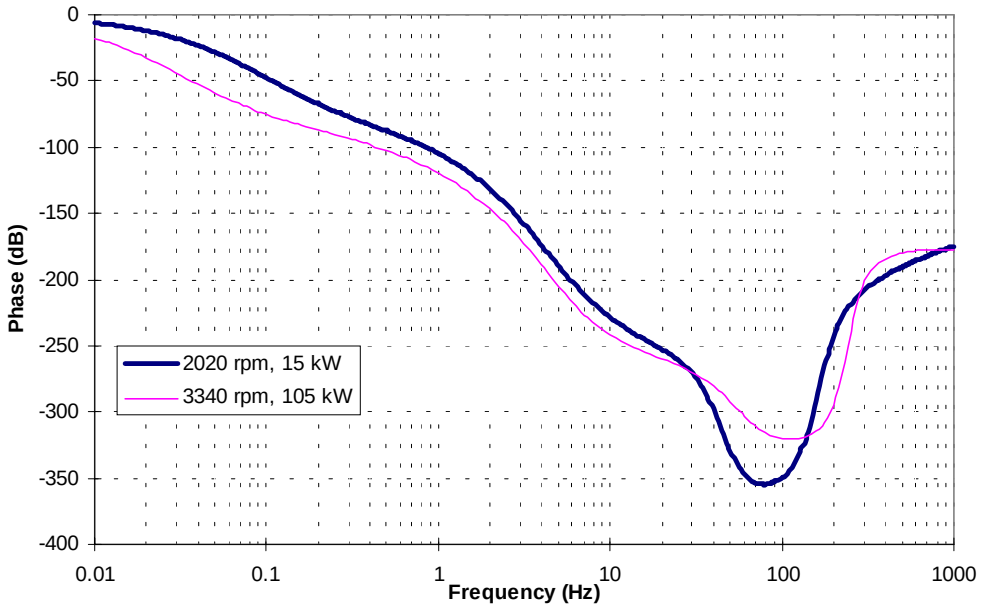

Fig. 4.18. Phase of the exciter's field voltage-to-dc-link voltage transfer function with current source load, at two different operating points.

It can be seen from these figures that this system can hardly be approximated with a first-, or even second-order transfer function. The phase, for example, reaches values well below -180^{o} (which would be the minimum phase reached by a second-order transfer function). These facts become even more obvious if the transfer function's poles and zeros are found numerically (from numerator and denominator of (4.112)). They are listed in Table 4.2 for the operating point characterized by 3340 rpm and 105 kW current source load. It will be seen in the following chapter that all frequencies below 100 Hz are of interest for dc-link voltage control-loop design. It is clear from Table 4.2 that there are six poles and three zeros in that frequency range. Therefore, accurate Bode plots of this transfer function, obtainable with the use of the generator/rectifier average model, are essential for dc-link voltage control design.

Fig. 4.17 and Fig. 4.18 show that both magnitude and phase of control-to-output transfer function change as operating point changes. Since the load is represented by a current source, which does not contribute to damping of the system, this dependence can be attributed mainly to changes in generator speed, i.e. to the fact that the generator's reactances increase proportionally to the speed. The question then arises, which operating point to select as the basis for control-loop design. It can be argued that, at higher speed

and load, magnitude of control-to-output transfer function is higher, and phase starts decreasing sooner, than at lower speed and load. Therefore, the system seems to be 'more difficult' to compensate at operating points corresponding to high speed and load. However, it can also be seen from Fig. 4.18 that there is a frequency range (from approximately 30 Hz to 130 Hz) in which phase of control-to-output transfer function is lower at low speed and load than at high speed and load. It will be seen in the following chapter that crossover frequency of the closed loop system will fall exactly in that range. In spite of that, we will select the operating point corresponding to high speed and load as the basis for dc-link voltage controller design. When the design is completed, operation of closed loop system at low load and speed will be verified through transient simulation and measurement.

Table 4.2. Poles and zeros of $\tilde{v}_{adc} / \tilde{v}_{efd}$ transfer function at 3340 rpm, 105 kW current source load.

Poles (rad/s)	Zeros (rad/s)
-0.2010	-28.27
-13.08	-470.6
-22.24+20.19j	-551.3
-22.24-20.19j	-281.5+1489j
-209.4+280.5j	-281.5+1489j
-209.4-280.5j	-2275
1059	$-8.336 \cdot 10^{13}$
2732	

It was mentioned in the introductory chapter that the generator (and inverter) was designed for rated power of 150 kW. However, the engine (by which the generator was driven) could only provide power somewhat higher than 100 kW. That is why 105 kW

were selected as the maximum power of the system for control design purpose. The corresponding speed was assumed to be 3340 rpm.

It was argued in Section 4.4.3 that current source load, as opposed to resistive load, makes the system more difficult to stabilize in closed loop. Since the average model allows us to find transfer functions with any kind of load, it is now possible to verify the validity of that argument. For the sake of comparison, Fig. 4.19 and Fig. 4.20 show magnitude and phase, respectively, of control-to-output transfer function at 3340 rpm, 105 kW, with current source load and resistive load. Table 4.3 lists poles and zeros of control-to-output transfer function with resistive load. It can be seen that, with resistive load, the lowest-frequency poles of the transfer function are at approximately two Hz, as opposed to 0.03 Hz with current source load (Table 4.2). That makes the phase of control-to-output transfer function with resistive load start decreasing at frequencies higher than with the current source load. Also, the dc gain of the transfer function is significantly lower with a resistive load. That is easily explained if it is remembered that, with resistive load, an increase in the exciter's field voltage by an amount x results in an increase, by an amount y, in main generator's armature voltage. Since the dc load is resistive, the main generator's armature current will also increase (by an amount approximately equal to y/R_l), increasing the voltage drop at the main generator's synchronous reactance. With current source load, however, the main generator's armature current is kept constant. Therefore, an increase by x in the exciter's field voltage will not result in an increased voltage drop at the main generator's synchronous reactance; consequently, the main generator's armature voltage will rise by an amount larger than y. This is seen as a larger magnitude of control-to-output transfer function.

Because of the two above listed reasons (higher dc gain and poles at lower frequencies), current source load definitely makes the system more difficult to stabilize in closed loop at frequencies up to approximately three Hz. After that frequency, there is almost no difference between transfer functions with current source or resistive load (that can also be seen by comparing poles and zeros in Table 4.2 and Table 4.3), and both are equally difficult, or easy, to compensate.

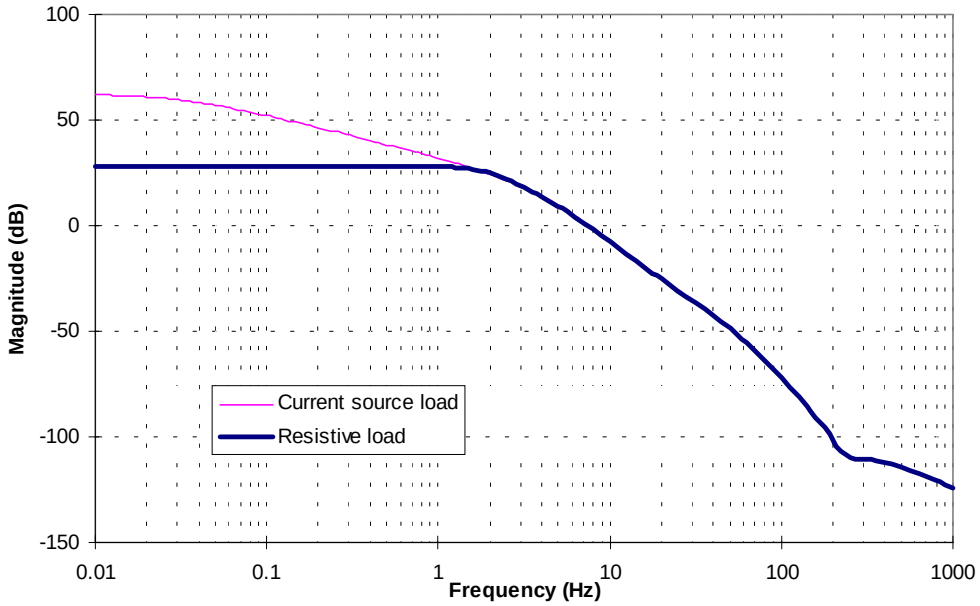

Fig. 4.19. Magnitude of the exciter's field voltage-to-dc-link voltage transfer function at 3340 rpm, 105 kW, with different kinds of load.

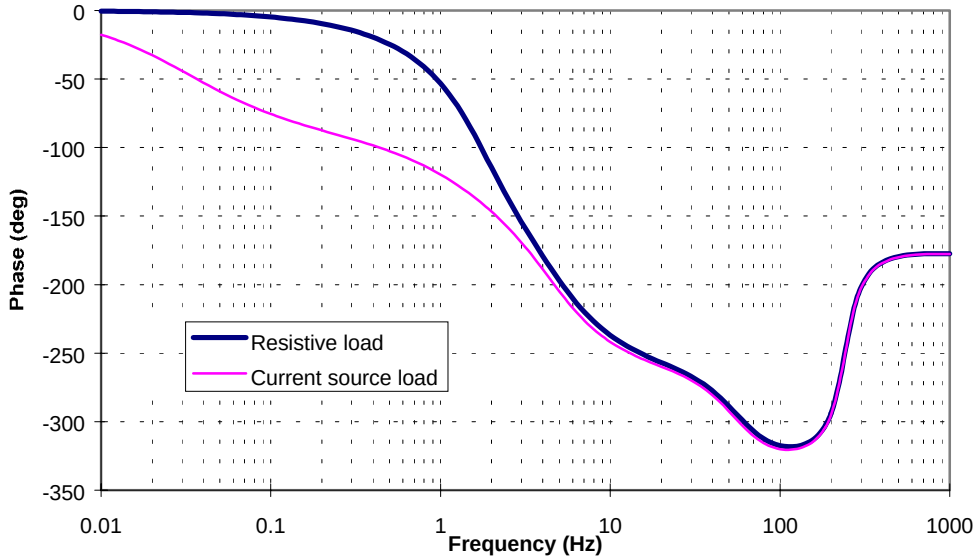

Fig. 4.20. Phase of the exciter's field voltage-to-dc-link voltage transfer function at 3340 rpm, 105 kW, with different kinds of load.

Current source load, as opposed to resistive load, can therefore be adopted as a more conservative option from a closed loop control design point of view. Consequently, transfer function relative to a speed of 3340 rpm and a current source load of 105 kW will represent a starting point for dc-link controller design, which is the matter of discussion of the following chapter.

Table 4.3. Poles and zeros of $\tilde{v}_{adc} / \tilde{v}_{efd}$ transfer function at 3340 rpm, 105 kW resistive load.

Poles (rad/s)	Zeros (rad/s)
-8.906+10.25j	-30.83
-8.906-10.25j	-500
-23.53+21.44j	-802.3
-23.53-21.44j	-281.6+1771j
-274.1+274.7j	-281.6+1777j
-274.1-274.7j	-2022
1140	$-9.098 \cdot 10^{13}$
2632	

Before concluding this chapter, let it note that the average generator/rectifier model can provide any other system's transfer function that may be of interest for a particular application. One such example is the system's output impedance, which will be a topic of discussion in the following chapter. Two other examples are given in Fig. 4.21 and Fig. 4.22, which show Bode plots of the exciter's field voltage-to-exciter's field current and the exciter's field voltage-to-main generator's field current transfer functions. These transfer functions would be interesting if the objective were to implement some kind of field current control. That was not the case in the system under our study, due to the following reasons. The main generator's field current is rotating with the shaft, and is therefore not available for sensing. The exciter's field current is affected by a large amount of ripple (visible in Fig. 4.5, Fig. 4.8 and Fig. 4.11), which should be filtered in order to control the exciter field current's average value. Filtering of that ripple would introduce poles in the control-loop that would compromise the bandwidth of the closed loop system.

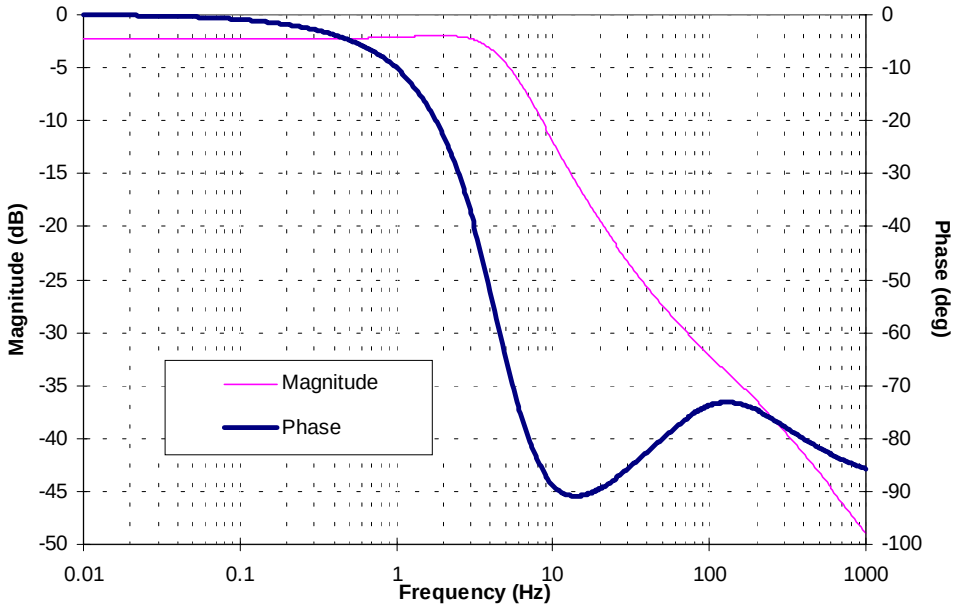

Fig. 4.21. The exciter's field voltage-to-exciter's field current transfer function at 3340 rpm, 105 kW current source load.

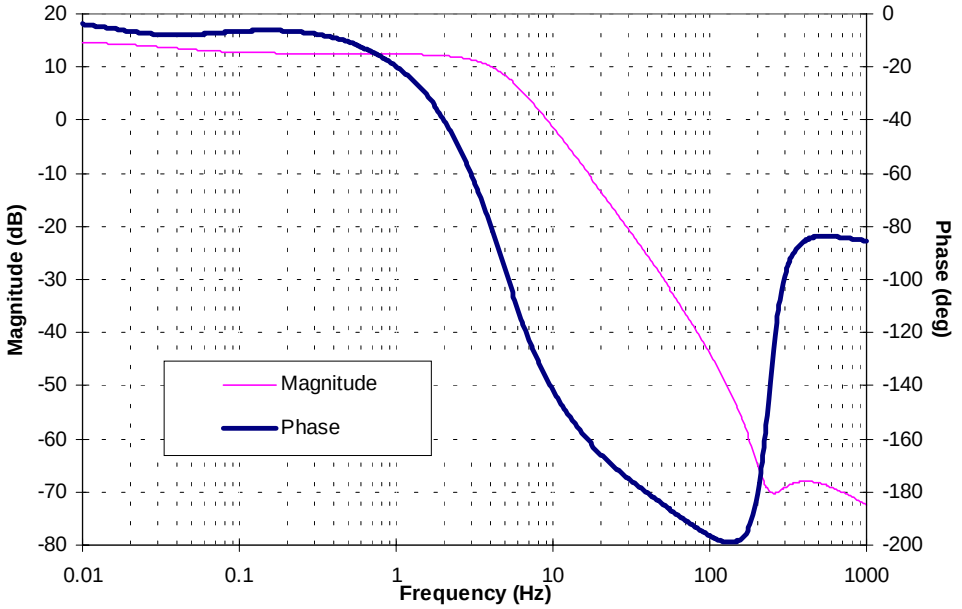

Fig. 4.22. The exciter's field voltage-to-main generator's field current transfer function at 3340 rpm, 105 kW current source load.

Chapter 5. Dc-Link Control-Loop Design

5.1. Introduction

It has already been stated that two major advantages of the developed average generator/rectifier model consist in savings in transient simulation time and the possibility to perform frequency-domain analysis. The latter was of crucial importance for the practical application that motivated this entire work, i.e. for control design of the generator set shown in Fig. 1.1. It is our intention in this final chapter to show, in detail manner, how the dc-link voltage control-loop compensator was designed based on the control-to-output transfer function shown in Fig. 4.17 and Fig. 4.18 and repeated, for convenience, in Fig. 5.1. Apart from representing a good example of practical usefulness of the developed model, this chapter will supply additional proofs of the model's validity through comparison of closed-loop transient simulation and measurement results.

Block diagram of the closed loop system drawn for small signal analysis is shown in Fig. 5.2. In Fig. 5.2, $G(s)$ represents the exciter's field voltage-to-dc-link voltage transfer function, p represents the gain of the dc-link voltage sensor, $H(s)$ stands for

dynamic compensator's transfer function, M for modulator's gain, and V_g for input voltage of the buck dc-to-dc power supply used to provide the exciter's field voltage. Regarding signals' notation, $\tilde{v}_{efd}$ and $\tilde{v}_{adc}$ have already been introduced, while $\tilde{v}_s$ stands for dc-link voltage sensed signal, $\tilde{v}_m$ for voltage signal input to the modulator, and $\tilde{d}$ for the buck converter's duty cycle.

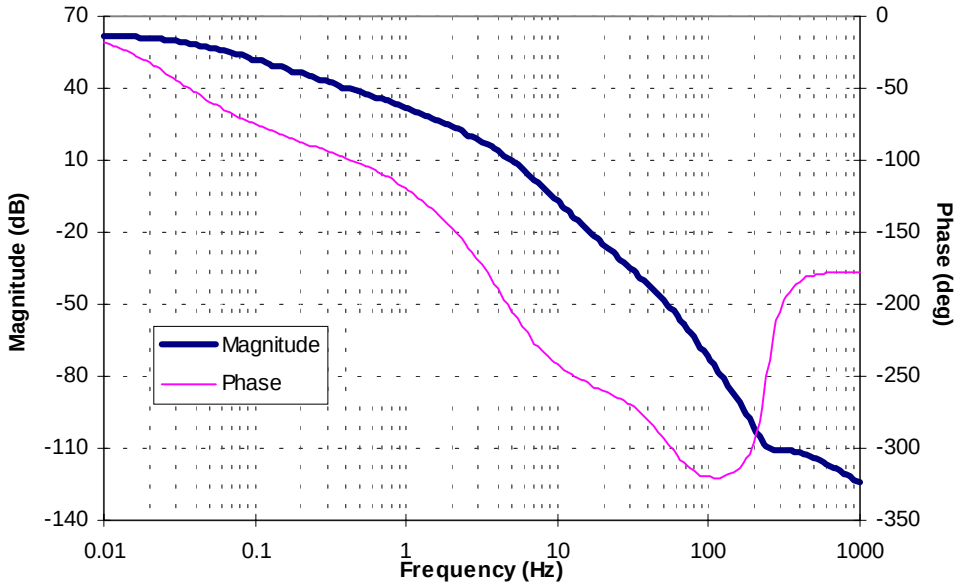

Fig. 5.1. The exciter's field voltage-to-dc-link voltage transfer function at 3340 rpm and 105 kW current source load.

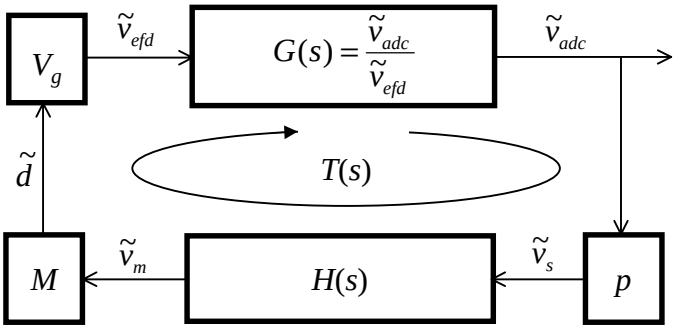

Fig. 5.2. Small-signal block diagram of the closed-loop system.

Stability and performance of the closed loop system can be expressed in terms of system's loop gain $T(s)$ which, as indicated in Fig. 5.2, is the product of all blocks forming the loop, i.e.

$$T(s) = G(s)\,pH(s)MV_g\,.$$

(5.1)

Sensor gain p, modulator gain M and voltage V_g are constants which follow from a particular choice of hardware components. In this application, they had the following values:

- p=0.005;
- M=0.56;
- V_g=48 V.

With these parameters fixed, loop gain is shaped by selecting appropriate gain, poles and zeros of the compensator's transfer function $H(s)$. Stability and performance criteria, such as phase margin and crossover frequency, can be read directly from Bode plots of the system's loop gain. In this particular application, no specifications were defined regarding these criteria. That means that any stable dc-link voltage control-loop is acceptable, as long as it enables the inverter to operate according to its own requirements. The first attempt in compensator design was made, therefore, with a simple PI compensator. For reasons which will be discussed in the following sections, the system's operation with that compensator was found to be unsatisfactory, and a more complex compensator, consisting of three zeros and five poles, needed to be designed and implemented.

5.2. PI compensator

5.2.1. Design

The PI compensator is the simplest compensator that provides zero steady state error, due to its pole in the origin. The compensator's transfer function is

$$H(s) = k\frac{1+\frac{s}{\omega_z}}{s}.$$

(5.2)

Standard analog realization of this transfer function is shown in Fig. 5.3. After one component's value, say C_2, is chosen, the other two can be calculated from the compensator's pole and zero as

$$R_1 = \frac{1}{kC_2},$$

(5.3)

$$R_2 = \frac{1}{\omega_z C_2}.$$

(5.4)

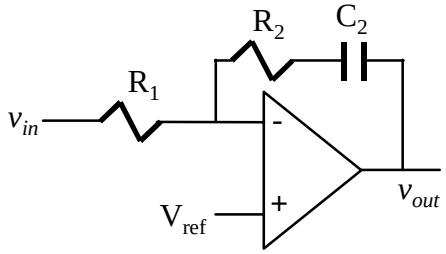

Fig. 5.3. Analog realization of a PI compensator.

Zero at ω_z has the role of compensating for the 90º phase lag introduced by the pole in the origin. It can be seen from Fig. 5.1 that the zero needs to be placed between 0.1 Hz and 1 Hz in order to have the desired phase-boosting effect. After the zero is placed, gain *k* can be adjusted in order to have stable system with the acceptable phase margin.

With zero placed at 1 Hz, and the compensator's gain of 1.25, the loop gain shown in Fig. 5.4 is obtained. It is characterized by a crossover frequency of 1 Hz and a phase margin of approximately 25º. A higher phase margin would have been preferred, but the crossover frequency would have become unacceptably low in that case.

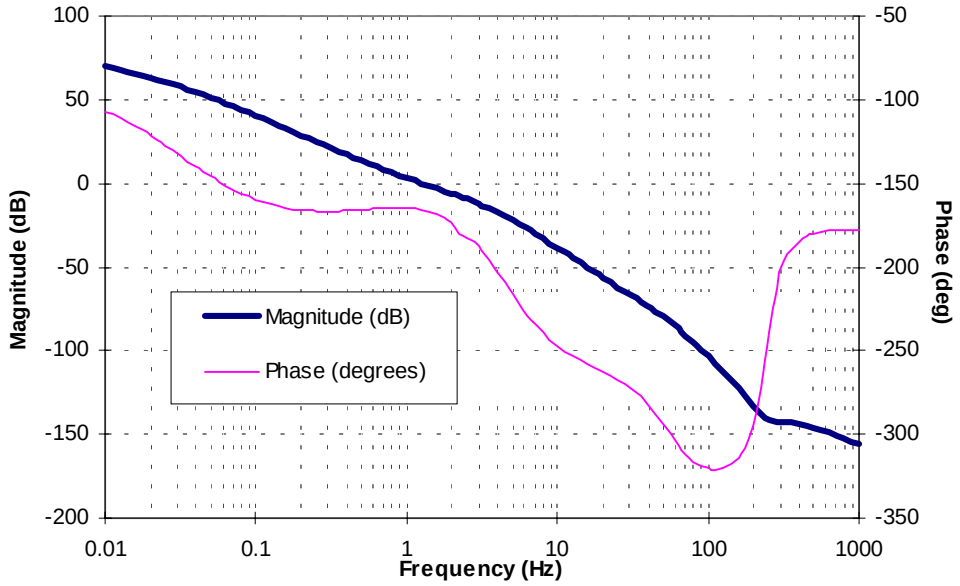

Fig. 5.4. Loop gain with PI compensator (3340 rpm, 105 kW current source load).

5.2.2. Operation with resistive dc load

After the PI compensator was implemented as shown in Fig. 5.3, operation of the system was tested with a resistive load connected to main generator's dc-link. The power level at which testing was done was significantly lower than the rated power of the system, because of the unavailability of a dc load with appropriate voltage and power rating. The buck converter's input voltage V_g was also reduced, compared to the design value of 48 V.

Fig. 5.5-Fig. 5.8 show average model simulation and measurement results relative to resistive load step and two different speeds. Dc-link voltage is regulated at 400 V, and the load is switched from 19.2 kW to 12.8 kW in both cases. Transient response is always stable, but is characterized by large overshoot and settling time, due to poor bandwidth. It can also be noticed that average model simulation results match well with measurement results, which is another confirmation of the average model's validity. Average model simulation results can actually be considered somewhat conservative, since they predict values of overshoot and settling time slightly larger than their measured values.

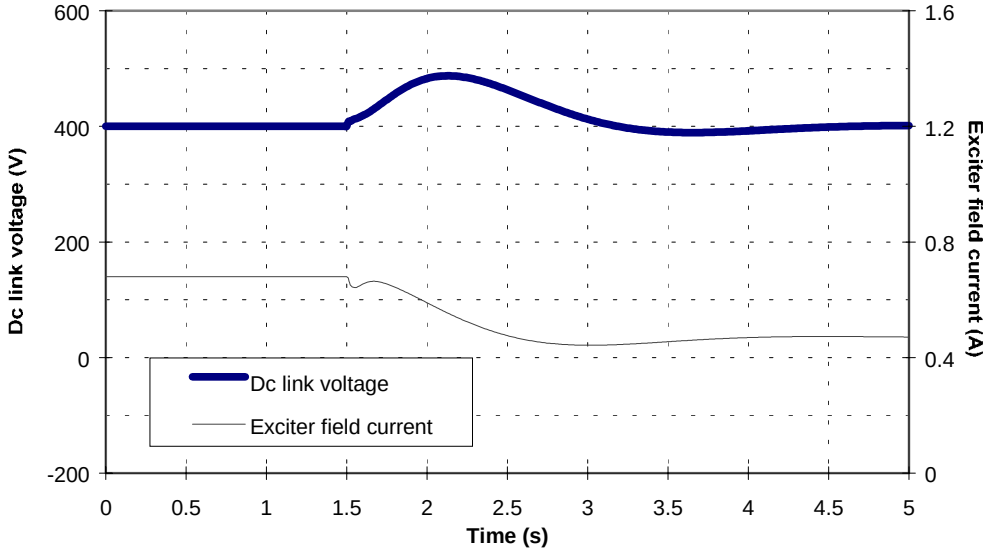

Fig. 5.5. Average model simulation: dc-link voltage and the exciter's field current at resistive load step from 8.3 Ω to 12.5 Ω (n=2000 rpm, V_g=25 V).

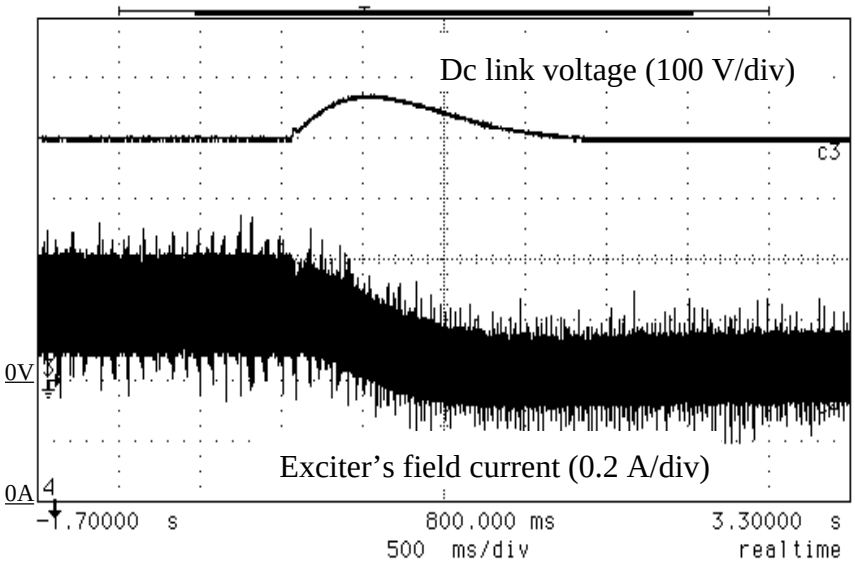

Fig. 5.6. Measurement: dc-link voltage and the exciter's field current at resistive load step from 8.3 Ω to 12.5 Ω (n=2000 rpm, V_g=25 V).

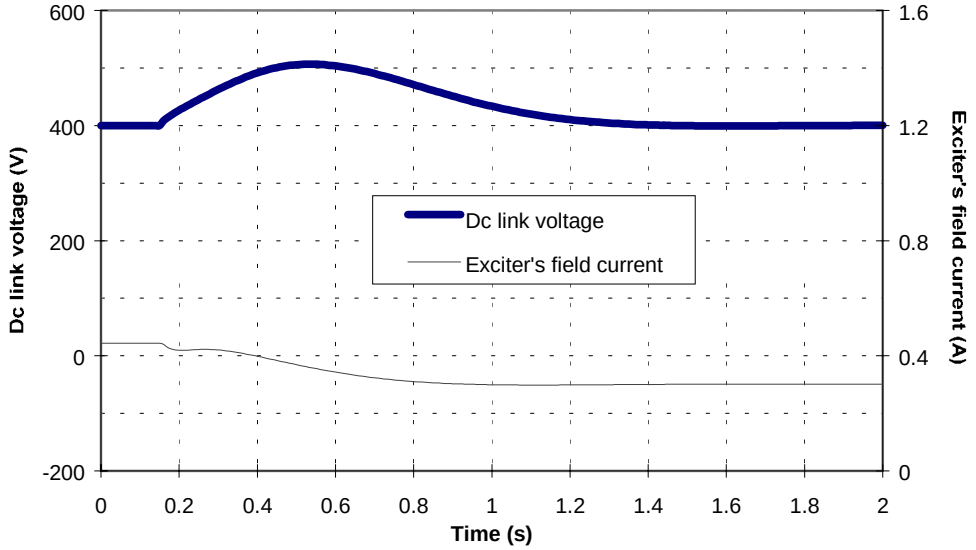

Fig. 5.7. Average model simulation: dc-link voltage and the exciter's field current at resistive load step from 8.3 Ω to 12.5 Ω (n=3800 rpm, V_g=15 V).

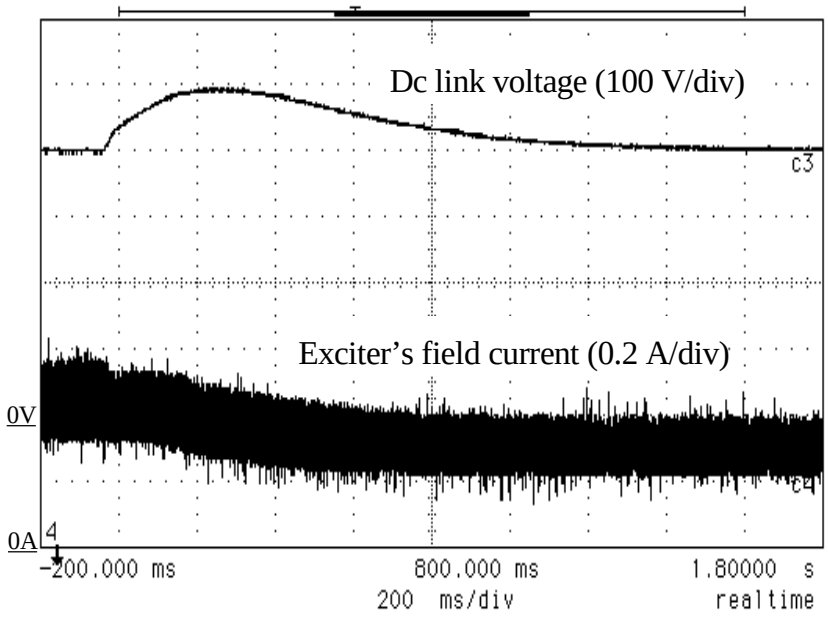

Fig. 5.8. Measurement: dc-link voltage and the exciter's field current at resistive load step from 8.3 Ω to 12.5 Ω (n=3800 rpm, V_g=15 V).

5.2.3. Operation with inverter load and instability problem

After testing with resistive dc load, testing the closed loop system with inverter connected to the dc-link was attempted. When that was done, instability occurred in the form of oscillations of the dc-link voltage. This instability is due to the nature of the inverter load, and can be explained in terms of the generator's output impedance and the inverter's input impedance [22], [23].

A regulated inverter (i.e. an inverter operating in closed voltage loop) behaves like a constant power load which, from the small-signal point of view, can be modeled as a negative resistor, characterized by a phase of -180º. If such a load is connected to a non-ideal voltage source, as shown in Fig. 5.9, it can be shown that the system will be stable if

$$|Z_{o1}| < |Z_{i2}| . \tag{5.5}$$

Otherwise, there may be instability in the cascaded system, depending on the phase of the ratio Z_{o1}/Z_{i2}.

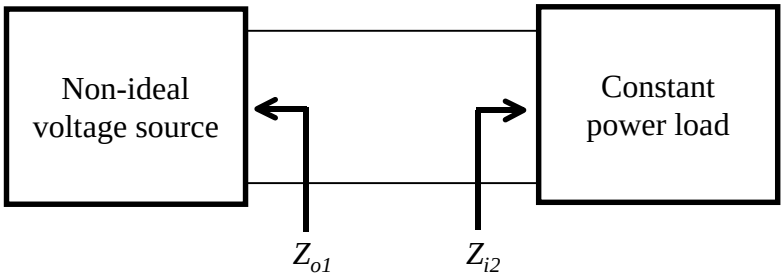

Fig. 5.9. Illustration for instability problem.

Fig. 5.10 shows the generator's output impedance ('seen' from the dc-link, therefore including the dc-link capacitor) in open and closed loop. It can be seen that, at frequencies up to the crossover frequency, closing the loop reduces the magnitude of the generator's output impedance by a factor approximately equal to the loop gain magnitude. Around the crossover frequency, there is a certain peaking in closed loop output impedance due to the small phase margin, which makes it somewhat higher than

the open loop output impedance. At frequencies significantly higher than the crossover frequency, closing the loop has no effect on the output impedance.

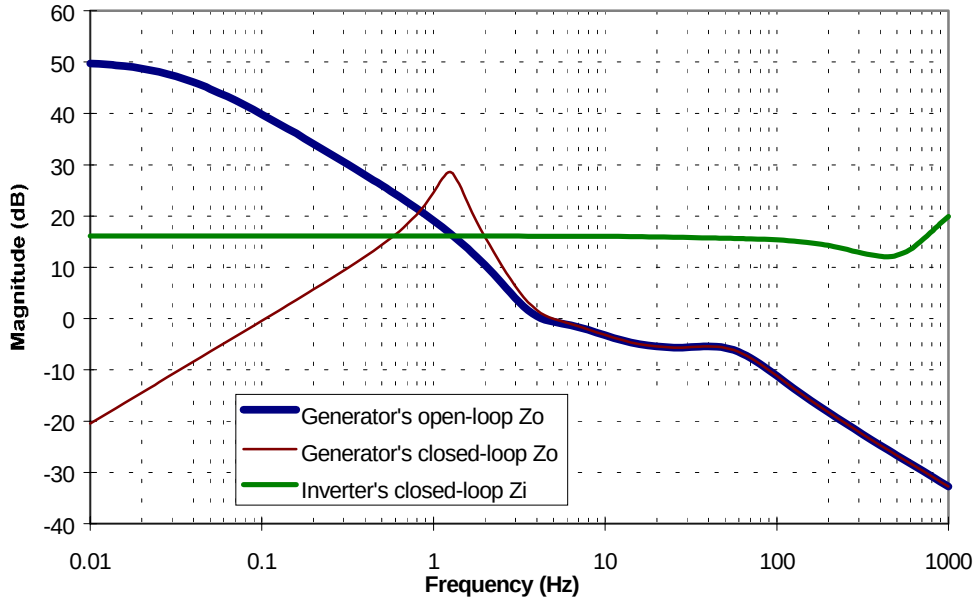

Fig. 5.10. Magnitude of the generator's output impedance (in open and closed loop) and the inverter's input impedance (3340 rpm, 105 kW current source load).

Fig. 5.10 also shows input impedance of the inverter operating in closed voltage loop at 105 kW output power level. It can be seen that the inverter's input impedance intersects with the generator's closed-loop output impedance. Therefore, instability is present in the system.

A solution to the instability problem consists in increasing the bandwidth of the dc-link voltage loop. It can be predicted from the generator's open-loop output impedance plot in Fig. 5.10 that, if the dc-link voltage control-loop's crossover frequency were between ten Hz and 100 Hz, the generator's closed loop output impedance would have its peak between zero dB and ten dB, and would not intersect with the inverter's input impedance. That would stabilize the overall system.

With the above discussion in mind, the new control goal becomes to design a dc-link voltage loop compensator that would provide a crossover frequency large enough to make the generator's closed-loop output impedance smaller, at all frequencies, than the inverter's input impedance.

5.3. Multiple-pole, multiple-zero compensators

5.3.1. Design

It can be seen from Fig. 5.1 that the phase of control-to-output transfer function is the main cause of difficulties in achieving high crossover frequency. At 30 Hz (which is approximately the frequency at which crossover is desired), the phase of control-to-output transfer function is -270º. An additional phase lag of 90º will be introduced by the compensator's pole in the origin, necessary to have zero steady state error. That would cause the loop gain's phase to be -360º at the desired crossover frequency. In order to stabilize the system, three zeros are needed in the compensator's transfer function at frequencies lower than the desired crossover. For the compensator to be a causal system, there have to be at least as many poles as zeros in the compensator's transfer function; practical considerations, however, suggest that there be one more pole than zero, in order to attenuate the high-frequency noise that may appear at the compensator's input. That finally results in a four-pole, three zero compensator. Poles (other than the one in origin) need to be placed at frequencies as high as possible, in order to affect the loop gain's phase as little as possible below the crossover frequency. Zeros are placed between one Hz and ten Hz by following a trial-and-error procedure, in order to obtain a loop gain's magnitude that decreases steadily with a slope of approximately 20 dB/decade, and a phase which stays well above -180º up to the crossover frequency.

The simulation showed very good results with three compensator poles placed at 1 kHz, zeros at 1.5 Hz, 2 Hz and 10 Hz, and a gain of 584. The corresponding loop gain is shown in Fig. 5.11, and the generator's closed loop output impedance (together with the inverter's input impedance) in Fig. 5.12. It can be seen that crossover frequency is 100 Hz, with a phase margin of about 15 degrees. Such a low phase margin is acceptable because the loop gain's phase, right after the crossover, reaches a minimum of -167º and then rises again. It eventually reaches -180º at a frequency higher than one kHz. Actually,

if only the phase of the loop gain had been considered, crossover frequency could have been extended above 100 Hz. However, that would not have had the desired effect on the control-loop because of the shape of the loop gain's magnitude in the range of 200 Hz–1 kHz. As it is known, the control-loop is effective only as long as the loop gain's magnitude is much larger than one; that would not have been the case in the 200 Hz–1 kHz range with the magnitude shaped as in Fig. 5.11.

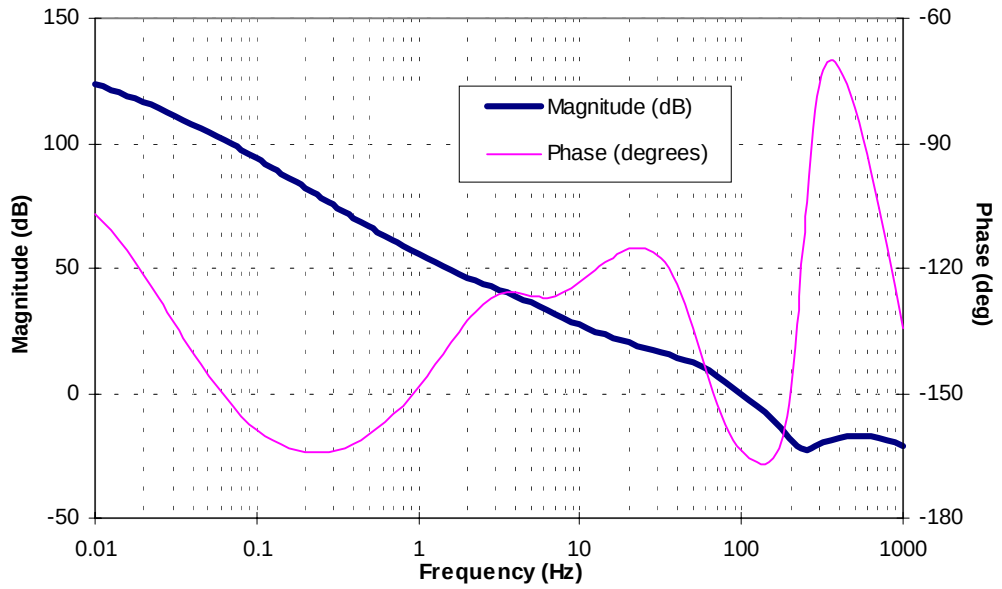

Fig. 5.11. Loop gain with four-pole, three-zero compensator (3340 rpm, 105 kW current source load).

It can be seen from Fig. 5.12 that, with a four-pole, three-zero compensator, the generator's closed loop output impedance always stays well below the inverter's input impedance. It could have been expected, therefore, that this compensator would have solved the instability problem.

An analog four-pole, three-zero compensator was implemented using three stages (three compensated operational amplifiers) connected in cascade. The first stage had a gain of one, one pole at one kHz and one zero at ten Hz; the second stage had a gain also equal to one, pole at one kHz and zero at two Hz; finally, the third stage had a gain of 584, one pole in the origin, one at one kHz, and one zero at 1.5 Hz. When tested, this compensator revealed itself to be extremely sensitive to noise. The reason for that was the fact that the first two stages, having one pole and one zero only, also had high, flat gain at

high frequencies, thus amplifying any noise that would appear at the compensator's input. The noise problems were serious enough to compromise entirely the operation of the closed loop system.

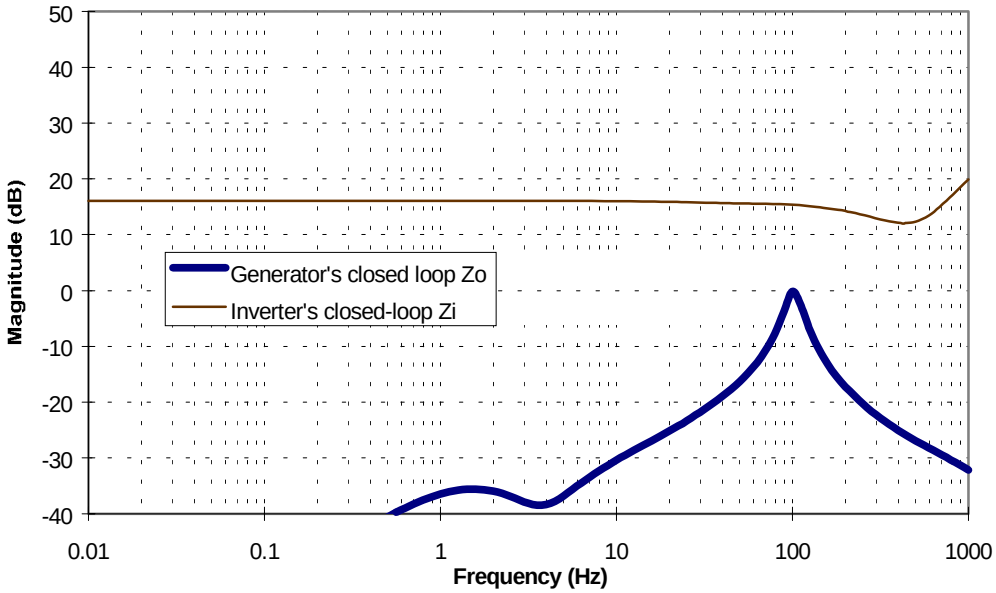

Fig. 5.12. Generator's closed loop output impedance with four-pole, three zero compensator (3340 rpm, 105 kW current source load).

In order to solve the noise-related problems, implementation of the compensator, and even the compensator itself, had to be changed. Instead of three stages, a two-stage approach was tried. The first stage had gain of one, one zero and two poles, so that its gain decreases at high frequencies. The second stage had two zeros and three poles (of which one was in the origin). Therefore, one pole was added to the compensator to reduce the high-frequency gain of the first stage. That resulted in a three-zero, five-pole compensator. All poles that previously used to be at one kHz, had to be shifted at lower frequencies, in order to decrease high-frequency gain of both stages. After several attempts, it was found by trial-and-error that pole frequencies of 150 Hz, 150 Hz, 250 Hz and 500 Hz made the noise effects tolerable. Frequencies at which compensator zeros were placed remained unchanged. The highest-frequency zero (ten Hz) and lowest frequency pole (150 Hz) were attributed to the first stage, in order to keep its gain as low as possible at all frequencies. Decreasing pole frequencies required a decrease by a factor of five (117 instead of 584) in the compensator's gain (attributed entirely to the second

stage), in order to keep the system stable. Fig. 5.13 compares magnitudes of the four-pole three-zero and five-pole, three-zero compensator's transfer functions. Note how much the five-pole, three-zero compensator reduces the magnitude above 200 Hz, where the frequency of the dc-link voltage ripple (240 Hz-798 Hz) and the inverter switching frequency (4 kHz) lie.

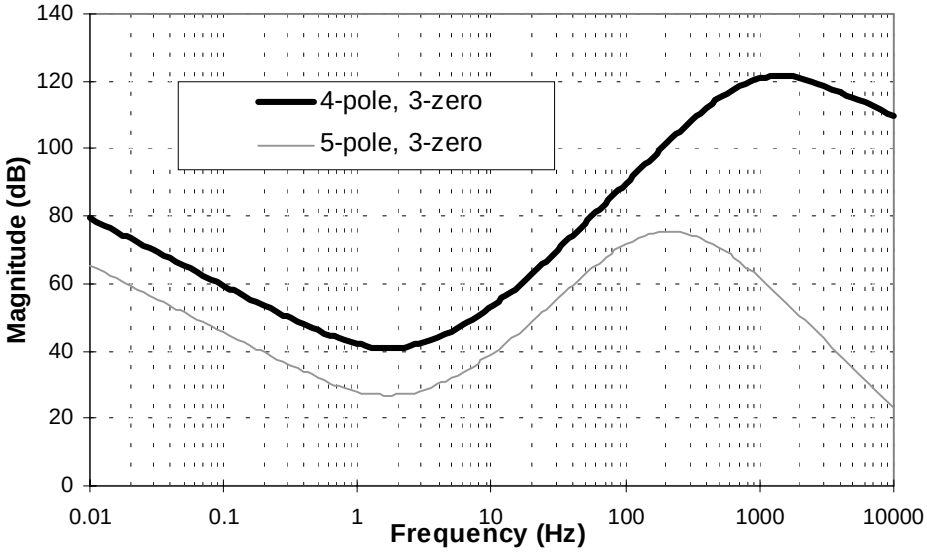

Fig. 5.13. Multiple-pole, multiple-zero compensators' transfer function's magnitudes.

The five-pole, three-zero compensator resulted in a somewhat lower crossover frequency (40 Hz), as shown in Fig. 5.14. It can be seen that the phase characteristic at frequencies above ten Hz was heavily influenced by moving compensator's poles to frequencies lower than one kHz, so that the phase actually reaches -180º soon after the crossover, leaving the phase margin of only about 20º.

In spite of a somewhat lower crossover frequency compared to a four-pole, three-zero compensator, the generator's closed-loop output impedance is still lower than the inverter's input impedance, as Fig. 5.15 shows. It can therefore be expected that operation with the inverter connected to the dc-link will be stable.

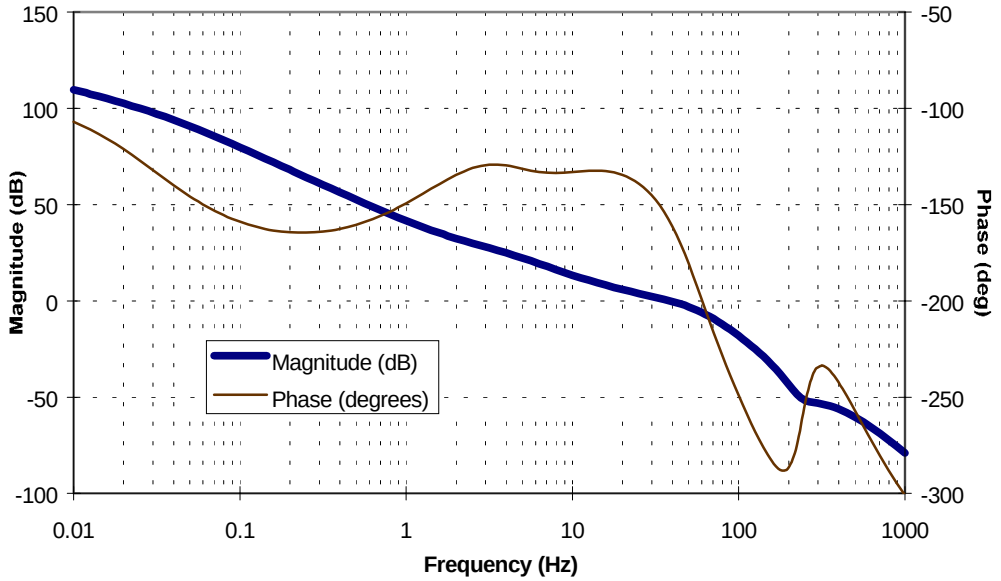

Fig. 5.14. Loop gain with five-pole, three-zero compensator (3340 rpm, 105 kW current source load).

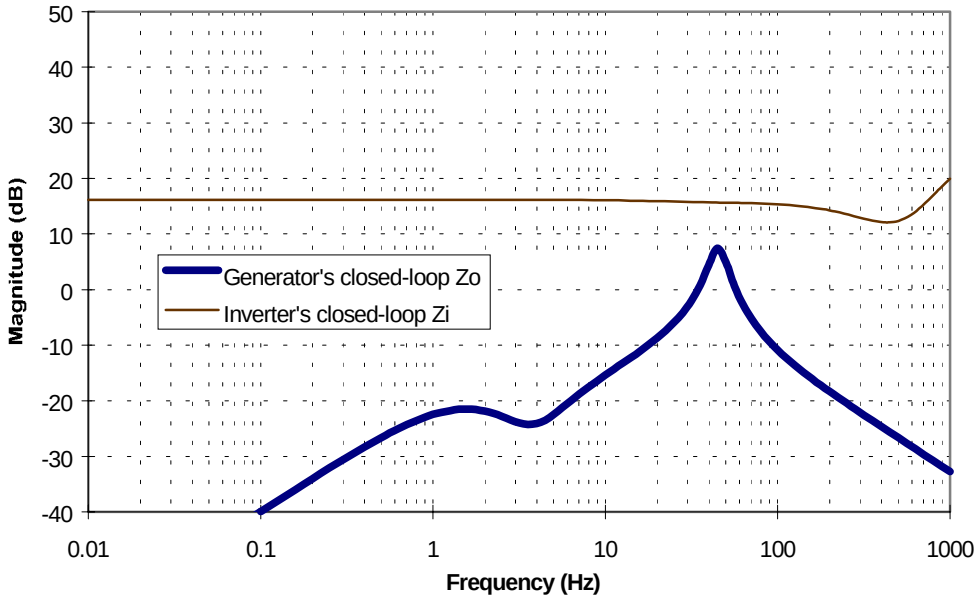

Fig. 5.15. Generator's closed loop output impedance with five-pole, three zero compensator (3340 rpm, 105 kW current source load).

An analog five-pole, three-zero compensator, having the transfer function

$$H(s) = k_a \frac{1+\frac{s}{\omega_{za}}}{\left(1+\frac{s}{\omega_{pa1}}\right)\left(1+\frac{s}{\omega_{pa2}}\right)} k_b \frac{\left(1+\frac{s}{\omega_{zb1}}\right)\left(1+\frac{s}{\omega_{zb2}}\right)}{s\left(1+\frac{s}{\omega_{pb1}}\right)\left(1+\frac{s}{\omega_{pb1}}\right)}, \tag{5.6}$$

was implemented with the circuit shown in Fig. 5.16.

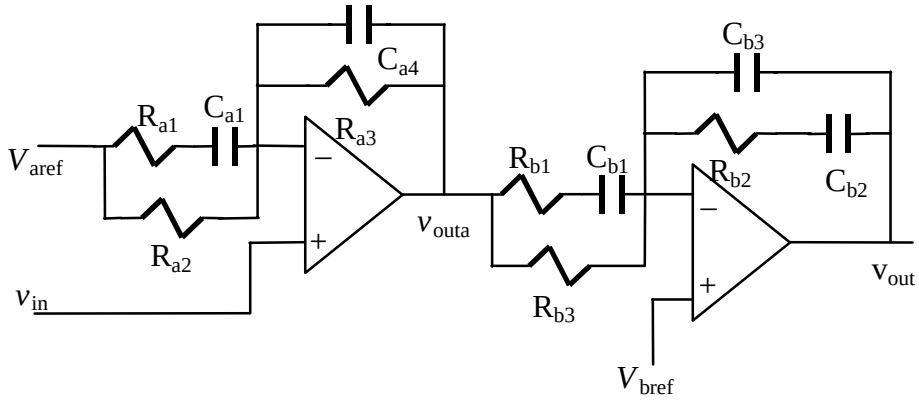

Fig. 5.16. Analog realization of a five-pole, three-zero compensator.

After one component value for each stage, say R_{a2} and R_{b1}, is chosen arbitrarily, others can be calculated from the transfer function's parameters as follows:

$$C_{a1} = \frac{1}{\omega_{za} R_{a2}}, \tag{5.7}$$

$$R_{a1} = \frac{1}{\omega_{pa1} C_{a1}}, \tag{5.8}$$

$$R_{a3} = k_a R_{a2}, \tag{5.9}$$

$$C_{a4} = \frac{1}{\omega_{pa2} R_{a3}}, \tag{5.10}$$

$$C_{b1} = \frac{1}{\omega_{pb2} R_{b1}}, \tag{5.11}$$

$$R_{b3} = \frac{1}{\omega_{zb2} C_{b1}}, \tag{5.12}$$

$$C_{b2} = \frac{1}{R_{b3} k_b}, \tag{5.13}$$

$$R_{b2} = \frac{1}{\omega_{zb1} C_{b2}}, \tag{5.14}$$

$$C_{b3} = \frac{1}{\omega_{pb1} R_{b2}}. \tag{5.15}$$

For (5.10)-(5.14) to be valid, it needs to be $C_{b2}>>C_{b3}$ and $R_{b3}>>R_{b1}$.

5.3.2. Operation with resistive dc load

The five-pole, three-zero compensator was first tested with a resistive dc load. The same transients presented in Section 5.2.2 for a PI compensator were simulated and measured with a five-pole, three-zero compensator. The results are shown in Fig. 5.17-Fig. 5.20. The time scale in these figures is the same as in Fig. 5.5-Fig. 5.8, relative to the PI compensator. It can be seen that the increased control-loop's bandwidth results in dramatically decreased overshoot and settling time.

Fig. 5.21-Fig. 5.24 show resistive load step of the same magnitude as the one shown in Fig. 5.17-Fig. 5.20, but of the opposite sign. Time scale is also more detailed, in order to highlight the close matching of simulated and measured results.

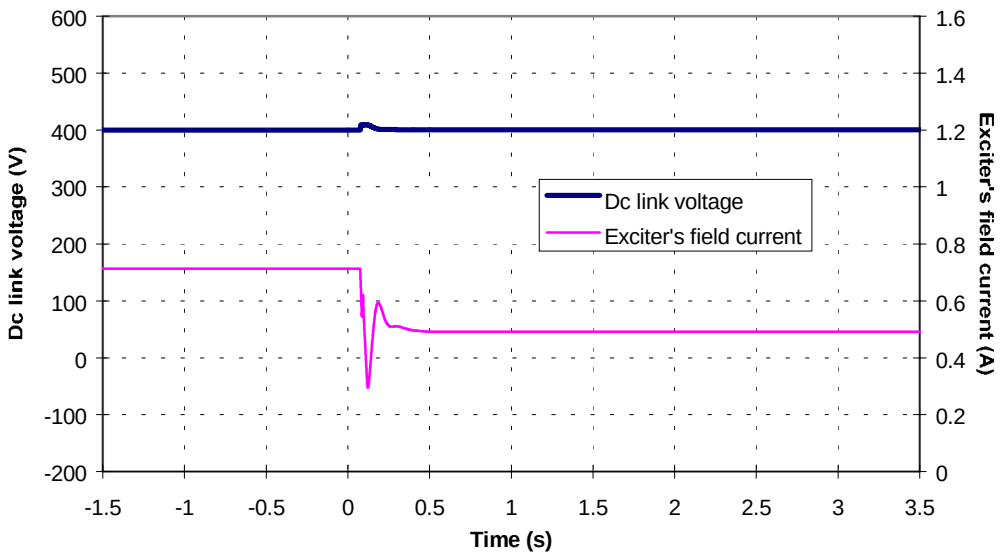

Fig. 5.17. Average model simulation: the dc-link voltage and exciter's field current for a resistive load step from 8.3 Ω to 12.5 Ω (n=2000 rpm, V_g=25 V).

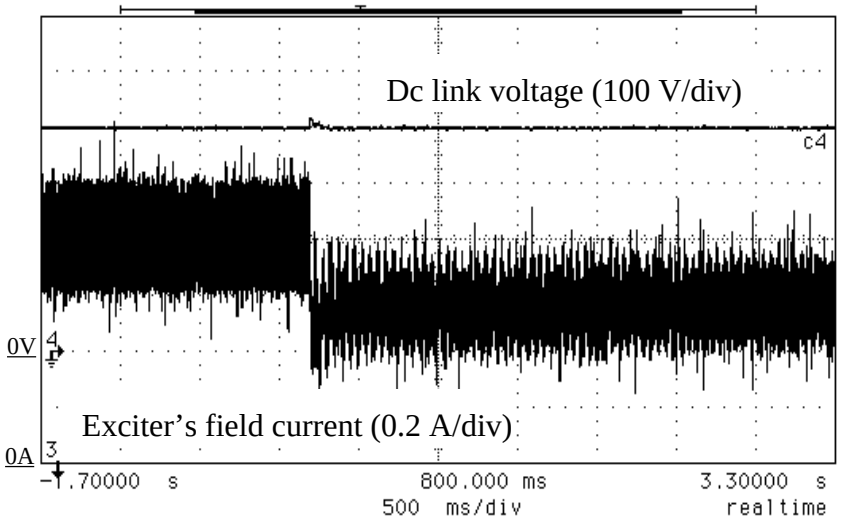

Fig. 5.18. Measurement: the dc-link voltage and exciter's field current for a resistive load step from 8.3 Ω to 12.5 Ω (n=2000 rpm, V_g=25 V).

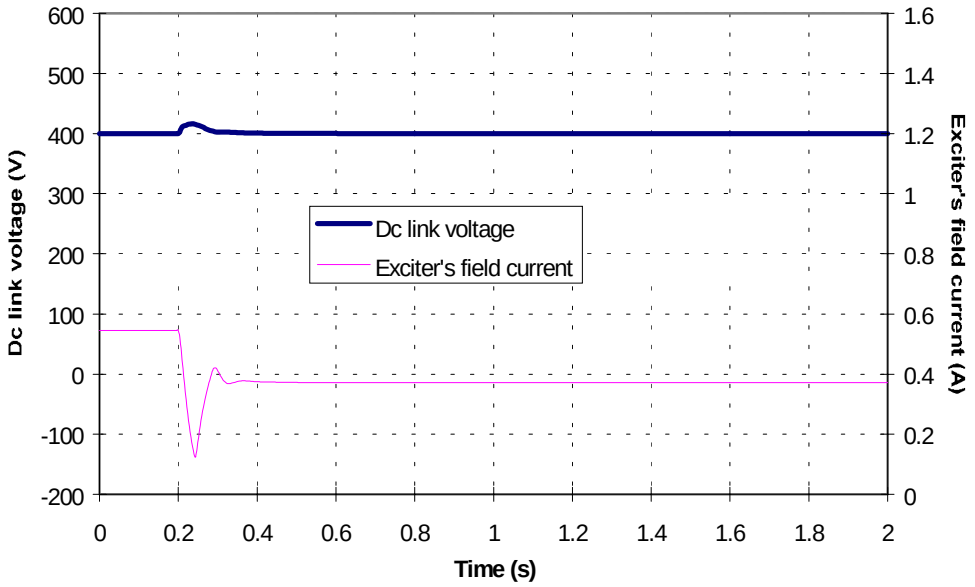

Fig. 5.19. Average model simulation: the dc-link voltage and exciter's field current for a resistive load step from 8.3 Ω to 12.5 Ω (n=3800 rpm, V_g=15 V).

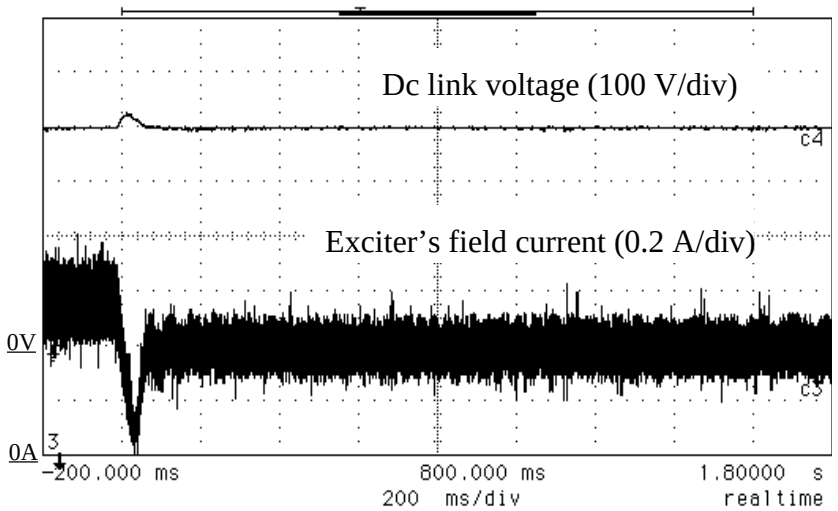

Fig. 5.20. Measurement: the dc-link voltage and exciter's field current for a resistive load step from 8.3 Ω to 12.5 Ω (n=3800 rpm, V_g=15 V).

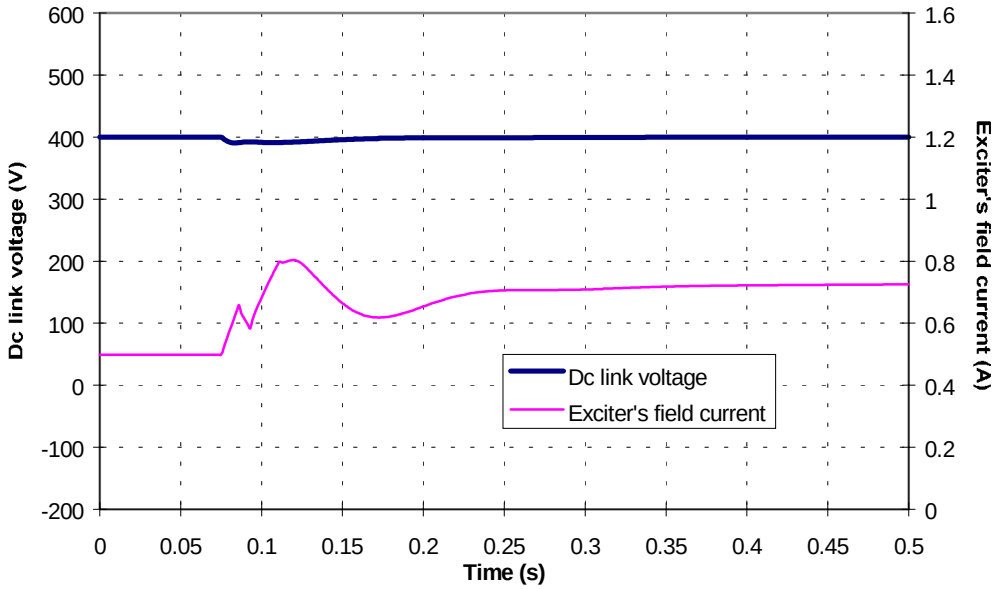

Fig. 5.21. Average model simulation: the dc-link voltage and exciter's field current for a resistive load step from 12.5 Ω to 8.3 Ω (n=2000 rpm, V_g=25 V).

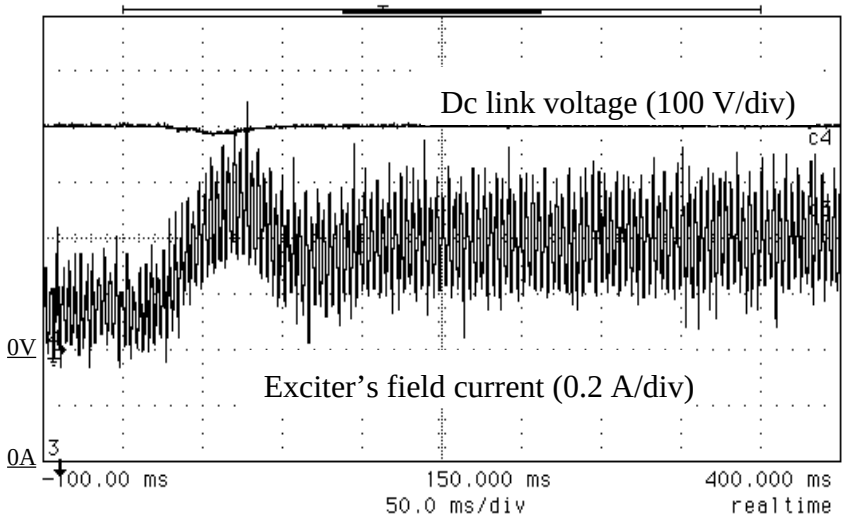

Fig. 5.22. Measurement: the dc-link voltage and exciter's field current for a resistive load step from 12.5 Ω to 8.3 Ω (n=2000 rpm, V_g=25 V).

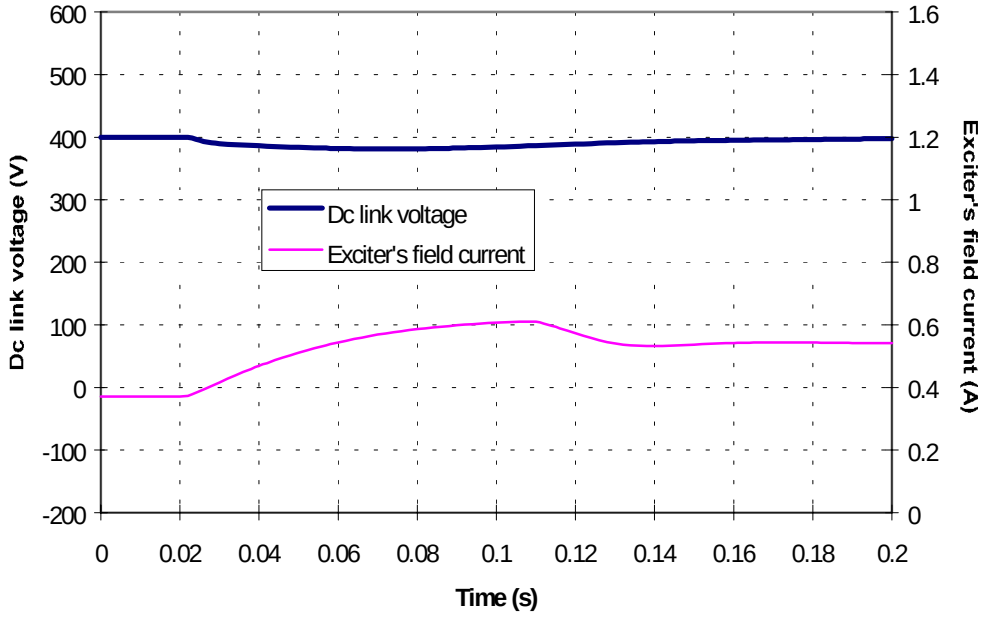

Fig. 5.23. Average model simulation: the dc-link voltage and exciter's field current for a resistive load step from 12.5 Ω to 8.3 Ω (n=3800 rpm, V_g=15 V).

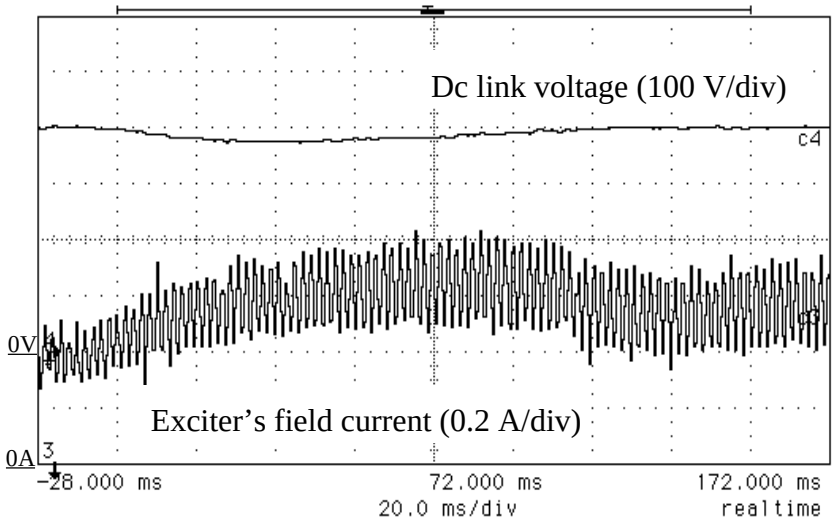

Fig. 5.24. Measurement: the dc-link voltage and exciter's field current for a resistive load step from 12.5 Ω to 8.3 Ω (n=3800 rpm, V_g=15 V).

5.3.3. Operation with inverter load

After the testing with a resistive load showed stable operation, fast transient response and good matching of simulated and measured results, a five-pole, three zero compensator was tested with the inverter connected to the dc-link. No instability was detected in the system.

Fig. 5.25 and Fig. 5.26 show the dc-link voltage and exciter's field current during the transient caused by stepping the inverter's resistive three-phase load from 12.8 kW to 18.8 kW. Due to the lack of damping at the dc-link, the response is slightly more oscillatory than with resistive load; overshoot in dc-link voltage is, nevertheless, very small.

It can be concluded, therefore, that a five-pole, three-zero compensator satisfies the requirements regarding the system's stability and the generator's output impedance damping.

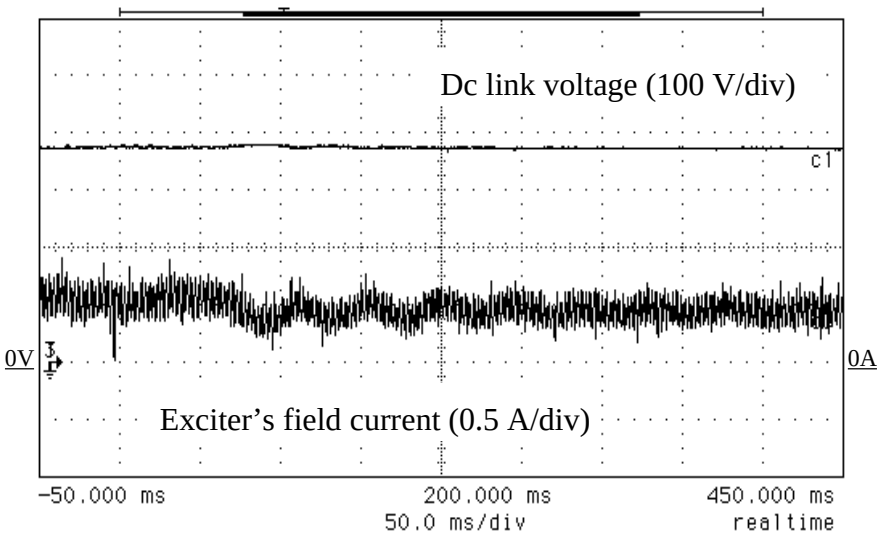

Fig. 5.25. Measurement: the dc-link voltage and exciter's field current at step in the inverter's resistive three-phase load from 18.8 kW to 12.8 kW (n=3000 rpm, V_g=35 V).

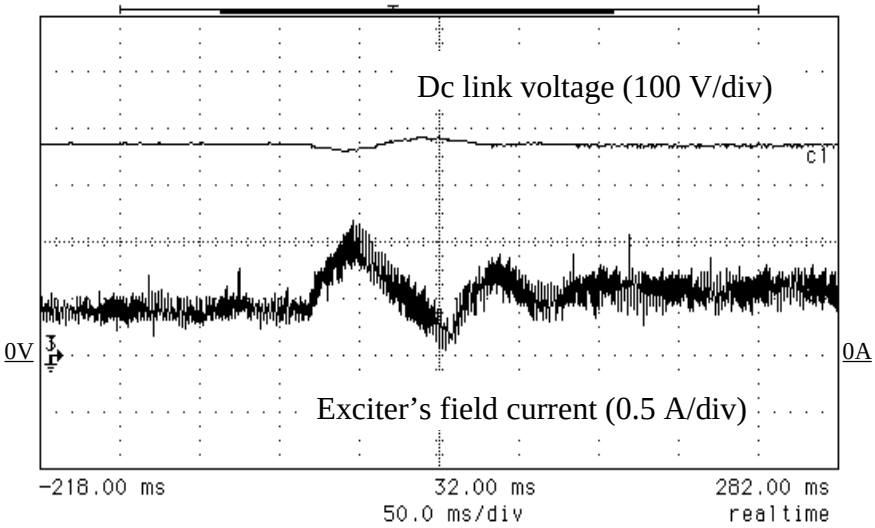

Fig. 5.26. Measurement: the dc-link voltage and exciter's field current at step in the inverter's resistive three-phase load from 12.8 kW to 18.8 kW (n=3800 rpm, V_g=35 V).

Chapter 6. Conclusions

When a diode rectifier is supplied from a three-phase voltage source with large internal impedance and/or is loaded with a reactive dc load, its operation cannot be described with equations derived analytically assuming instantaneous commutations of diodes. An example of a source which can cause extremely non-ideal operation of the rectifier is a variable-speed stand-by synchronous generator, characterized by an extremely large value of synchronous impedance as a consequence of variable-speed design. This thesis presents an attempt to develop a simplified model of the system consisting of a synchronous generator with large internal impedance feeding a diode rectifier with a reactive dc load. The results obtained, however, go beyond this particular application, and can be applied to any case in which the source's impedance significantly affects operation of the diode rectifier.

The basis for the development of the simplified, average generator/rectifier model consists of the study of the generator's ac waveforms affected by the non-ideal operation of the diode bridge and reactive nature of the dc load. This study is carried out through analysis of the switching model of the system. It can be concluded from such analysis that there exists a phase shift between the fundamental harmonics of the generator's voltage and current. In the ideal case, when commutations of the rectifier's diodes are instantaneous, this phase shift is equal to zero. Also, average values of dc current and voltage at the rectifier's output are found to be different than in the ideal case. The amount of phase shift and discrepancies in average values of the dc variables depend on

the parameters of the three-phase source (in the studied case, the synchronous generator), and the nature of the dc load (capacitive or inductive). They affect both transient and steady state operation of the system, and need to be taken into account when, for example, the system's control-loops are designed.

The developed average model of the diode rectifier relies on the assumption that fundamental harmonic of ac variables and average value of dc variables are of primary importance for the system's operation, as far as power transfer and dynamic behavior is concerned. This assumption is true in most practical applications, due to the primarily inductive character of the source's impedance and presence of a filter at rectifier's output. The developed model allows us to relate the dynamics of the three-phase source connected to the rectifier's input, to dynamics of the reactive dc load at rectifier's output. In doing so, the non-ideal operation of the rectifier is taken into account by means of three constants obtained from the switching model. These three constants model the diode rectifier in an average sense, i.e. they make it possible to establish a relationship between fundamental harmonics of ac voltage and current at the rectifier's input to average values of dc voltage and current at the rectifier's output. The dependence of these constants on the operating point is not highly pronounced, which results in the model's validity for both steady state and transient operation. This is verified to be true through comparison of the average model simulation results with switching model simulation results and measurement results, for both open- and closed-loop operation and different operating points.

The way the average model is implemented takes into account losses in the diode rectifier, and allows us to relate these losses directly to the average model's parameters. If diode losses are negligible, it can be shown that there are only two independent average model's parameters, from which the third one can be computed.

The main advantages of the average model, as opposed to the switching model, are savings in computational time when time-domain simulations are performed, and the possibility to perform frequency-domain analysis of the system. The latter is the result of the average model's equations' being time-continuous and, therefore, easy to linearize. From linearized equations, it is possible to obtain state-space representation and transfer

functions of the system. In the studied case, practical interest was focused on the exciter's field voltage-to-dc-link voltage transfer function, which represents the system's control-to-output transfer function. Dependence of this transfer function on the operating point and nature of dc load was discussed from the point of view of dc-link voltage control-loop design.

Design of this control-loop is a good example of a practical application of the developed model. Control-to-output transfer function, obtained with the average generator/rectifier model, shows that the actual order of the system in this case is such that the often-used, first-order generator model cannot be applied. That is particularly true if a high-order (five pole, three-zero) dynamic compensator needs to be designed in order to stabilize the cascaded generator-rectifier-inverter system, affected by instability due to poor matching of output and input impedances of different parts of the system. In such a design, the system's dynamic response needs to be known, in a detailed manner, at frequencies much higher than the frequency corresponding to the transfer function's dominant pole. The developed average generator/rectifier model represents a unique and indispensable means to study and solve this and similar problems.

References

[1] J. G. Kassakian, M. F. Schlecht and G. C. Verghese, *Principles of Power Electronics*, Addison-Wesley Publishing Company, 1991.

[2] W. J. Bonwick and V. H. Jones, "Performance of a synchronous generator with a bridge rectifier," *Proceedings IEE*, Vol. 119, No. 9, September 1972, pp. 1338-1342.

[3] W. J. Bonwick and V. H. Jones, "Rectifier-loaded synchronous generator with damper windings," *Proceedings IEE*, Vol. 120, No. 6, June 1973, pp. 659-666.

[4] V. H. Jones and W. J. Bonwick, "Three-phase bridge rectifiers with complex source impedance," *Proceedings IEE*, Vol. 122, No. 6, June 1975, pp. 630-636.

[5] W. J. Bonwick, "Characteristics of a diode-bridge-loaded synchronous generator without damper windings," *Proceedings IEE*, Vol. 122, No. 6, June 1975, pp. 637-641.

[6] W. J. Bonwick, "Voltage waveform distortion in synchronous generators with rectifier loading," *IEE Proceedings*, Vol. 127, Pt. B, No. 1, January 1980, pp. 13-19.

[7] R. L. Ames, "A.C. Generators: Design and Applications," Research Studies Press Ltd., Taunton, Somerset, England, 1990

[8] P. C. Krause, *Analysis of Electric Machinery*, New York: McGraw Hill, Inc., 1987.

[9] M. Jadric, *Dinamika elektricnih strojeva*, Graphis, Zagreb, 1997.

[10] *PSpice A/D Reference Manual*, Version 8.0, MicroSim Corporation, June 1997.

[11] A.H.M.S. Ula and Abul R. Hasan, "Design and Implementation of a Personal Computer Based Automatic Voltage Regulator for a Synchronous Generator," *IEEE Transactions on Energy Conversion*, Vol. 7, No.1, March 1992, pp. 125-130.

[12] A. Ghandakly and P. Kronneger, "Digital Controller Design Method for Synchronous Generator Excitation and Stabilizer Systems, Parts I and II," *IEEE Transactions on Power Systems*, Vol. PWRS-2, No. 3, August 1987, pp. 633-644.

[13] Y. Takeda and B. Adkins, "Determination of synchronous-machine parameters allowing for unequal mutual inductances," *Proceedings IEE*, Vol. 121, No. 12, December 1974, pp. 1501-1504.

[14] M. E. Coultes and W. Watson, "Synchronous Machine Models by Standstill Frequency Response Tests," *IEEE Transactions on Power Apparatus and Systems*, Vol. PAS-100, No. 4, April 1981, pp. 1480-1489.

[15] P. L. Dandeno and A. T. Poray, "Development of a Detailed Turbogenerator Equivalent Circuit from Standstill Frequency Response Measurement," *IEEE Transactions on Power Apparatus and Systems*, Vol. PAS-100, No. 4, April 1981, pp. 1646-1655.

[16] S. H. Minnich, "Snall Signals, Large Signals, and Saturation in Generator Modeling," *IEEE Transactions on Energy Conversion*, Vol. EC-1, No. 1, March 1986, pp. 94-102.

[17] *IEEE Standard Procedures for Obtaining Synchronous Machine Parameters by Standstill Frequency Response Testing*, IEEE Std. 115A-1987.

[18] A. Keyhani, H. Tsai and T. Leksan, "Maximum Likelihood Estimation of Synchronous Machine Parameters from Standstill Time Response Data," IEEE Transaction on Energy Conversion, Vol. 9, No. 1, March 1994, pp. 98-114.

[19] A. Keyhani, H. Tsai, "Identification of High-Order Synchronous Generator Models from SSFR Test Data," *IEEE Transactions on Energy Conversion*, Vol. 9, No. 3, September 1994, pp. 593-603.

[20] P. C. Krause and T. A. Lipo, "Analysis and Simplified Representations of Rectifier-Inverter Induction Motor Drives," *IEEE Transactions on Power Apparatus and Systems*, Vol. PAS-88, No. 5, May 1969, pp. 588-596.

[21] P. C. Krause and T. A. Lipo, “Analysis and Simplified Representations of Rectifier-Inverter Reluctance-Synchronous Motor Drives,” *IEEE Transactions on Power Apparatus and Systems*, Vol. PAS-88, No. 6, June 1969, pp. 962-970.

[22] R. D. Middlebrook, “Input Filter Considerations in Design and Applications of Switching Regulators,” *IEEE IAS Annual Meeting*, Chicago, IL, October 11-14, 1976.

[23] B. H. Cho, “*Modeling and Analysis of Spacecraft Power Systems*,” Ph.D. Dissertation, Virginia Polytechnic Institute and State University, Blacksburg, Virginia, October 1985.

Vita

Ivan Jadric

Ivan Jadric is a native of Split, Croatia. From 1989 to 1991 he studied at the Faculty of Electrical Engineering, University of Zagreb, in Zagreb, Croatia, and from 1991 to 1995 at the Polytechnic of Turin in Turin Italy. He obtained the BS in Electrical Engineering from the Polytechnic of Turin in July 1995. From August 1995 to January 1998, he was with the Virginia Power Electronics Center at Virginia Tech in Blacksburg, Virginia, working towards the MS degree in Electrical Engineering. He is currently with the York International Corporation in York, Pennsylvania.